National Library of Canada
Canadian Theses Service
Ottawa, Canada
K1A 0N4

Bibliothèque nationale du Canada
Service des thèses canadiennes

NOTICE

The quality of this microform is heavily dependent upon the quality of the original thesis submitted for microfilming. Every effort has been made to ensure the highest quality of reproduction possible.

If pages are missing, contact the university which granted the degree.

Some pages may have indistinct print especially if the original pages were typed with a poor typewriter ribbon or if the university sent us an inferior photocopy.

Reproduction in full or in part of this microform is governed by the Canadian Copyright Act, R.S.C. 1970, c. C-30, and subsequent amendments.

AVIS

La qualité de cette microforme dépend grandement de la qualité de la thèse soumise au microfilmage. Nous avons tout fait pour assurer une qualité supérieure de reproduction.

S'il manque des pages, veuillez communiquer avec l'université qui a conféré le grade.

La qualité d'impression de certaines pages peut laisser à désirer, surtout si les pages originales ont été dactylographiées à l'aide d'un ruban usé ou si l'université nous a fait parvenir une photocopie de qualité inférieure.

La reproduction, même partielle, de cette microforme est soumise à la Loi canadienne sur le droit d'auteur, SRC 1970, c. C-30, et ses amendements subséquents.

NL-339 (r. 88/04) c

Canada

UNIVERSITY OF ALBERTA

QUARTIC NONLINEAR HAMILTONIAN SYSTEMS

BY

MAN LEUNG ALEXANDER NIP

©

A THESIS
SUBMITTED TO THE FACULTY OF GRADUATE STUDIES AND RESEARCH
IN PARTIAL FULFILMENT OF THE REQUIREMENTS FOR THE DEGREE
OF

MASTER OF SCIENCE
IN
THEORETICAL PHYSICS

DEPARTMENT OF PHYSICS

EDMONTON, ALBERTA
FALL 1991

National Library
of Canada

Bibliothèque nationale
du Canada

Canadian Theses Service

Service des thèses canadiennes

Ottawa, Canada
K1A 0N4

The author has granted an irrevocable non-exclusive licence allowing the National Library of Canada to reproduce, loan, distribute or sell copies of his/her thesis by any means and in any form or format, making this thesis available to interested persons.

The author retains ownership of the copyright in his/her thesis. Neither the thesis nor substantial extracts from it may be printed or otherwise reproduced without his/her permission.

L'auteur a accordé une licence irrévocable et non exclusive permettant à la Bibliothèque nationale du Canada de reproduire, prêter, distribuer ou vendre des copies de sa thèse de quelque manière et sous quelque forme que ce soit pour mettre des exemplaires de cette thèse à la disposition des personnes intéressées.

L'auteur conserve la propriété du droit d'auteur qui protège sa thèse. Ni la thèse ni des extraits substantiels de celle-ci ne doivent être imprimés ou autrement reproduits sans son autorisation.

ISBN 0-315-69982-5

Canada

UNIVERSITY OF ALBERTA

RELEASE FORM

NAME OF AUTHOR: Man Leung Alexander Nip

TITLE OF THESIS: Quartic Nonlinear Hamiltonian Systems

DEGREE: Master of Science

YEAR THIS DEGREE GRANTED: 1991

Permission is hereby granted to the University of Alberta Library to reproduce single copies of this thesis and to lend or sell such copies for private, scholarly or scientific research purposes only.

The author reserves other publication rights, and neither the thesis nor extensive extracts from it may be printed or otherwise reproduced without the author's written permission.

Man Leung Alexander Nip
Department of Physics
University of Alberta
Edmonton, Alberta
T6G 2J1

Date: August 12, 1991

UNIVERSITY OF ALBERTA

FACULTY OF GRADUATE STUDIES AND RESEARCH

The undersigned certify that they have read, and recommended to the Faculty of Graduate Studies and Research for acceptance, a thesis entitled "Quartic Nonlinear Hamiltonian Systems" submitted by Man Leung Alexander Nip in partial fulfilment of the requirements for the degree of Master of Science in Theoretical Physics.

Dr. J. A. Tuszynski, Supervisor

D G Hughes

Dr. D. G. Hughes

Dr. J. Stephenson

Dr. Z. W. Gortel

Dr. J. S. Muldowney

Date: August 12, 1991

To my sisters and my very best friend Lawrence

ABSTRACT

We study some special cases of Hamiltonian systems with fourth order polynomial potentials and detail their deterministic and chaotic behavior. In particular, for systems which are characterized by one order parameter, we introduce generalizations of the Landau-Ginzburg model to three dimensions and include an external weak magnetic field. For those systems that are described by two spatial parameters with coupling, as an example, we examine the x^2y^2 potential problem and apply an anharmonic phonon perturbation theory to a two-dimensional atomic lattice. Exact solutions to the above deterministic systems are described in detail both analytically and numerically. Chaotic behavior of the coupled systems is analyzed with perturbative techniques and, by numerical analysis, demonstrated through sequential Poincaré sections.

ACKNOWLEDGEMENTS

I wish to thank my supervisor Dr. J. A. Tuszyński not only for introducing me to nonlinear dynamics but also for his patience and continuous encouragement.

I also want to thank Dr. Z. W. Gortel for many of his valuable contributions in much of Chapter Four.

I am very grateful to my supervisory committee: Dr. J. A. Tuszyński, Dr. D. G. Hughes, Dr. J. Stephenson, Dr. Z. W. Gortel and Dr. J. S. Muldowney for carefully proof reading this thesis and for many of their helpful suggestions.

I wish to express my gratitude to Dr. R. Teshima for his programming expertise which made many of the numerical simulations possible. I also want to thank Dan Bright for introducing me to programming in **C**, which was my main programming tool during the time of my research.

Finally, the staff of the Physics Department has always been supportive. Many thanks to Lynn Chandler and Phyllis Tripp for making many parts of my research work enjoyable.

TABLE OF CONTENTS

1 LANDAU-GINZBURG MODEL OF UNIAXIAL FERROMAGNETS 1

1.1 Introduction 1

1.2 The Model 4

1.3 Equation of Motion 5

1.4 Solution 7

a) Trivial Solution 7

b) Solutions Corresponding to Real Roots 7

c) Two Real and Two Purely Imaginary Roots 19

d) Solutions Corresponding to Four Purely Imaginary Roots . . 23

e) Solutions Corresponding to Four Complex Roots 24

1.5 Free Energy 26

a) The Ferromagnetic and The Antiferromagnetic Spin Waves . 27

1.6 Partition Functions and Specific Heats 32

2 LANDAU-GINZBURG MODEL OF A UNIAXIAL FERROMAGNET IN THE PRESENCE OF A MAGNETIC FIELD 41

2.1 Equation of Motion 42

2.2 The Ferromagnetic and The Antiferromagnetic Spin Waves 43

2.3 Mean Magnetization 46

a) The $sn(u,k)$ Solutions 47

b) The $cn(u,k)$ Solutions 49

c) The $dn(u,k)$ Solutions 52

2.4 Free Energy 56

3 BIFURCATIONS AND PERTURBATIVE ANALYSIS IN THE X^2Y^2 POTENTIAL PROBLEM 62

3.1 Numerical Simulations 64

3.2 Perturbative Analysis I 71

3.3 Perturbative Analysis II 78

4 CHAOS IN TWO-DIMENSIONAL LATTICES 84

4.1 The Model 85

4.2 The Mean Field Potential 86

4.3 Nearest- Neighbor Interactions 88

4.4 The Equations of Motion and The Continuum Limit 91

4.5 The Hamiltonian 94

4.6 Numerical Analysis 97

4.7 Conclusions 106

BIBLIOGRAPHY 108

LIST OF FIGURES

1.1 Plots of $\dot{P}^2$ as a function of P. These are the possible cases in which real solutions exist. 8

1.2 Solution of (1.16) with a plus sign. 9

1.3 Solution of (1.18) with $\epsilon = 1$. 11

1.4 Solution of (1.19) with $\epsilon = 1$. 11

1.5 Solution of (1.21) with $\epsilon = 1$. 13

1.6 Solution of (1.22) with $\epsilon = 1$. 13

1.7 The $dn(u, k)$ Jacobian elliptic function. 15

1.8 The $sn(u, k)$ Jacobian elliptic function. 17

1.9 The periodic singular solution of (1.31) for $P_2 = 1$. 18

1.10 Solution of (1.34) with a plus sign. 20

1.11 The periodic singular solution of (1.35). 21

1.12 The $cn(u, k)$ Jacobian elliptic solution of (1.36). 22

1.13 The $tn(u, k)$ Jacobian elliptic function. 24

1.14 The periodic singular solution of (1.41). 25

1.15 A comparison of the γ-dependence of the free energy for the $dn(u, k)$ elliptic waves at various temperatures. The lower curve represents $\epsilon = -1$ while the upper overlapping curves represent ϵ from -0.1 to -10^{-6}. 28

1.16 A comparison of the γ-dependence of the free energy for the $sn(u,k)$ elliptic waves at various temperatures. The upper curve represents $\epsilon = -1$ while the lower overlapping curves represent ϵ from -0.1 to -10^{-6}. 29

1.17 A similar comparison for the $cn(u,k)$ elliptic waves as in the previous two figures. Here, $\epsilon < 0$. The lower solid and the dashed curves correspond to $\epsilon = -1$ and $\epsilon = -0.1$ respectively. The upper overlapping curves correspond to ϵ from -0.01 to -10^{-6}. 30

1.18 A similar comparison for the $cn(u,k)$ elliptic waves as in the previous figure. Here, $\epsilon > 0$. The upper and the lower dashed curves correspond to $\epsilon = 1$ and $\epsilon = 0.1$ respectively. The lower overlapping curves correspond to ϵ from 0.01 to 10^{-6}. 31

1.19 The partition function of the $dn(u,k)$ elliptic solutions. The solid line represents the empirical relation. The actual (numerical) data points are denoted by "+." 33

1.20 The partition function of the $sn(u,k)$ elliptic solutions. 34

1.21 The partition function of the $cn(u,k)$ elliptic solutions for $\epsilon < 0$. . . 34

1.22 The partition function of the $cn(u,k)$ elliptic solutions for $\epsilon > 0$. . . 35

1.23 The specific heat capacity for the $dn(u,k)$ and the $sn(u,k)$ elliptic solutions. 37

1.24 The specific heat capacity of the $cn(u,k)$ elliptic solutions in the case where $\epsilon < 0$. 38

1.25 The specific heat capacity of the $cn(u,k)$ elliptic solutions in the case where $\epsilon > 0$. 39

2.1 Plot of the polynomial $R(M)$ as a function of M. 44

2.2 Field dependence of the mean magnetization for the $sn(u,k)$ solutions. 48

2.3 Mean magnetization for the $cn(u,k)$ waves at $\varepsilon = -0.75$. 50

2.4 Mean magnetization for the $cn(u,k)$ waves at $\varepsilon = -0.55$. 50

2.5 Mean magnetization for the $cn(u,k)$ waves at $\varepsilon = -0.45$. 51

2.6 Mean magnetization for the $cn(u,k)$ waves at $\varepsilon = -0.01$. 51

2.7 Mean magnetization of $dn(u,k)$ waves for $M_4 < M_3 < M_2 \leq M \leq M_1$. 54

2.8 Mean magnetization of $dn(u,k)$ waves for $M_4 \leq M \leq M_3 < M_2 < M_1$. 55

2.9 Field dependence of the free energy for the $sn(u,k)$ solutions. 57

2.10 Free energy of the $cn(u,k)$ solutions at $\varepsilon = -0.6$. 57

2.11 Free energy of the $cn(u,k)$ solutions at $\varepsilon = -0.55$. 58

2.12 Free energy of the $cn(u,k)$ solutions at $\varepsilon = -0.5$. 58

2.13 Free energy of the $cn(u,k)$ solutions st $\varepsilon = -0.45$. 59

2.14 Free energy of the $dn(u,k)$ waves in region 1. 59

2.15 Free energy of the $dn(u,k)$ waves in region 2. 60

3.1 Three-dimensional plot of the x^2y^2 -potential. 63

3.2 Contour plot of the potential. 63

3.3 A stable periodic trajectory. 65

3.4 The straight-interval trajectory $y = -x$ 66

3.5 x as a periodic function of t for the straight-line path. 66

3.6 y as a periodic function of t for the straight-line path. 67

3.7 $\dot{x}$ as a periodic function of t for the straight-line path. 67

3.8 $\dot{y}$ as a periodic function of t for the straight-line path. 68

3.9 Trajectory for $x_0 = -1.2$. 69

3.10 Trajectory for $x_0 = -0.8$. 70

3.11 x *vs* t for $x_0 = -1.2$. 71

3.12 x *vs* t for $x_0 = -0.8$. 72

3.13 y *vs* t for $x_0 = -1.2$. 72

3.14 y *vs* t for $x_0 = -0.8$. 73

3.15 $\dot{x}$ *vs* t for $x_0 = -1.2$. 73

3.16 $\dot{x}$ *vs* t for $x_0 = -0.8$. 74

3.17 $\dot{y}$ *vs* t for $x_0 = -1.2$. 74

3.18 $\dot{y}$ *vs* t for $x_0 = -0.8$. 75

4.1 A two-dimensional crystal lattice. 86

4.2 An atom with its four nearest-neighbors. 89

4.3 The potential energy of the decoupled oscillators for various values of the effective wave vector K. 96

4.4 Contour plot of the potential in (4.43). 98

4.5 Poincaré section at $E = -0.33$ 99

4.6 Poincaré section at $E = -0.31$ 100

4.7 Separatrix of the previous figure. 101

4.8 Coexistence of chaotic and regular structures at $E = -0.275$ 101

4.9 Diminishing regular region at $E = -0.2499$ 102

4.10 Islands of high-order resonance from the previous figure. 102

4.11 Complete chaos at $E = -0.05$ 103

4.12 Emergence of regular structure at $E = 1$ 104

4.13 Expansion of regular region at $E = 10$ 104

4.14 Dominance of regular structure at $E = 1000$ 105

CHAPTER ONE

LANDAU-GINZBURG MODEL OF UNIAXIAL FERROMAGNETS

1.1 Introduction

Hamiltonian systems characterized by a parameter ϕ in a polynomial type potential of the fourth order (commonly refered to as the ϕ^4 field) arise quite frequently in the modelling of phase transitions as well as in an anharmonic perturbation theory of lattice vibrations. Like a vector, this parameter, in general, can have any number of components (ϕ_1, ϕ_2, …, ϕ_n). In this thesis, we shall focus only on those systems described by single-component order parameters and those described by two-component spatial parameters; they will be referred to as the single-component and the two-component systems, respectively. Landau [1] proposed that a free energy expansion in even powers of an order parameter could describe second order phase transitions in the neighborhood of a critical point. The order parameter which distinguishes the order or the symmetry of two neighboring phases varies continuously from zero to some finite non-zero value as the system evolves from the disordered phase to the ordered one. When high order interaction terms beyond the fourth order are ignored, this phenomenological free energy expansion leads to single-component systems described exactly by the ϕ^4 field. These systems are highly nonlinear; nevertheless, they are deterministic. Solutions to their equations of motion include those which are of solitary-wave type.

Systems of the ϕ^4 field class have been studied extensively for a number of years. Efforts have been put in to obtain exact solutions as well as the thermodynamic properties of these systems [2]-[4]. Krumhansl and Schrieffer [5] were among the first to obtain exact solutions to the system whose potential is given by

$(\phi^2 - 1)^2/8$, while Scalapino et al. [6] sought thermodynamical properties of a one-dimensional Landau-Ginzburg system. These investigations were, however, aimed at single-component systems in low dimensions, while much more interesting physics and solutions occur in higher dimensions. Although Bishop and Krumhansl [7] did attempt to generalize their earlier model to include two and three-dimensional systems, they assumed a highly anistropic medium so that the order parameter varied in one direction only. Their model therefore has limited applicability.

Generalizations to multicomponent fields can be directly related to systems characterized by coupled parameters. For example, a metamagnet possessing two inequivalent magnetic sublattices [8] is described by two order parameters which can be chosen to be the z-components of the magnetizations of the two sublattices. The order parameters are thus mutually coupled and, in addition, interact with an external magnetic field. Another example is the displacement field in the anharmonic perturbation phonon theory. Such systems lead to nonlinear coupled equations of motion, chaos thus can be inevitable.

In this thesis, we intend to introduce generalizations of the ϕ^4 field model to include three-dimensional (in space) single-component systems in which the order parameters are allowed to vary in all three directions. Also, we aim to contrast the deterministic property of single-component systems with the chaotic behavior of coupled two-component systems. We will look at systems characterized by single-component order parameters in the first two chapters. We will devote the first chapter to review some of the exact solutions to the three-dimensional Landau-Ginzburg model applied to a uniaxial ferromagnet found by Winternitz et al. [11] and to introduce numerical techniques for the test of stability for these solutions. The potential involved here is also a fourth order polynomial; however, it does not form a complete square and its coefficients can be temperature- and pressure-dependent. Therefore, this ϕ^4 potential is different from that already examined by

Krumhansl and Schrieffer [5]. Then, in Chapter Two, we will introduce a generalization of the model to include a weak magnetic field and review some of the exact solutions found recently by Winternitz et al. [12]. By the method of numerical analysis, we will investigate the field dependence of these solutions so as to make comparison with those in the absence of a magnetic field. Finally, we will look at systems characterized by two-component spatial parameters with coupling. In Chapter Three, we will begin with the controversial x^2y^2 potential problem. The system is largely chaotic. A very small stable region has been found only recently by Dahlqvist and Russberg [9]. We will examine the actual trajectories traced out by the two-component spatial parameter $\vec{r} = x\vec{i} + y\vec{j}$ and introduce perturbative techniques to model the dynamics of the system. We will also use perturbative analysis to explain the observed bifurcation phenomenon. In the final chapter, Chapter Four, we will explore anharmonic perturbation theory of lattice vibrations. The anharmonicity of the lattice eventually leads to a system described by a two-component spatial parameter. The coupling between these components gives rise to two nonlinear coupled equations of motion. Instead of looking at the actual trajectories in real coordinate-space, we will cast the system's chaotic motions onto Poincaré sections with the aid of numerical techniques. We will show that whether the system behaves chaotically is determined by the system's energy level in relation to the effective potential.

1.2 The Model

The Landau model has been used extensively to study phase transitions in one-component order-parameter systems, in particular, systems uniquely characterized by the value of the z-component of the magnetization [8]. The free energy F of such systems is usually written in the form

$$F = B_2\eta^2 + B_4\eta^4 + B_6\eta^6 + \cdots, \tag{1.1}$$

where η, the order-parameter, determines the symmetry of the phases. For the disordered phase (the high temperature phase), $\eta = 0$. For the ordered one (the low temperature phase), η is non-zero and finite. The coefficients in the above expansion are considered temperature- and pressure-dependent [1]. This model, however, is not very realistic since it only measures the mean field property of the system and does not take into account the spatial variation of the order parameter. To remove this deficiency, we introduce the Landau-Ginzburg free energy expansion [10] and, as an example, we apply this expansion to describe the free energy density f of a uniaxial ferromagnet:

$$f = f_0 + \frac{1}{2}AM^2 + \frac{1}{4}BM^4 + \frac{1}{6}CM^6 + D\left|\vec{\nabla}M\right|^2 \tag{1.2}$$

where f_0 is a temperature-dependent parameter (free energy density of the nonmagnetic phase) and the z-component of the magnetization $M(\vec{r})$ is the order-parameter. The coefficient A is assumed to take the form $A = \alpha(T - T_c)$ where $\alpha > 0$ and T_c is the transition (critical) temperature [1]. Hence, A changes sign at the critical temperature T_c. The coefficient B can take on an arbitrary sign; however, the transition is of first order if $B < 0$ and of second order if $B \geq 0$. The coefficient C must necessarily be positive for stability reasons. This can be deduced directly from the Landau model [1]. The difference between the two models comes from the last term on the right of (1.2). This gradient term measures the spatial variation of the order-parameter $M(\vec{r})$; hence, the magnetic inhomogeneity of the system is built into the model. In this chapter, we will concern ourselves only with the second order continuous transitions. Therefore, we take $B > 0$.

Exact solutions of this model have been found by Winternitz et al. [11] using the method of symmetry reduction. They have shown that their solutions correspond to physical processes and can be classified according to their symmetry properties. However, the thermodynamics of these solutions has not been presented. We feel that this is crucial in determining whether a solution is physically admissible. Therefore, in this chapter, we will first outline the method used in the publication by Winternitz et al. and review some of their results [11]. Then, by numerical analysis, we will obtain empirical expressions for the partition function for some of the solutions and calculate the specific heats accordingly.

1.3 Equation of Motion

To obtain the time evolution equation for the order-parameter $M(\vec{r})$, we make use of the Onsager relation

$$\frac{\partial M}{\partial t} = -\Gamma \frac{\delta f}{\delta M} \tag{1.3}$$

which describes the system's evolution toward its thermodynamic equilibrium. The coefficient Γ is called the Landau-Khalathikov damping coefficient and $\delta f/\delta M$ denotes the functional derivative of f with respect to M. Then, the equation of motion for steady states is obtained by setting the time derivative on the left of (1.3) to zero. If we consider terms only up to third order, the equation of motion is written as

$$\vec{\nabla}^2 M = \frac{1}{2D}(AM + BM^3). \tag{1.4}$$

According to the method of symmetry reduction, solutions to this equation can be classified by their symmetry properties. It has been discovered that its solutions consist of a translationally-invariant group, a cylindrically- and a spherically-symmetric group, and an invariant subgroup with dilation [11]. We shall focus ourselves on the first invariant group, and in particular, look for solutions of the form

$$M(\vec{r}) = P(\xi) \tag{1.5}$$

$$\xi = \xi(\vec{r}) = z. \tag{1.6}$$

Therefore, we are simply looking at the variations of the solutions in the z-direction only and ignoring their variations in the x- and the y-directions. These particular solutions are actually in accordance with the translational symmetry of the crystal, which is a fundamental property of the crystal, and so they represent the most physically meaningful solutions. Assuming (1.5) and (1.6) in equation (1.4) reduces the equation of motion to a second order differential equation [11] with one independent variable ξ

$$\frac{d^2P}{d\xi^2} = \frac{1}{2D}(AP + BP^3) \tag{1.7}$$

which can be integrated once to give

$$\left(\frac{dP}{d\xi}\right)^2 = \frac{B}{4D}\left(P^4 + \frac{2A}{B}P^2 + \frac{4\gamma}{B}\right) \tag{1.8}$$

where γ is the integration constant and is determined by the initial conditions

$$\begin{aligned} \dot{P}(\xi_0) &= \dot{P}_0 \\ P(\xi_0) &= P_0. \end{aligned} \tag{1.9}$$

The constant γ is then found to be expressed as

$$\gamma = D\dot{P}_0^2 - \frac{A}{2}P_0^2 - \frac{B}{4}P_0^4. \tag{1.10}$$

Equation (1.8) can be written in a more familiar (standard elliptic) form

$$\left(\frac{dP}{d\xi}\right)^2 = \Delta(P^2 - P_1^2)(P^2 - P_2^2) \tag{1.11}$$

where $\Delta = B/4D$, $P_1^2 + P_2^2 = -2A/B$ and $P_1^2P_2^2 = 4\gamma/B$, and can be solved by various Jacobian elliptic functions depending on the roots of the polynomial that appear on the right-hand side of equation (1.11):

$$\begin{aligned} R(P) &= \Delta(P^2 - P_1^2)(P^2 - P_2^2) \qquad (1.12)\\ &= \Delta\left(P^4 + \frac{2A}{B}P^2 + \frac{4\gamma}{B}\right). \qquad (1.13)\end{aligned}$$

Interestingly, if any of the roots coincide, the solution is expressible in terms of elementary functions. We look for real solutions so that $\dot{P}^2 \geq 0$. Figure 1.1 displays plots of $\dot{P}^2$ as a function of P for all possible cases in which real solutions exist. We shall go through this list in sequential order in the following section.

1.4 Solution

a) Trivial Solution

The most trival solutions to equation (1.11) are the constant solutions:

$$\begin{aligned} P(\xi) &= 0 \qquad (1.14)\\ P(\xi) &= \pm\sqrt{\frac{-A}{B}} \qquad (1.15)\end{aligned}$$

where $A < 0$. These solutions represent the homogeneous mean fields due to the background magnetization for $T < T_c$. Hence, solution (1.15) implies an homogeneous magnetic medium while solution (1.14) implies a non-magnetic one.

b) Solutions Corresponding to Real Roots

The conditions for the existence of real roots are $0 \leq \gamma \leq A^2/4B$ and $A \leq 0$. The solutions in this case consist of elementary functions as well as Jacobian elliptic functions.

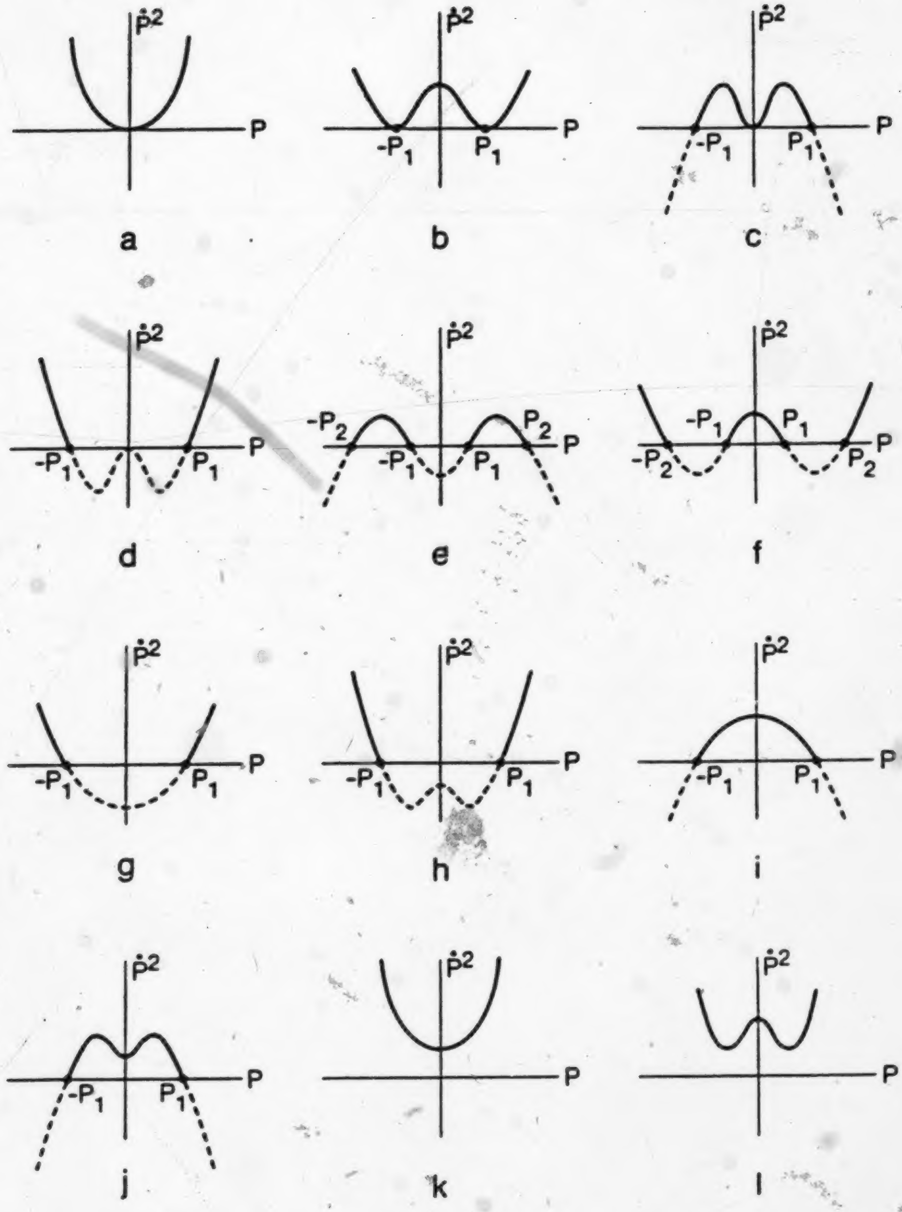

Figure 1.1: Plots of $\dot{P}^2$ as a function of P. These are the possible cases in which real solutions exist.

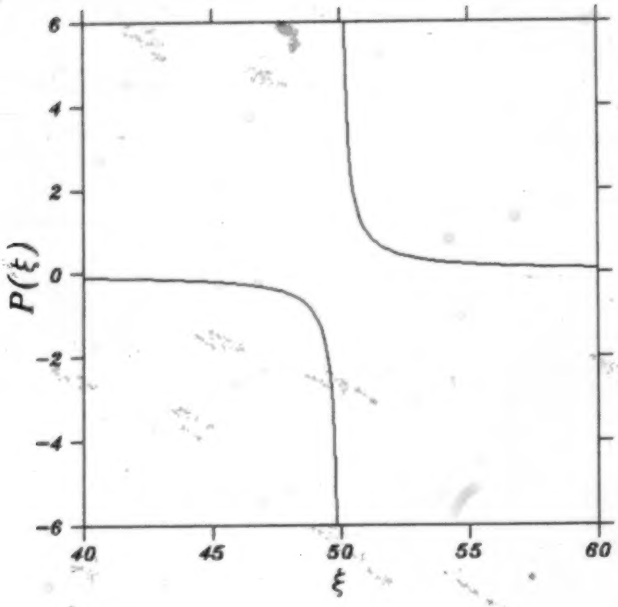

Figure 1.2: Solution of (1.16) with a plus sign.

One Quadruple Root

When $A = 0$ and $\gamma = 0$, the roots coincide as shown in Fig. 1.1a. The quadruple root is given by $\pm P_1 = \pm P_2 = 0$. The solution, for $\Delta = B/4D > 0$, is

$$P(\xi) = \frac{\pm 1}{\sqrt{\Delta}(\xi - \xi_0)} \tag{1.16}$$

and is shown in Fig. 1.2. The solution approaches $\pm\infty$ at $\xi = \xi_0$. Such an unphysical behavior is possibly caused by the continuum approximation. The discreteness effect is critically affecting the solution's behavior in a spatial extent less than the equilibrium spacing between the atoms. However, this singularity can be taken as an indication of saturation. The magnetization reaches its saturated value as the plane $\xi = \xi_0$ is approached and abruptly reverses its direction as it crosses the plane. At large distances from the plane, the magnetization falls to zero. Therefore, the solution best describes the occurrence of a magnetic double-layer in a non-magnetic medium. However, the solution only exists when $A = 0$. By assumption, $A = \alpha(T - T_c)$ and $\alpha > 0$. This means, the solution is physically realizable only at the critical temperature.

Two Double Roots

If the integration constant $\gamma = A^2/4B$, $A < 0$ and $\Delta > 0$, then the polynomial (1.12) has two double roots as shown in Fig. 1.1b. They are

$$\pm P_1 = \pm P_2 = \pm\sqrt{\frac{-A}{B}} \tag{1.17}$$

Depending on the magnitude of P, two types of solutions are available. First, for $-P_1 \le P \le P_1$, the solution is

$$P(\xi) = \epsilon P_1 \tanh[\sqrt{\Delta} P_1(\xi - \xi_0)] \tag{1.18}$$

where $\epsilon = \pm 1$. The solution is shown Fig. 1.3 for $\epsilon = 1$. It suggests that the magnetization saturates in two opposite directions as it moves away from the $\xi = \xi_0$ plane. Near the plane, the magnetization reverses its direction smoothly and continuously. The solution therefore corresponds to a domain wall.

Secondly, for $P > P_1$ or $P < -P_1$, the real solution is given by

$$P(\xi) = \epsilon P_1 \coth[\sqrt{\Delta} P_1(\xi - \xi_0)] \tag{1.19}$$

where $\epsilon = \pm 1$. The solution, as shown in Fig. 1.4, is singular at the $\xi = \xi_0$ plane and approaches a constant value at large distances. It therefore represents a magnetic double-layer in an homogeneous background. Although (1.18) and (1.19) are both candidate solutions to equation (1.11) at any temperature $T < T_c$, the actual solution is determined by the initial conditions (1.9).

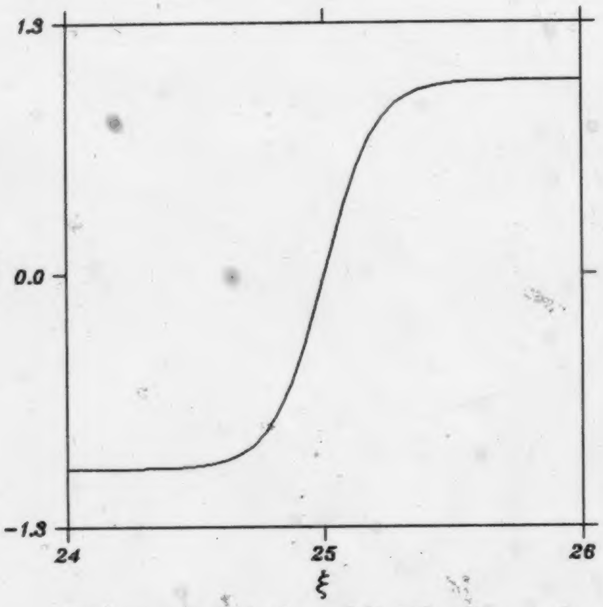

Figure 1.3: Solution of (1.18) with $\epsilon = 1$.

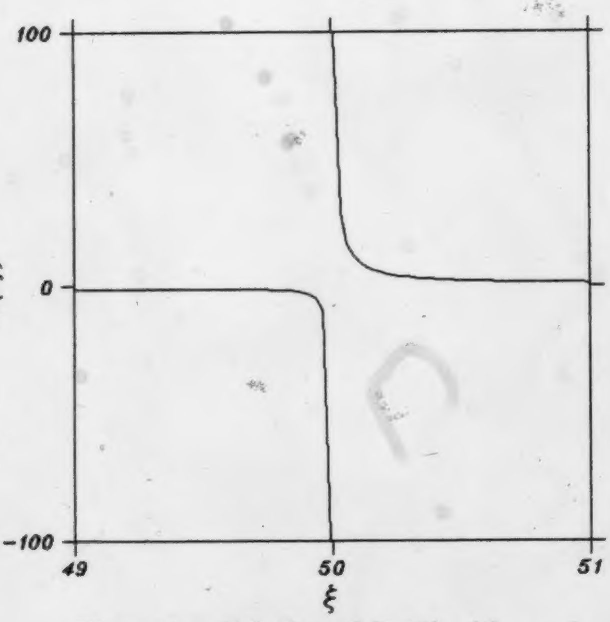

Figure 1.4: Solution of (1.19) with $\epsilon = 1$.

One Double and Two Simple Roots

When $\gamma = 0$ and $A < 0$, there exist one double and two simple real roots:

$$\begin{aligned} P_2 &= -P_2 = 0 \\ \pm P_1 &= \pm\sqrt{\frac{-2A}{B}}. \end{aligned} \tag{1.20}$$

For $\triangle < 0$ (Fig. 1.1c), the corresponding real solutions are

$$P(\xi) = \frac{\epsilon P_1}{\cosh[\sqrt{-\triangle} P_1(\xi - \xi_0)]} \tag{1.21}$$

where

$$\epsilon = \begin{cases} 1, & 0 \le P \le P_1; \\ -1, & -P_1 \le P \le 0. \end{cases}$$

The solution for $\epsilon = 1$ is shown in Fig. 1.5. Magnetization is strongly localized in one direction near the plane $\xi = \xi_0$ and decays rapidly to zero away from it. This process corresponds to the nucleation of a magnetic center, which could be, for example, initiated by thermal fluctuations. For $\triangle > 0$ (Fig.1.1d), the solution is expressed in terms of a trigonometric function:

$$P(\xi) = \frac{\epsilon P_1}{\cos[\sqrt{\triangle} P_1(\xi - \xi_0)]} \tag{1.22}$$

where

$$\epsilon = \begin{cases} 1, & P > P_1; \\ -1, & P < -P_1. \end{cases}$$

It has a period $T = 2\pi/\sqrt{\triangle}P_1$ and singularities at

$$\xi - \xi_0 = (2n+1)\frac{\pi}{2\sqrt{\triangle}P_1}$$

where $n = 1, 2, \cdots$. According to Fig. 1.6, the solution suggests a periodic formation of magnetic double-layers of opposite magnetizations at $T < T_c$ and the

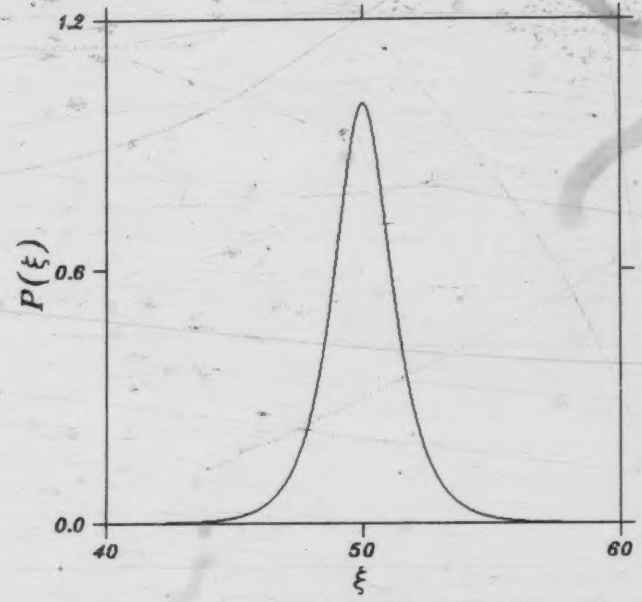

Figure 1.5: Solution of (1.21) with $\epsilon = 1$.

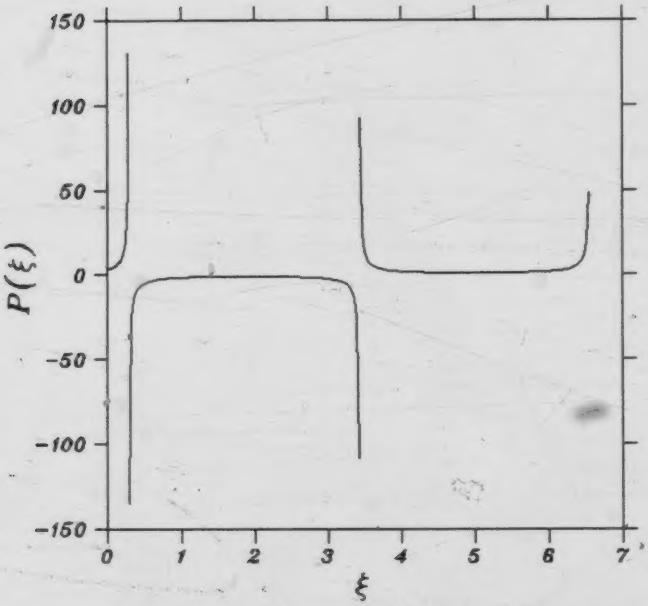

Figure 1.6: Solution of (1.22) with $\epsilon = 1$.

magnetization in each layer becomes saturated in the neighborhood of the layer's boundary.

Four Real Simple Roots

When $0 < \gamma < A^2/4B$ and $A < 0$, the roots of (1.12) are written as

$$\pm P_2 = \pm\left(\frac{-A}{B} + \frac{1}{2}\sqrt{\frac{4}{B}(\frac{A^2}{B} - 4\gamma)}\right)^{\frac{1}{2}} \qquad (1.23)$$

$$\pm P_1 = \pm\left(\frac{-A}{B} - \frac{1}{2}\sqrt{\frac{4}{B}(\frac{A^2}{B} - 4\gamma)}\right)^{\frac{1}{2}}, \qquad (1.24)$$

so that $|P_2| > |P_1| > 0$. For $\Delta < 0$ (Fig. 1.1e), the real solution is written in terms of the Jacobian elliptic function [13]

$$P(\xi) = \epsilon P_2 dn[\sqrt{-\Delta}P_2(\xi - \xi_0), k] \qquad (1.25)$$

where $k = (1 - P_1^2/P_2^2)^{\frac{1}{2}}$ is the modulus of $dn(u, k)$, and

$$\epsilon = \begin{cases} 1, & P_1 \le P \le P_2; \\ -1, & -P_2 \le P \le -P_1, \end{cases}$$

The Jacobian elliptic function $dn(u, k)$ is defined as

$$dn(u, k) = \frac{\pi}{2K} + \frac{2\pi}{K}\sum_{n=1}^{\infty}\frac{q^n}{1 + q^{2n}}\cos(\frac{n\pi u}{K}) \qquad (1.26)$$

where $K = K(k)$ is the complete elliptic integral, $q = \exp(-\pi K(k')/K(k))$ and $k' = \sqrt{1 - k^2}$ the complementary modulus [13]. As shown in Fig. 1.7, $dn(u, k)$ is periodic. Its period T can be found by setting

$$\cos\left\{\frac{n\pi\sqrt{-\Delta}P_2[(\xi - \xi_0) + T]}{K}\right\} = \cos\left\{\frac{n\pi\sqrt{-\Delta}P_2[\xi - \xi_0]}{K}\right\}, \qquad (1.27)$$

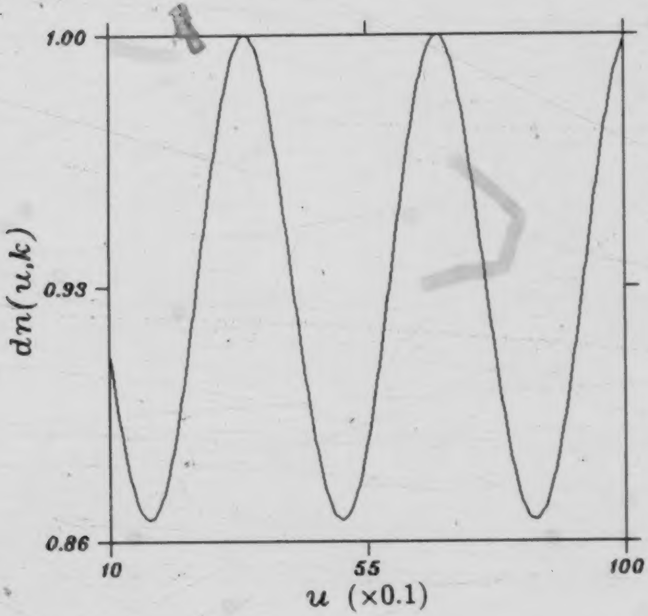

Figure 1.7: The $dn(u,k)$ Jacobian elliptic function.

for $n = 1, 2, \cdots$. This can be satisfied only if

$$T = \frac{2K(k)}{\sqrt{-\triangle P_2}}. \tag{1.28}$$

These solutions correspond to two possible branches of ferromagnetic spin waves at $T < T_c$ oscillating on top of an homogeneous background.

For $\triangle > 0$ (Fig. 1.1f) and $-P_1 \leq P \leq P_1$, the solution is given by another type of Jacobian elliptic function

$$P(\xi) = P_1 sn[\sqrt{\triangle} P_2(\xi - \xi_0), k] \tag{1.29}$$

where $k = P_1/B$ is the modulus of $sn(u, k)$ [13]. As shown in Fig. 1.8, the Jacobian elliptic function $sn(u, k)$ is again periodic and is defined as

$$sn(u, k) = \frac{2\pi}{kK} \sum_{n=1}^{\infty} \frac{q^{n-\frac{1}{2}}}{1 - q^{2n-1}} \sin[(2n-1)\frac{\pi u}{2K}] \tag{1.30}$$

where K and q are defined as above [13]. Following similar steps, the period of (1.29) is found to be $T = 4K(k)/\sqrt{\triangle} P_2$. However, the solution behaves very much like a sine wave, oscillating around the horizontal axis. Therefore, it is interpreted as antiferromagnetic spin waves. For $P \geq P_2 > P_1$ or $P \leq -P_2 < -P_1$, the solution is still periodic but singular [13]:

$$P(\xi) = P_2 sn[\sqrt{\triangle} P_2(\xi - \xi_0), k]^{-1}. \tag{1.31}$$

The solution has a period $T = 4K/\sqrt{\triangle} P_2$, a modulus $k = P_1/P_2$ and singularities at

$$(\xi - \xi_0) = \frac{2nK}{\sqrt{\triangle} P_2} \tag{1.32}$$

for $n = 1, 2, \cdots$. Then, according to Fig. 1.9, the solution can be interpreted again as a periodic arrangement of magnetic double layers in an homogeneous mean field background.

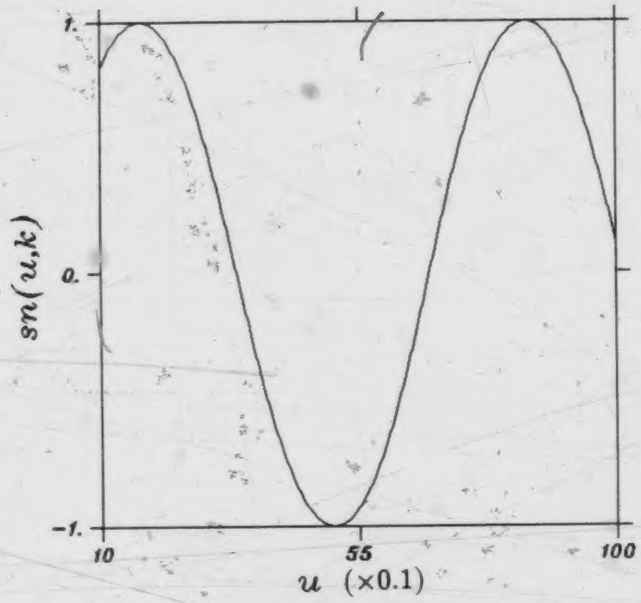

Figure 1.8: The $sn(u,k)$ Jacobian elliptic function.

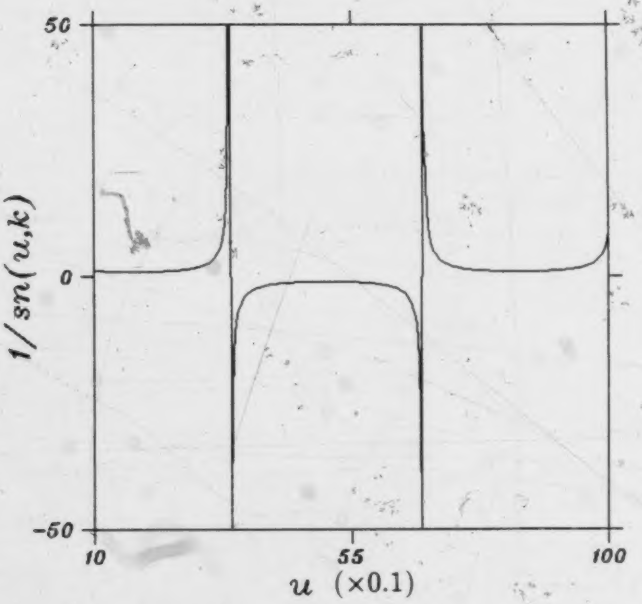

Figure 1.9: The periodic singular solution of (1.31) for $P_2 = 1$.

c) Two Real and Two Purely Imaginary Roots

If the integration constant $\gamma \leq 0$, then there exist two real and two imaginary roots and, for any A, they are written respectively as

$$\begin{aligned} \pm P_1 &= \pm r \\ \pm P_2 &= \pm iq \end{aligned} \qquad (1.33)$$

where both r and q are real and positive.

One Real Double Root and Two Purely Imaginary

Only if $A > 0$ and $\gamma = 0$, does the polynomial (1.12) have one real double and two purely imaginary roots (Fig. 1.1a): $\pm P_1 = \pm r = 0$, and $\pm P_2 = \pm iq$. Then, for $\Delta > 0$, the solution is given in terms of a hyperbolic sine function:

$$P(\xi) = \pm q \left\{ \sinh[\sqrt{\Delta} q(\xi - \xi_0)] \right\}^{-1}. \qquad (1.34)$$

The solution is singular at $\xi = \xi_0$ as shown in Fig. 1.10. It thus implies saturation of the magnetization in opposite directions on each side of the plane $\xi = \xi_0$. However, the magnetization decays to zero as it moves away from ξ_0. It means that the saturation takes place in the absence of a homogeneous background. Thus, the solution can be regarded as a magnetic double layer in a non-magnetic sample at $T > T_c$.

Two Simple Real and Two Purely Imaginary Roots

If $\gamma \neq 0$ but $\gamma < 0$, then there exist two simple real roots and two purely imaginary ones. Since Δ and A can take on arbitrary signs, there are four possibilities:

(a) $\Delta > 0$, $A \geq 0$ (Fig. 1.1g),

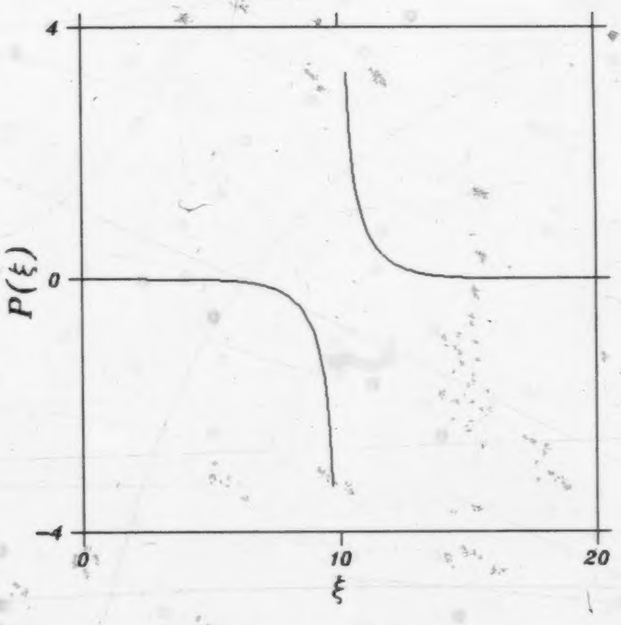

Figure 1.10: Solution of (1.34) with a plus sign.

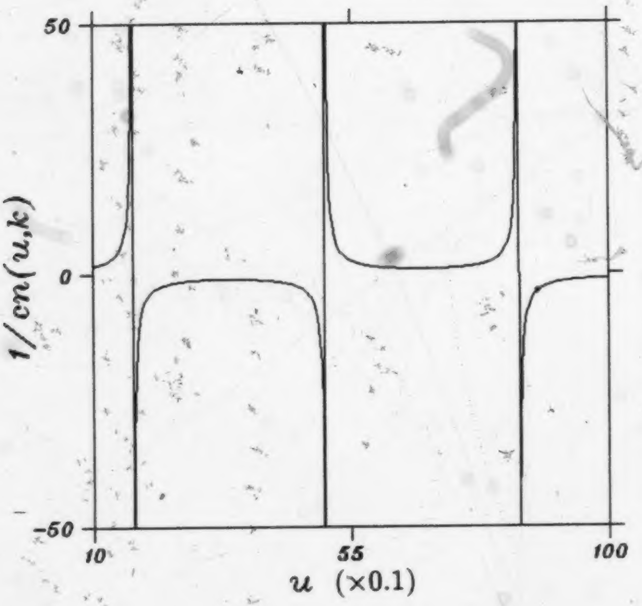

Figure 1.11: The periodic singular solution of (1.35).

(b) $\triangle > 0$, $A < 0$ (Fig. 1.1h),

(c) $\triangle < 0$, $A \geq 0$ (Fig. 1.1i),

(d) $\triangle < 0$, $A < 0$ (Fig. 1.1j).

The roots are given as in (1.33). The solutions to (**a**) and (**b**) are of the same form and, for $P \geq P_1$ or $P \leq -P_1$, they are written in terms of Jacobian elliptic functions:

$$P(\xi) = r\left\{cn[\sqrt{\Delta(r^2+q^2)}(\xi-\xi_0), k]\right\}^{-1} \tag{1.35}$$

where $k^2 = q^2/(r^2+q^2)$ [13]. A sketch of the solution is shown in Fig. 1.11. It has a period $T = 4K(k)/\sqrt{\Delta(r^2+q^2)}$ and singularities at $(\xi - \xi_0) = (2n + 1)K/\sqrt{\Delta(r^2+q^2)}$ where n is an integer. Again, the solution represents a periodic formation of magnetic double layers of opposite magnetizations in a homogeneous

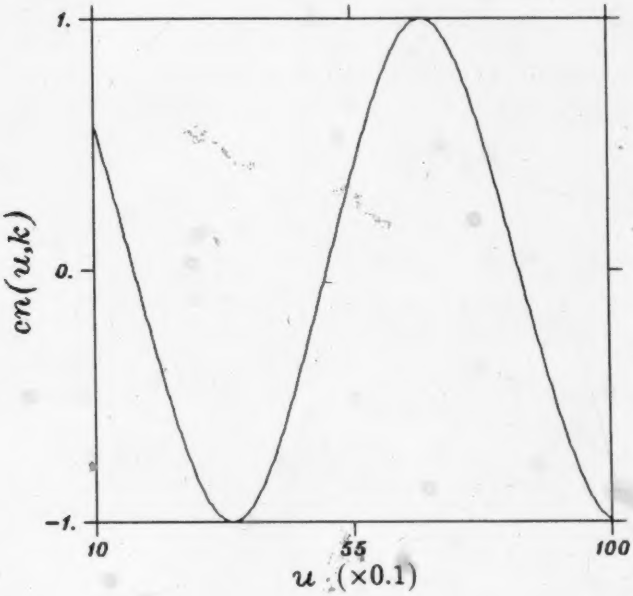

Figure 1.12: The $cn(u,k)$ Jacobian elliptic solution of (1.36).

mean-field background. The real solutions corresponding to the case (**c**) and (**d**) are also of the same form but finite. They are represented by

$$P(\xi) = rcn[\sqrt{-\Delta(r^2+q^2)}(\xi-\xi_0), k] \tag{1.36}$$

for $-P_1 \leq P \leq P_1$ [13]. It has a real period $T = 4K/\sqrt{-\Delta(r^2+q^2)}$ and a modulus $k = [r^2/(r^2+q^2)]^{\frac{1}{2}}$. Since the solutions oscillate around the horizontal axis as shown in Fig. 1.12, they can be interpreted as antiferromagnetic spin waves. Note that the modulus k is limited to the range $(0,1)$. It can be demonstrated that for $A \geq 0$, $1/\sqrt{2} > k > 0$ and for $A < 0$, $1 > k > 1/\sqrt{2}$. Hence, the four cases (**a**)-(**d**) exploit the full range of k exhaustively.

d) Solutions Corresponding to Four Purely Imaginary Roots

If $A > 0$, $\Delta > 0$ and $0 < \gamma \leq A^2/4B$, the roots are all purely imaginary (Fig. 1.1k) and given by

$$\begin{aligned} \pm P_1 &= \pm qi \\ \pm P_2 &= \pm si \end{aligned} \tag{1.37}$$

such that $0 < q < s$.

Two Double Roots

However, if $\gamma = A^2/4B$, the polynomial (1.12) has two double imaginary roots: $\pm P_1 = \pm P_2 = \pm\sqrt{A/B}i = \pm qi$, and the solution is simply trigonometric

$$P(\xi) = q\tan[\sqrt{\Delta}q(\xi - \xi_0)] \tag{1.38}$$

with a period $T = \pi/q\sqrt{\Delta}$ and simple poles at $(\xi - \xi_0) = (2n+1)\pi/(2q\sqrt{\Delta})$ for $n = 1, 2, \cdots$. Therefore, the solution represents a periodic structure of magnetic layers. Similar to a spin wave in the domain wall, the magnetization reverses its direction smoothly and continuously in each layer.

Four Simple Roots

If $0 < \gamma < A^2/4B$, the roots are given as in (1.37). The solution is singular and periodic:

$$P(\xi) = q\,tn[\sqrt{\Delta}s(\xi - \xi_0), k] \tag{1.39}$$

where $tn(u, k)$ is another Jacobian elliptic function and $k^2 = 1 - q^2/s^2$ is the square of the modulus [13]. The solution has a real period $T = 2K(k)/s\sqrt{\Delta}$ and singularities at $(\xi - \xi_0) = (2n + 1)K(k)/s\sqrt{\Delta}$ where n is an integer. According to Fig. 1.13, it

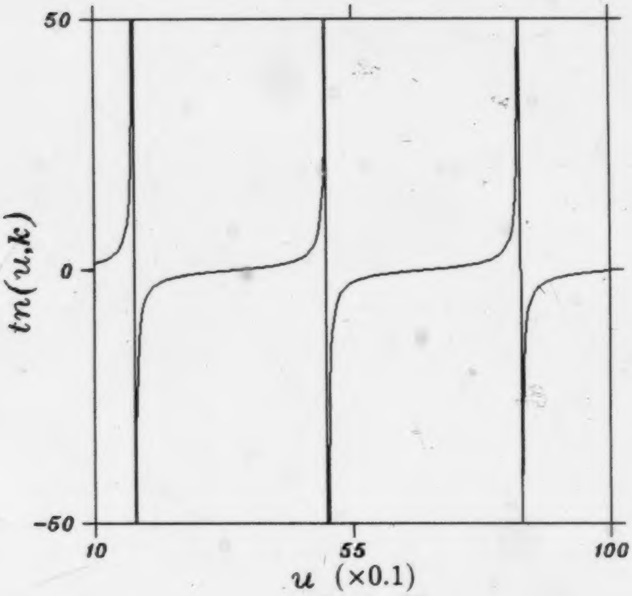

Figure 1.13: The $tn(u,k)$ Jacobian elliptic function.

also represents a periodic configuration of magnetic layers with magnetization that resembles a spin wave in a domain wall.

e) Solutions Corresponding to Four Complex Roots

When $\Delta > 0$ and $\gamma > A^2/4B$ the roots are all complex (Fig. 1.1k, l) and written as

$$\begin{aligned} \pm P_1 &= \pm(p+iq) \\ \pm P_2 &= \pm(p-iq) \end{aligned} \tag{1.40}$$

so that p and q are both real and positive. The solutions in this case are singular and periodic:

$$P(\xi) = \sqrt{p^2+q^2}\left\{tn[\sqrt{\Delta(p^2+q^2)}(\xi-\xi_0),k]dn[\sqrt{\Delta(p^2+q^2)}(\xi-\xi_0),k]\right\}^{-1} \tag{1.41}$$

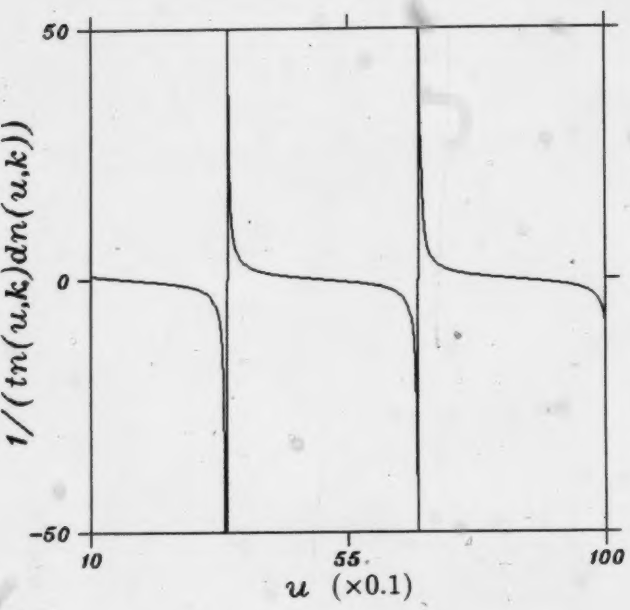

Figure 1.14: The periodic singular solution of (1.41).

where $k^2 = p^2/(p^2+q^2)$ [13]. One of these solutions is depicted in Fig. 1.14. It has a period $T = 2K(k)/\sqrt{\Delta(p^2+q^2)}$ and singularities at $(\xi-\xi_0) = 2nK(k)/\sqrt{\Delta(p^2+q^2)}$ for any integer n. It can be interpreted as a periodic arrangement of isolated magnetic layers in a nonmagnetic sample.

Therefore, by the method of elliptic integration, we are able to solve the equation of motion (1.8) exactly. In addition to the temperature, the integration constant γ adds an extra degree of freedom to the system to admit a great variety of solutions: homogeneous mean fields, double magnetic layers, single magnetic layers, ferromagnetic spin waves, antiferromagnetic spin waves, domain walls, etc. For a given temperature, many solutions are simultaneously available. However, they do not necessarily correspond to the stable equilibria of the system. Some may be metastable, or even unstable solutions. The solutions that can be realized physically would be energetically more favorable and if we interpret the situation statistically, the solutions would correspond to higher probabilities. One way to test the stability of a solution is to calculate its specific heat. An unstable solution is then characterized by a negative specific heat value. To demonstrate the method explicitly, we shall calculate the specific heats for two types of solutions, namely, the antiferromagnetic spin waves (the $sn(u,k)$ and the $cn(u,k)$ solutions) and the ferromagnetic spin waves (the $dn(u,k)$ solutions). To begin, we need to derive an analytic expression of the free energy for these special cases.

1.5 Free Energy

The total free energy is obtained by integrating the free energy density (1.2) over the volume of the sample

$$F = \int f(M, |\vec{\nabla} M|^2) d^3x. \tag{1.42}$$

If we consider only the translationally-invariant solutions (1.5) and (1.6), the above integral is written as

$$F = S_\perp \int_0^l \left\{ f_0 + \frac{A}{2}P^2 + \frac{B}{4}P^4 + D\dot{P}^2 \right\} d\xi \tag{1.43}$$

where $S_\perp$ and l are the cross-sectional area and the length of the sample, respectively. This integral is reduced to a much simpler form

$$\left(\frac{F}{S_\perp n}\right) = 4K(k)(f_0 - \frac{B\gamma}{4D}) + 2D\int_0^{4K(k)} \dot{P}^2(n\xi')d\xi' \tag{1.44}$$

if we make use of the equation of motion (1.8), scale the independent variable as $\xi' = \xi/n$ and assume that the length of the sample l is an exact integral multiple of the complete elliptic integral $K(k)$. That is, we assume $l = 4nK(k)$ where n is any positive integer. This assumption is to ensure that the longitudinal dimension of the sample matches up with the spatial periods of the ferromagnetic or the antiferromagnetic spin waves, so that standing waves are free to set up.

a) *The Ferromagnetic and The Antiferromagnetic Spin Waves*

The free energy expression for the $dn(u,k)$ waves can be obtained by substituting the solution (1.25) into the integral (1.44). This integral is then expressible in closed form [13]. The free energy per unit cross-sectional area of the sample is given by

$$\left(\frac{F}{S_{\perp}n}\right)_{dn} = 4K(k)(f_0 - \frac{B\gamma}{4D}) + \frac{4P_2}{3}\sqrt{-BD}[2K(k)P_1^2 - (P_1^2 + P_2^2)E(k)] \quad (1.45)$$

where $E(k)$ is the elliptic integral of the second kind [13]. Substituting the corresponding solution (1.29) or (1.36) in the integral (1.44), the free energy per unit cross-sectional area for the $sn(u,k)$ and the $cn(u,k)$ waves are written respectively as

$$\left(\frac{F}{S_{\perp}n}\right)_{sn} = 4K(k)(f_0 - \frac{B\gamma}{4D}) + \frac{4P_2}{3}\sqrt{BD}[K(k)(P_1^2 - P_2^2) + (P_1^2 + P_2^2)E(k)] \quad (1.46)$$

and

$$\left(\frac{F}{S_{\perp}n}\right)_{cn} = 4K(k)(f_0 - \frac{B\gamma}{4D}) + \frac{4}{3}\sqrt{-BD(r^2 + q^2)}[q^2K(k) + (r^2 - q^2)E(k)] \quad (1.47)$$

It is now clear that the temperature-dependent parameter f_0 and the integration constant γ represent the average energy densities not associated with the waves, they simply set the energy scale.

These free energy expressions can be converted to a dimensionless form. Their dependence on temperature and the integration constant γ is depicted in Fig. 1.15-1.18, where the scaled temperature $\epsilon = (T - T_c)/T_c$ has been used. For the purpose of comparison, the horizontal axes for each wave have been scaled to a common unit. The shapes of the curves are quite well preserved for all three cases and are very insensitive to temperature variations. For the $dn(u,k)$ waves, free energy drops nonlinearly with γ; whereas, the opposite is true for the $sn(u,k)$ waves. For the $cn(u,k)$ waves, whether $A > 0$ or $A < 0$, a local minimum is found

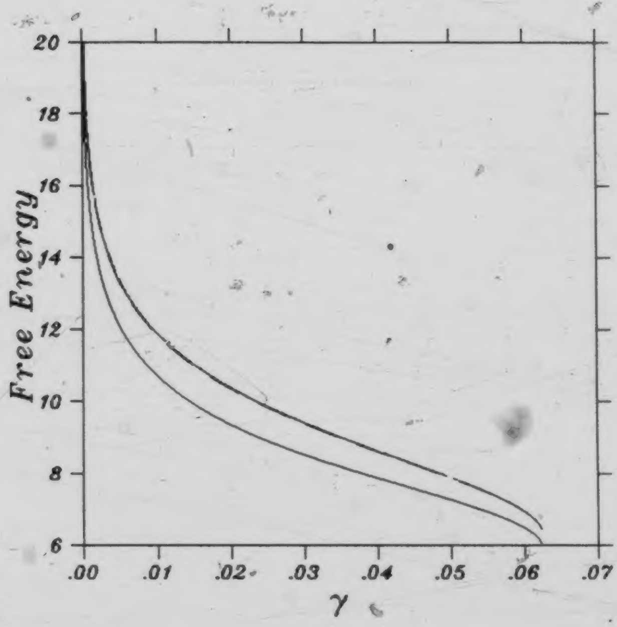

Figure 1.15: A comparison of the γ-dependence of the free energy for the $dn(u,k)$ elliptic waves at various temperatures. The lower curve represents $\epsilon = -1$ while the upper overlapping curves represent ϵ from -0.1 to -10^{-6}.

on each curve. This could be an indirect indication that in the case of dn or sn waves, no stable solution is available for any given temperature within the allowable range. On the contrary, in the case of cn waves, stable equilibrium states are clearly evident. They correspond to a particular choice of periodicity of the waves.

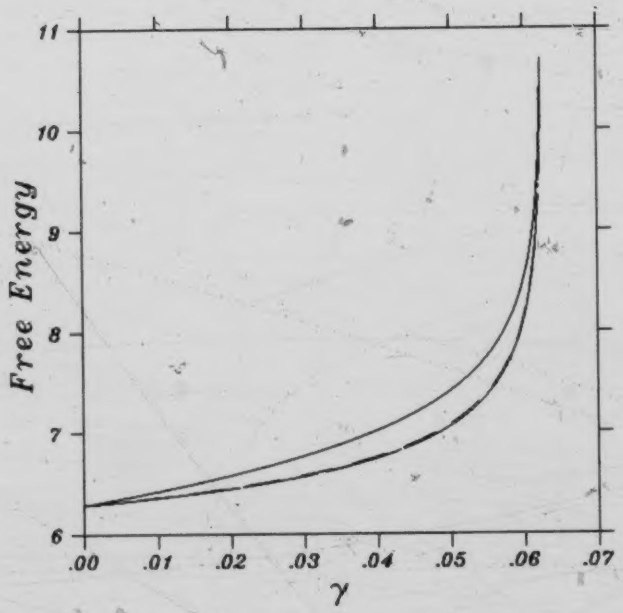

Figure 1.16: A comparison of the γ-dependence of the free energy for the $sn(u,k)$ elliptic waves at various temperatures. The upper curve represents $\epsilon = -1$ while the lower overlapping curves represent ϵ from -0.1 to -10^{-6}.

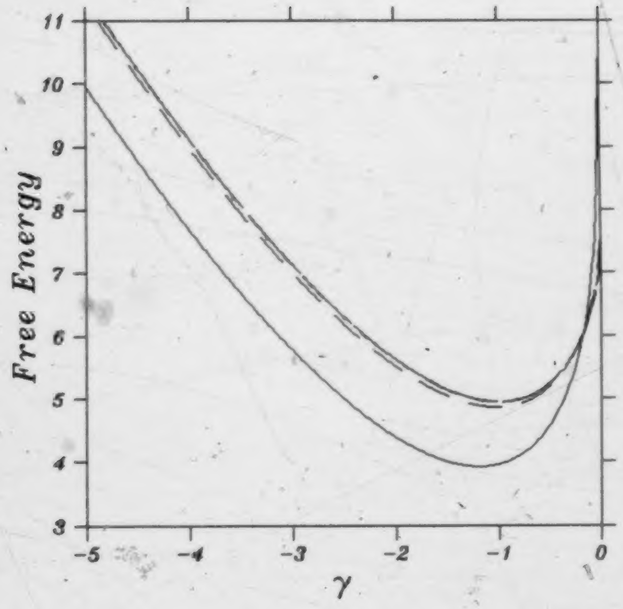

Figure 1.17: A similar comparison for the $cn(u,k)$ elliptic waves as in the previous two figures. Here, $\epsilon < 0$. The lower solid and the dashed curves correspond to $\epsilon = -1$ and $\epsilon = -0.1$ respectively. The upper overlapping curves correspond to ϵ from -0.01 to -10^{-6}.

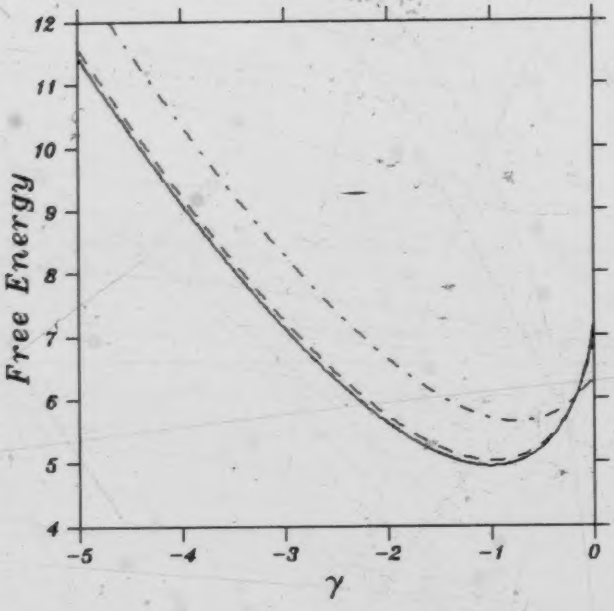

Figure 1.18: A similar comparison for the $cn(u,k)$ elliptic waves as in the previous figure. Here, $\epsilon > 0$. The upper and the lower dashed curves correspond to $\epsilon = 1$ and $\epsilon = 0.1$ respectively. The lower overlapping curves correspond to ϵ from 0.01 to 10^{-6}.

1.6 Partition Functions and Specific Heats

Having derived the analytic expressions for the free energies, we next calculate the partition function for each type of waves. Since there are two independent parameters, temperature and period, associated with each type of solutions, we denote the partition function of solution type Ω with period λ at temperature T by $\mathcal{Z}'_\Omega(T,\lambda)$. Then the total partition function $\mathcal{Z}_\Omega(T)$ is found by summing over all possible accessible states, in this case all possible λ. Therefore,

$$\mathcal{Z}_\Omega(T) = \sum_\lambda g(\lambda)\mathcal{Z}'_\Omega(T,\lambda) \tag{1.48}$$

where $g(\lambda)$ is the density of states or the degeneracy of the solution. The *dn* waves are doubly degenerate ($\epsilon = \pm 1$), therefore $g = 2$. However, the period λ is dependent on the roots of the polynomial (1.12) which in turn depend on the integration constant λ. Thus, the sum in (1.48) is equivalent to the sum over γ and the partition function is now written as

$$\mathcal{Z}_\Omega(T) = \sum_\gamma g(\gamma)\mathcal{Z}'_\Omega(T,\gamma). \tag{1.49}$$

The integration constant γ is a continuous parameter. Hence, in the continuum limit, the sum is converted to an integral

$$\mathcal{Z}_\Omega(T) = \int_{\gamma_l}^{\gamma_u} g(\gamma)\mathcal{Z}'_\Omega(T,\gamma)d\gamma \tag{1.50}$$

where γ_l and γ_u denote the lower and the upper limits of γ, respectively. Finally, for each set (T,γ), the partition function $\mathcal{Z}'_\Omega(T,\gamma)$ is related to the Helmholtz free energy $F_\Omega(T,\gamma)$ through $F_\Omega(T,\gamma) = -k_B T \ln(\mathcal{Z}'_\Omega)$ which gives

$$\mathcal{Z}'_\Omega(T,\gamma) = e^{-\beta F_\Omega(T,\gamma)} \tag{1.51}$$

where $\beta = 1/k_B T$ and k_B is the Boltzmann constant. Substituting this expression into (1.50), we obtain an integral relation between the total partition function and

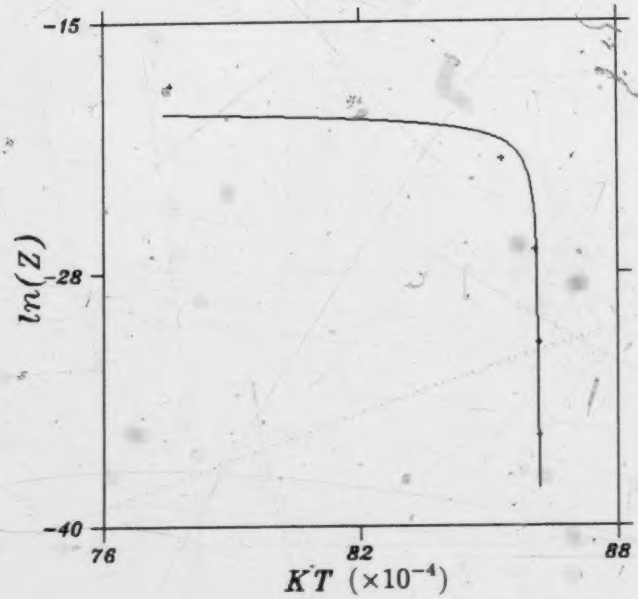

Figure 1.19: The partition function of the $dn(u,k)$ elliptic solutions. The solid line represents the empirical relation. The actual (numerical) data points are denoted by "+."

the Helmholtz free energy

$$\mathcal{Z}_\Omega(T) = \int_{\gamma_l}^{\gamma_u} g(\gamma) e^{-\beta F_\Omega(T,\gamma)} d\gamma. \tag{1.52}$$

Therefore, if we parametrize the energy curves in Fig. 1.15-1.18 for each temperature T, and integrate as described in (1.52), we obtain the empirical partition functions for the elliptic waves as functions of temperature. The results of such procedures are shown in Fig. 1.19-1.22. The temperature dependence of the partition functions is shown together with the corresponding empirical relations. The

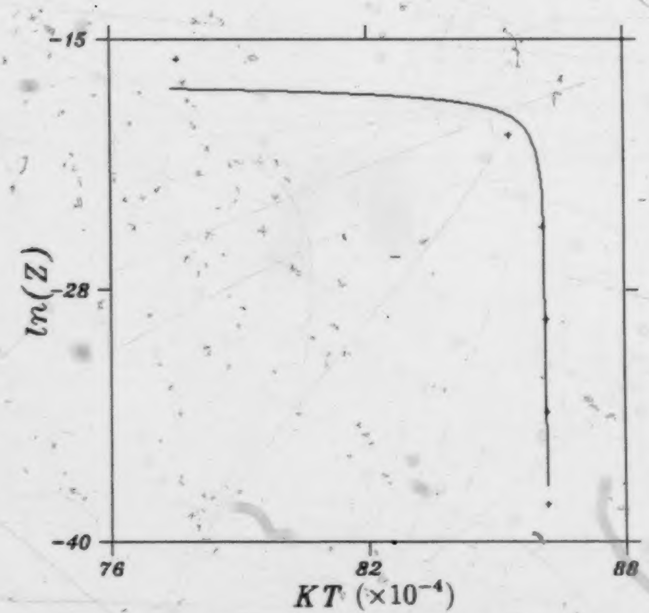

Figure 1.20: The partition function of the $sn(u, k)$ elliptic solutions.

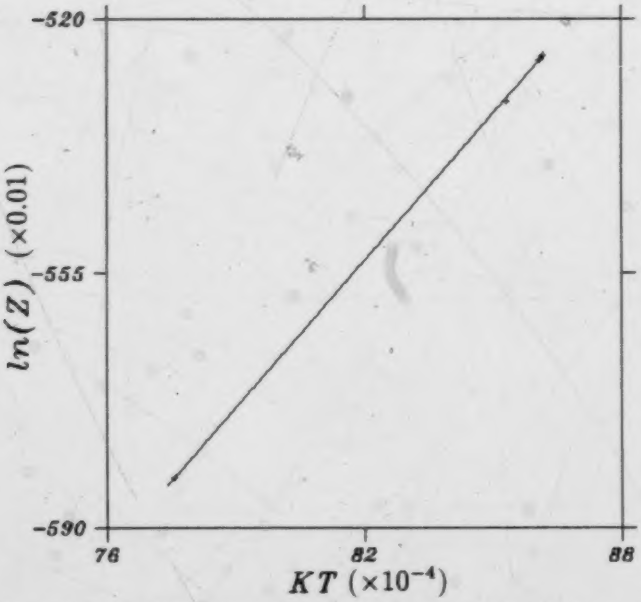

Figure 1.21: The partition function of the $cn(u, k)$ elliptic solutions for $\epsilon < 0$.

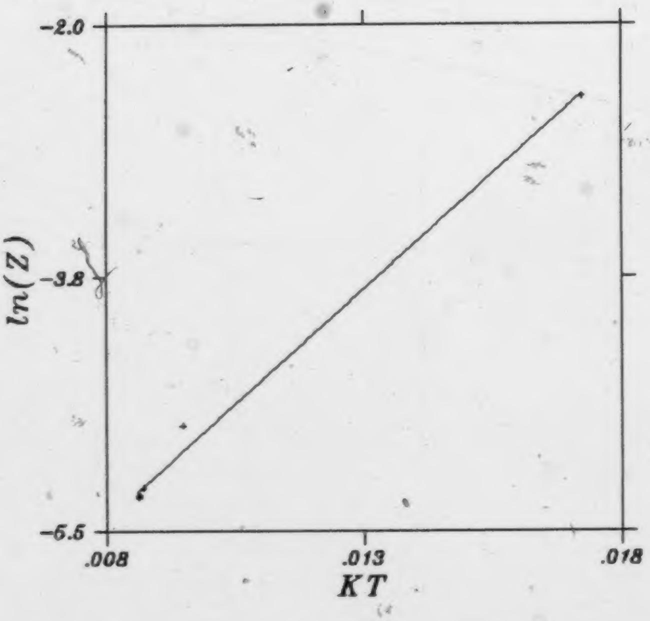

Figure 1.22: The partition function of the $cn(u,k)$ elliptic solutions for $\epsilon > 0$.

partition functions so obtained are listed as follows:

$$\ln(\mathcal{Z}_{dn}) = A/\sqrt{B-\beta^{-\frac{1}{4}}} + C,$$

$$\ln(\mathcal{Z}_{sn}) = A/\sqrt{B-\beta^{-\frac{1}{4}}} + D,$$

$$\ln(\mathcal{Z}_{cn}) = E/\beta + F \quad (\text{for } A > 0),$$

$$\ln(\mathcal{Z}_{cn}) = G/\beta + H \quad (\text{for } A < 0),$$

where the constants A, $B, \cdots$, G and H are respectively -0.054, 0.304688, -18.98, -16.89, 672.77, -11.05, 318.50 and -7.97. These expressions can then be used to derive various thermodynamic properties of the solutions. In particular, the specific heats at constant volume given by

$$C_V = k_B\beta^2\left(\frac{\partial^2 \ln \mathcal{Z}}{\partial\beta^2}\right)_V \tag{1.53}$$

are found to be

$$C_V^{dn,sn} = Ak_B/[32\beta^{\frac{1}{4}}(B-\beta^{-\frac{1}{4}})^{\frac{3}{2}}]\left\{5+3/[2(B-\beta^{-\frac{1}{4}})\beta^{\frac{1}{4}}]\right\},$$

$$C_V^{cn} = 2Ek_B/\beta \quad (A<0),$$

$$C_V^{cn} = 2Gk_B/\beta \quad (A>0).$$

Therefore, the specific heats of the $dn(u,k)$ and the $sn(u,k)$ waves are of the same form. When these specific heats are graphed according to their allowed temperature range as in Fig. 1.23 to 1.25, we find that the specific heats for the $dn(u,k)$ and the $sn(u,k)$ waves are both negative. Therefore, we have confirmed through empirical analysis the instability of these two solutions. On the other hand, the specific heats of $cn(u,k)$ waves show a linear relation with temperature. Both specific heats are positive within the allowable range. Thus their stability is once more confirmed.

To summarize the results of this chapter, we have reviewed the exact analytic translationally-invariant solutions to the Landau-Ginzburg model in a uniaxial

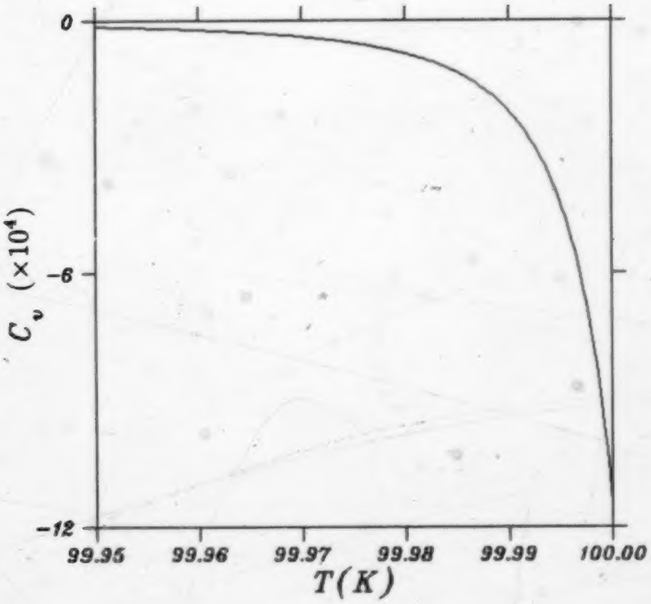

Figure 1.23: The specific heat capacity for the $dn(u,k)$ and the $sn(u,k)$ elliptic solutions.

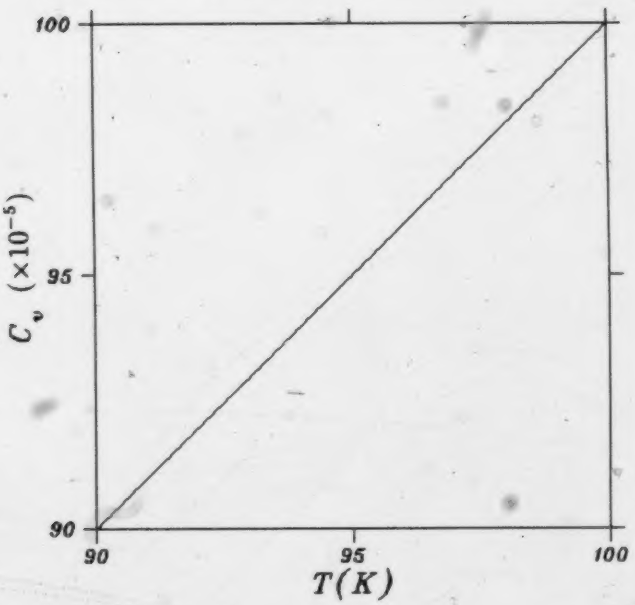

Figure 1.24: The specific heat capacity of the $cn(u,k)$ elliptic solutions in the case where $\epsilon < 0$.

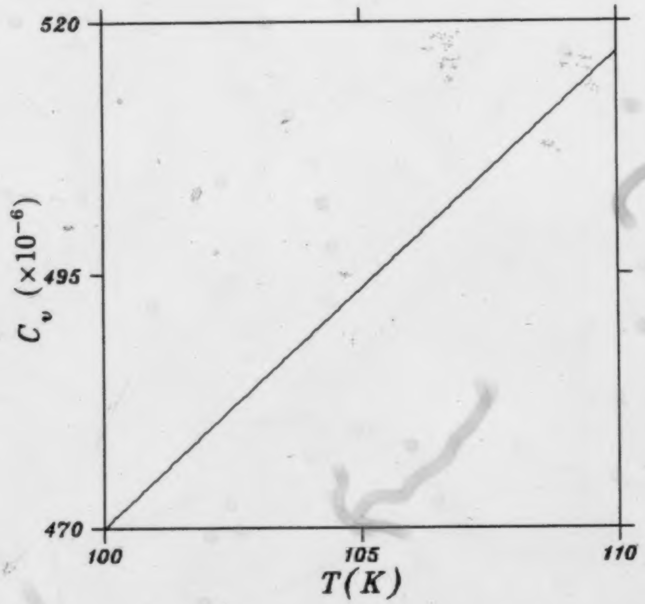

Figure 1.25: The specific heat capacity of the $cn(u,k)$ elliptic solutions in the case where $\epsilon > 0$.

ferromagnet. We have demonstrated that physically meaningful solutions such as magnetic double layers, domain wall spin waves, and nucleation of magnetic centers are direct results of the model. We have further shown that through empirical analysis some solutions are intrinsically unstable. Specifically, we have shown from our specific heat calculations that the $cn(u,k)$ elliptic solutions are stable while the $dn(u,k)$ and the $sn(u,k)$ elliptic solutions are unstable.

CHAPTER TWO

LANDAU-GINZBURG MODEL OF A UNIAXIAL FERROMAGNET IN THE PRESENCE OF A MAGNETIC FIELD

This chapter is an extension of the model used in Chapter One. Here, we include a weak magnetic field $\vec{H}$ pointing along the direction of easy magnetization, which is taken to be parallel to the z-axis. Then, the Landau-Ginzburg free energy expansion is exactly as given in (1.2) except that there is now an extra term on the right, the Zeeman term $-\vec{M}\cdot\vec{H} = -MH$ that describes the interaction between the magnetic field and the order-parameter M. Again, M denotes the z-component of the magnetization $\vec{M}$. The magnetic field $\vec{H}$ can either be positive or negative, depending on whether it is parallel or antiparallel to the axis of easy magnetization. With this Zeeman term, the free energy density expansion takes the form

$$f = f_0 + \frac{A}{2}M^2 + \frac{B}{4}M^4 + D|\vec{\nabla}M|^2 - MH. \tag{2.1}$$

The parameters f_0, A, B and D have exactly the same form as assumed in the previous chapter, that is, f_0 is temperature dependent, $A = \alpha(T - T_C)$ with $\alpha > 0$, $B > 0$ and D arbitrary [1]. Our intention in this chapter is to find out how the solutions we obtained earlier are modified by the presence of this weak magnetic field. The generalization of this model to include a weak magnetic field has been recently investigated by Winternitz et al. [12]. Although analytic solutions were obtained by the method of symmetry reduction, explicit behavior of the solutions as a function of the field was not presented. Therefore, we shall follow similar steps as in Chapter One but with the extra Zeeman term. We will first present briefly the derivation of the equation of motion for the order-parameter M and then by the method of symmetry reduction introduce some of the translationally-invariant solutions. We will then, using numerical analysis, look at how the weak magnetic field affects these solutions.

2.1 Equation of Motion

Making use of the Onsager relation (1.3), the equation of motion for the steady state is given by

$$\vec{\nabla}^2 M = \frac{1}{2D}\left(AM + BM^3 - H\right). \tag{2.2}$$

We only consider the translationally-invariant solutions, so we assume

$$\begin{aligned} M &= M(\xi) \qquad (2.3)\\ \xi &= z. \qquad (2.4)\end{aligned}$$

where z is just a representative independent variable for this type of reduction. These convert the equation of motion (2.2) to an ordinary differential equation of the form

$$\frac{d^2M}{d\xi^2} = \frac{1}{2D}\left(AM + BM^3 - H\right), \tag{2.5}$$

which can be integrated once to give

$$\begin{aligned}\left(\frac{dM}{d\xi}\right)^2 &= \frac{B}{4D}\left(M^4 + \frac{2A}{B}M^2 - \frac{4H}{B}M + \gamma\right) \qquad (2.6)\\ &= \Delta(M - M_1)(M - M_2)(M - M_3)(M - M_4) \qquad (2.7)\\ &= R(M) \qquad (2.8)\end{aligned}$$

where γ is the integration constant, $\Delta = B/4D$ and M_1, M_2, M_3 and M_4 are the roots of the fourth order polynomial on the right of (2.8). These roots are such that the following conditions are to be satisfied simultaneously:

$$M_1M_2M_3M_4 = \gamma \tag{2.9}$$

$$M_1M_2M_3 + M_1M_2M_4 + M_1M_3M_4 + M_2M_3M_4 = 4H/B \tag{2.10}$$

$$M_1M_2 + M_1M_3 + M_1M_4 + M_2M_3 + M_2M_4 + M_3M_4 = 2A/B \tag{2.11}$$

$$M_1 + M_2 + M_3 + M_4 = 0. \tag{2.12}$$

Depending on the values of these roots, solutions to the equation of motion (2.6) can be expressed in terms of various Jacobian elliptic functions [13]. Instead of going through the entire set of translationally-invariant solutions, we shall focus only on those that correspond to the ferromagnetic or the antiferromagnetic spin waves introduced in the last chapter.

2.2 The Ferromagnetic and The Antiferromagnetic Spin Waves

When $\triangle > 0$, $A < 0$ and the roots are real and distinct, the real and nonsingular solutions are expressed in terms of Jacobian elliptic functions [13]:

$$M(\xi) = \frac{\delta sn(\sqrt{\triangle K_0} R\xi, k) - \beta}{\alpha - \mu sn(\sqrt{\triangle K_0} R\xi, k)} \tag{2.13}$$

for $M_4 < M_3 \leq M \leq M_2 < M_1$, where $k = 1/R$ is the modulus of $sn(u,k)$ and $K_0 = [(M_1 - M_4)(M_2 - M_3)(R^2 - 1) - 2(M_1 - M_2)(M_3 - M_4)]/[2(R^2 - 1)]$. As shown in Fig. 2.1, the polynomial $R(M)$ is asymmetric in the presence of a weak magnetic field. The solutions are still periodic; however, they do not oscillate symmetrically about the vertical axis. Their periods are given by

$$T = \frac{4K(k)}{\sqrt{K_0 \triangle} R}. \tag{2.14}$$

The parameters δ, β, μ, α and R in (2.13) are written respectively as

$$\delta = M_1(M_2 - M_3)R + 2M_2M_3 - M_1(M_2 + M_3) \tag{2.15}$$

$$\beta = M_1(M_2 - M_3) + [2M_2M_3 - M_1(M_2 + M_3)]R \tag{2.16}$$

$$\mu = 2M_1 - M_2 - M_3 - (M_2 - M_3)R \tag{2.17}$$

$$\alpha = (2M_1 - M_2 - M_3)R - (M_2 - M_3) \tag{2.18}$$

$$\begin{aligned} R = {} & \{-2M_1M_4 - 2M_2M_3 + (M_1 + M_4)(M_2 + M_3) + \\ & 2[(M_1 - M_2)(M_1 - M_3)(M_2 - M_4)(M_3 - M_4)]^{\frac{1}{2}}\} \\ & [(M_1 - M_4)(M_2 - M_3)]^{-1}. \end{aligned} \tag{2.19}$$

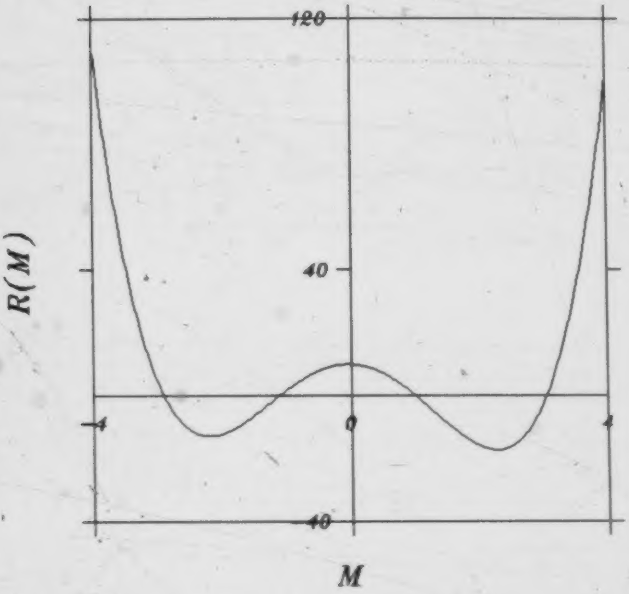

Figure 2.1: Plot of the polynomial $R(M)$ as a function of M.

In the zero field limit, $M_1 \longrightarrow -M_4$ and $M_2 \longrightarrow -M_3$. In that case, the above parameters are reduced respectively to $R = M_1/M_2$, $\mu = 0$, $\delta = 2(M_1^2 - M_2^2)$, $\beta = 0$ and $\alpha = 2(M_1^2 - M_2^2)/M_2$. The solutions (2.13) then approach the form

$$M \longrightarrow M_2 sn\left(\sqrt{\Delta} M_1 \xi, \frac{M_2}{M_1}\right). \tag{2.20}$$

Hence, we recover the antiferromagnetic spin waves obtained in Chapter One [11]. If the sign of Δ is reversed, real solutions exist only within two regions of M: $M_4 \leq M \leq M_3 < M_2 < M_1$ and $M_4 < M_3 < M_2 \leq M \leq M_1$. Their solutions are of the same form and are written in terms of the $dn(u, k)$ Jacobian elliptic functions [13]:

$$M = \frac{\epsilon\delta R dn(\sqrt{-\Delta K_0} R\xi, k) - \beta}{\alpha - \epsilon\mu R dn(\sqrt{-\Delta K_0} R\xi, k)} \tag{2.21}$$

where the modulus $k = \sqrt{1 - 1/R^2}$ and

$$\epsilon = \begin{cases} 1, & M_4 < M_3 < M_2 \le M \le M_1 \\ -1, & M_4 \le M \le M_3 < M_2 < M_1. \end{cases} \tag{2.22}$$

All other parameters are defined as before. The periods of these solutions are given by

$$T = \frac{2K(k)}{\sqrt{-\Delta K_0 R}}. \tag{2.23}$$

In the absence of magnetic field, the solutions again reduce to the ones that we obtained earlier [11].

$$M \longrightarrow \epsilon M_1 dn\left(\sqrt{-\Delta} M_1 \xi, k\right) \tag{2.24}$$

with $k = \sqrt{1 - M_2^2/M_1^2}$. Finally, if $\Delta < 0$ and if two distinct real roots (M_1 and M_2) and two complex conjugate roots (M_3 and M_4) exist so that $M_2 < M_1$ and $M_{3,4} = p \pm iq$ with $q > 0$, then the real solutions are given by

$$M = \frac{(M_2\sigma - M_1\phi)cn\left(\sqrt{-\Delta\sigma\phi}\xi, k\right) + M_2\sigma + M_1\phi}{(\sigma - \phi)cn\left(\sqrt{-\Delta\sigma\phi}\xi, k\right) + \sigma + \phi} \tag{2.25}$$

for $M_2 \le M \le M_1$, where $\sigma^2 = (M_1 - p)^2 + q^2$, $\phi^2 = (M_2 - p)^2 + q^2$, the modulus $k = \{[(M_1 - M_2)^2 - (\sigma - \phi)^2]/(4\sigma\phi)\}^{\frac{1}{2}}$ and its period

$$T = \frac{4K(k)}{\sqrt{-\Delta\sigma\phi}}. \tag{2.26}$$

In the absence of magnetic field, $M_2 \longrightarrow -M_1$ and $p \longrightarrow 0$. The solutions (2.25) then approach the form

$$M \longrightarrow -M_1 cn[\sqrt{-\Delta(M_1^2 + q^2)}\xi, k] \tag{2.27}$$

with the modulus $k = M_1/\sqrt{M_1^2 + q^2}$, which is in agreement with our earlier results [11].

Therefore, we have introduced the solutions corresponding to the ferromagnetic and the antiferromagnetic spin waves in the case of a weak magnetic field, and shown that these solutions behave appropriately in the zero field limit. However, the solutions, in their present forms, do not lend themselves easily for comparison. Their dependence on the magnetic field and the integration constant is implicit through their functional relations with the roots, hence it is not obvious at all how they evolve from their zero field limits. In order to examine how the magnetic field affects the dynamics of the above solutions, we need to introduce the mean magnetization. The purpose of this quantity is two-fold. First, it is an experimentially observable quantity, it allows us to make direct comparison with experimential results. Secondly, from intuition, since the magnet field points along the axis of easy magnetization we expect its magnitude to increase with that of the field. However, introducing this mean quantity, we defeat the purpose of the present model, namely, the inclusion of the Ginzburg term $|\vec{\nabla}M|^2$ to measure the magnetic inhomogeneity. In other words, we are over-looking the local property of the solutions by concerning ourselves only with their mean field property. Even though the mean magnetization represents a fair measure of the solutions' response to the external field, we will show later on that it does not always behave in accordance with our intuition. This unusual behavior can only be explained if we return to the local property of the solutions. In the next section, we shall derive analytic expressions for the mean magnetization in the above three special cases, their dependence on the magnetic field will then be examined by the method of numerical analysis.

2.3 Mean Magnetization

For our periodic solutions, the mean magnetization is defined as

$$\overline{M}(H,\gamma) = \frac{1}{T}\int_{\xi_0}^{\xi_0+T} M(\xi)d\xi \tag{2.28}$$

where T is the period of $M(\xi)$. We have indicated explicitly its dependence on the field H and on the integration constant γ.

a) The $sn(u,k)$ Solutions

If we substitute the solution (2.13) and its period (2.14) into the above integral, after a change of variable $u = \sqrt{\Delta K_0}R\xi$, the mean magnetization can be written as

$$\overline{M} = \frac{-\beta}{4\alpha K}\int_0^{4K} \frac{1-(\mu\delta/\alpha\beta)sn^2(u,k)}{1-(\mu^2/\alpha^2)sn^2(u,k)}du. \tag{2.29}$$

Then, if we make use of the symmetry property of the Jacobian elliptic function and the integral relation

$$\int_0^K \frac{1-a^2sn^2(u,k)}{1-b^2sn^2(u,k)}du = K\left(\frac{a^2}{b^2}\right) + \frac{b^2-a^2}{b^2}\Pi(b^2,k) \tag{2.30}$$

for $k^2 < b^2 < 1$, derived from the integral table provided by Byrd and Friedman [13], expression (2.29) is reduced to

$$\overline{M} = \frac{-\delta}{\mu} + \frac{\alpha\delta-\mu\beta}{\alpha\mu K}\Pi(\frac{\mu^2}{\alpha^2},k) \tag{2.31}$$

where $\Pi(\nu,k)$ is the complete elliptic integral of the third kind. This expression is valid for $k^2 < (\mu^2/\alpha^2) < 1$. In the absence of a magnetic field, the solution oscillates symmetrically about the horizontal axis. Therefore, we expect that its average over its period vanishes identically. The mean magnetization (2.31) is examined by numerical techniques, and its relation with the magnetic field is shown in Fig. 2.2. Because $\overline{M}$ depends on both H and γ, to isolate the effect due to the magnetic field only, we have kept γ fixed at a convenient value. But once γ is fixed, the solutions are valid only in a finite range of H: $0 \leq H \leq H_c$. Therefore, a critical field H_c is introduced beyond which the solutions cease to exist. In our case, γ is chosen such that the horizontial axis crosses the points of inflection of the polynomial (2.8) when

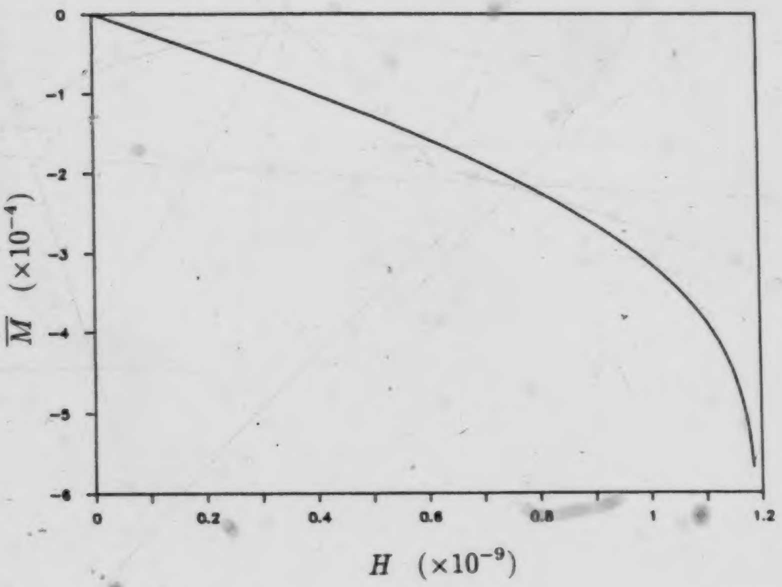

Figure 2.2: Field dependence of the mean magnetization for the $sn(u,k)$ solutions.

$H = 0$. Then, solving the equation $R(M) = 0$ and $dR/dM = 0$ simultaneously, we find that the critical field H_c is determined by

$$H_c = 2B\sqrt{\left(\sqrt{\frac{32}{27}} - 1\right)\left(\frac{|A|}{3B}\right)^3}. \tag{2.32}$$

Fig. 2.2 explores the entire range of H. As expected, the mean magnetization is zero in the absence of field. Its magnitude increases nonlinearly with H. This figure also indicates that, as the field approaches its critical value, the mean magnetization tends to saturate, however, in a direction opposite to the field. This implies that most of the time the magnetization $M(\xi)$ is antiparallel to the field over its spatial period. Such a configuration usually requires increasing the amount of energy as H rises, and hence, in accordance with our earlier result, the solution is intrinsically unstable.

b) The cn(u, k) Solutions

If the solution (2.25) and the period (2.26) are substituted into the integral (2.28), the mean magnetization can be expressed as

$$\overline{M} = \frac{a_3}{4a_4K}\int_0^{4K}\frac{1-[a_1a_2/(a_3a_4)]cn^2(u,k)}{1-a_2^2/a_4^2cn^2(u,k)}du \qquad (2.33)$$

following a change of variable $u = \sqrt{-\Delta\sigma\phi}\xi$. The parameters a_1, a_2, a_3 and a_4 are defined respectively as $a_1 = M_2\sigma - M_1\phi$, $a_2 = \sigma - \phi$, $a_3 = M_1\phi + M_2\sigma$ and $a_4 = \sigma + \phi$. Again, we make use of the symmetry property of the $cn(u,k)$ elliptic function, we divide the integral into four equal parts and convert the $cn(u,k)$ into the $sn(u,k)$ functions with the help of the identity $cn^2(u,k) + sn^2(u,k) = 1$. After rearrangement, the integral becomes

$$\overline{M} = \frac{a_3a_4 - a_1a_2}{K(a_4^2 - a_2^2)}\int_0^{K}\frac{1-a^2sn^2(u,k)}{1-b^2sn^2(u,k)}du \qquad (2.34)$$

where a^2 and b^2 are given respectively by $a^2 = a_1a_2/(a_1a_2 - a_3a_4)$ and $b^2 = a_2^2/(a_2^2 - a_4^2)$. This integral is again related to the complete elliptic integral of the third kind $\Pi(\nu, k)$ through the integral relation (2.30). Hence, the mean magnetization finally takes the form

$$\overline{M} = \frac{a_1}{a_2} + \frac{a_4(a_2a_3 - a_1a_4)}{Ka_2(a_4^2 - a_2^2)}\Pi(\frac{a_2^2}{a_2^2 - a_4^2}, k) \qquad (2.35)$$

for $k^2 < b^2 < 1$. Although this expression is very similar to (2.31), its dynamical behavior is radically more complicated. Numerical analysis shows that not only does it depend on the field and the integration constant, it also depends on the temperature. Its relation with the field changes from an inversely proportional to a proportional one as the temperature rises from below the critical temperature. Figures 2.3 to 2.6 show this sequence of transition as the scaled temperature ($\varepsilon = (T - T_c)/T_c$) increases from -0.75 to -0.01. At $\varepsilon = -0.75$, the mean magnetization behaves just as before, it grows in a direction opposite to H. But as ε climbs up to -0.55, the mean magnetization reaches its saturation value and begins to

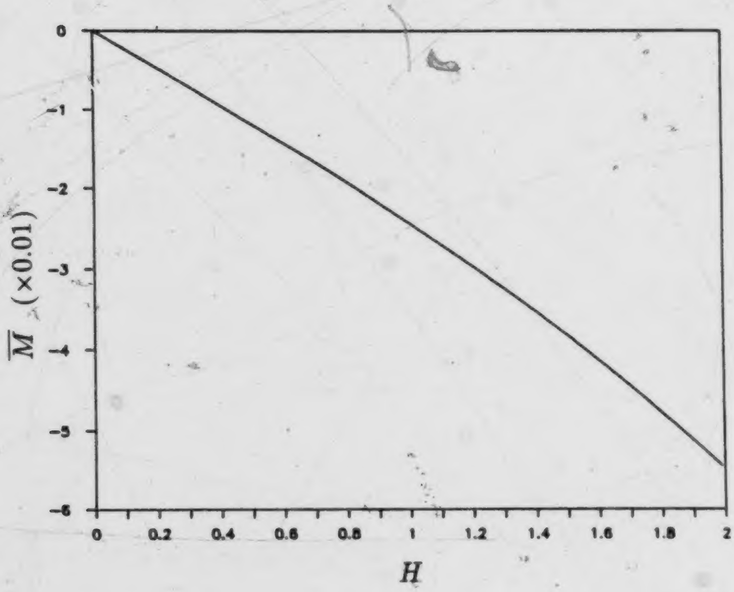

Figure 2.3: Mean magnetization for the $cn(u,k)$ waves at $\varepsilon = -0.75$.

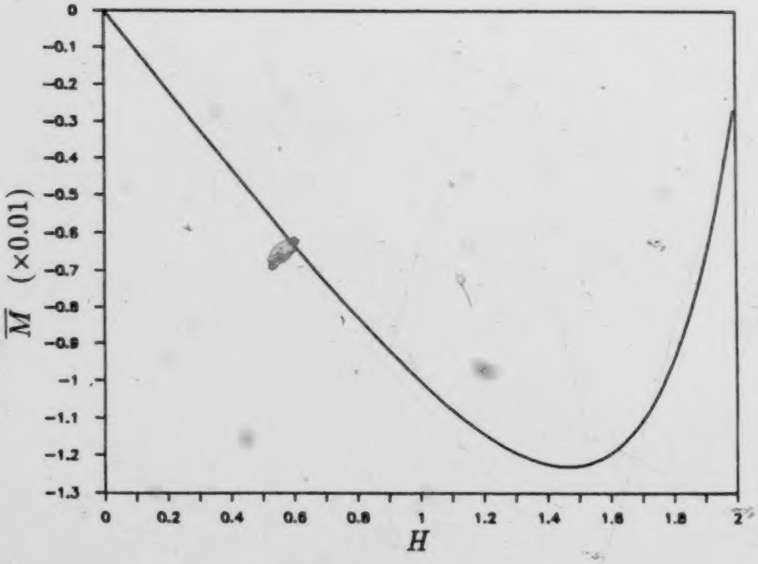

Figure 2.4: Mean magnetization for the $cn(u,k)$ waves at $\varepsilon = -0.55$.

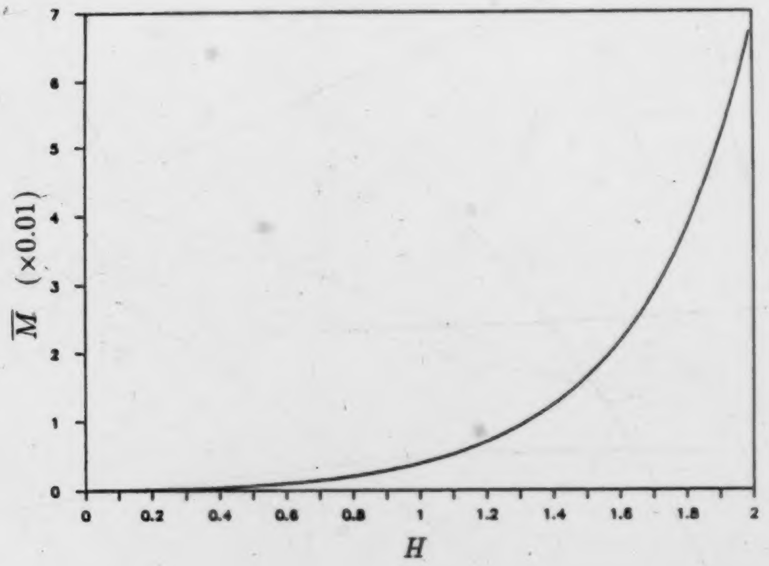

Figure 2.5: Mean magnetization for the $cn(u,k)$ waves at $\varepsilon = -0.45$.

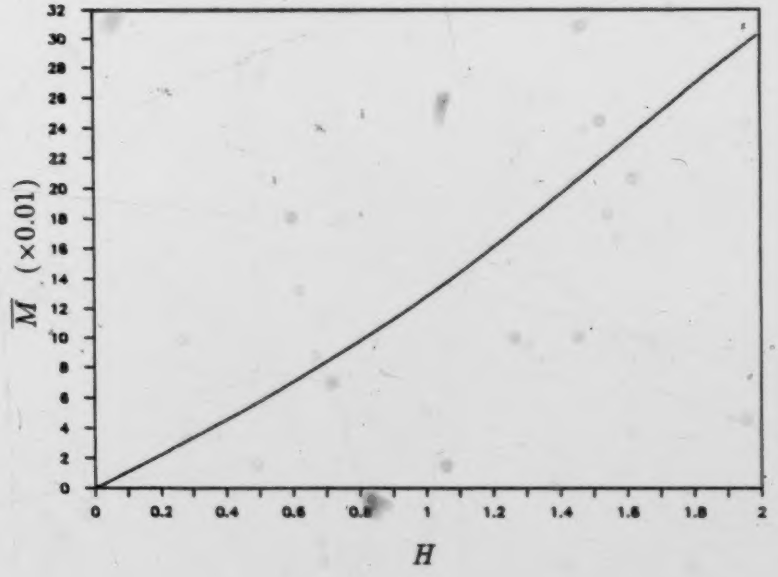

Figure 2.6: Mean magnetization for the $cn(u,k)$ waves at $\varepsilon = -0.01$.

reverse its direction; its magnitude diminishes with further increase in H. At higher temperatures, e.g. $\varepsilon = -0.45, -0.01$, the magnetization tends to align itself with the field, its mean value now rises in the direction of the field. One would naturally assume that this new configuration requires considerably less energy and is therefore energetically more favorable. We will show in the next section that this is simply not true. Mean magnetization in this case is no longer a good measure of the solutions' stability, rather, this mean field property totally obscures the picture. Contributions from the spatial variation of the solutions is so dominant that it is possible to have a stable configuration with its mean magnetization opposite to the field. Even though further investigation is necessary, the alignment of magnetization with the field could mean the existence of a new phase. According to Fig. 2.3 to 2.6, the boundary between these phases does not appear to be sharp and distinct. Therefore, a continuous phase transition is clearly evident.

c) The $dn(u,k)$ Solutions

Substituting the solution (2.21) and its period (2.23) into (2.28) and scaling the variable according to $u = \sqrt{-\Delta K_0} R\xi$, we can express the mean magnetization for the $dn(u,k)$ solutions as

$$\overline{M} = \frac{1}{K(k)} \int_0^K \frac{\epsilon\delta R dn(u,k) - \beta}{\alpha - \epsilon\mu R dn(u,k)} du. \tag{2.36}$$

We now use the Gauss' transformation [13]

$$dn(u,k) = \frac{1 - k_1 sn^2(u_1,k_1)}{1 + k_1 sn^2(u_1,k_1)} \tag{2.37}$$

where $u_1 = u/(1+k_1)$, $k_1 = (1-k')/(1+k')$ and k' is the complementary modulus of k, to convert the above integrand to

$$\omega \left\{ \frac{1 - \psi^2 sn^2(u_1,k_1)}{1 - \phi^2 sn^2(u_1,k_1)} \right\} \tag{2.38}$$

where ω, ψ^2 and ϕ^2 are defined respectively as $\omega = (\epsilon\delta R - \beta)/(\alpha - \epsilon\mu R)$, $\psi^2 = k_1(\epsilon\delta R + \beta)/(\epsilon\delta R - \beta)$ and $\phi^2 = k_1(\epsilon\mu R + \alpha)/(\epsilon\mu R - \alpha)$. Then the mean magnetization expressed as

$$\overline{M} = \frac{\omega(1+k_1)}{K(k)} \int_0^{\frac{K(k)}{1+k_1}} \frac{1 - \psi^2 sn^2(u_1, k_1)}{1 - \phi^2 sn^2(u_1, k_1)} du_1 \tag{2.39}$$

is related to the incomplete elliptic integral of the third kind $\Pi'(\tau, b^2)$ through the identity

$$\int_0^{\tau} \frac{1 - a^2 sn^2(u,k)}{1 - b^2 sn^2(u,k)} du = \frac{a^2}{b^2}\tau + \frac{b^2 - a^2}{b^2}\Pi'(\tau, b^2) \tag{2.40}$$

for $0 < k < b^2 < 1$, which is also derivable from the table of elliptic integrals provided by Byrd and Friedman [13]. Therefore, the mean magnetization takes the final form

$$\overline{M} = \frac{\omega(1+k_1)}{K(k)\phi^2}\left[\frac{\psi^2 K(k)}{1+k_1} + (\phi^2 - \psi^2)\Pi'(\frac{K(k)}{1+k_1}, \phi^2)\right] \tag{2.41}$$

for $0 < k_1 < \phi^2 < 1$. Note that there are two separate regions of M in which $dn(u,k)$ solutions exist: 1) for $M_4 < M_3 < M_2 \leq M \leq M_1$, $\epsilon = +1$; and 2) for $M_4 \leq M \leq M_3 < M_2 < M_1$, $\epsilon = -1$. In the absence of an external field, solutions in the first region oscillate symmetrically near the horizontial line $M = +1$ whereas those in the second region oscillate near $M = -1$. Therefore, their limiting mean values are finite, nonzero and are of opposite signs. In the presence of the magnetic field, the polynomial (2.8) is no longer symmetrical about the vertical axis. As a result, the waves' amplitudes begin to change and their mean values shift accordingly. For numerical convenience, we again chose γ such that the points of inflection of the polynomial (2.8) lie on the horizontal axis when $H = 0$, and we introduce the cutoff field H_c given exactly as in (2.32). Figures 2.7 and 2.8 summarize our numerical results. These graphs show that the mean values of the waves in both regions decrease with H, and suggest the magnetization is reluctant to align itself with the magnetic field. It would then appear that the process requires

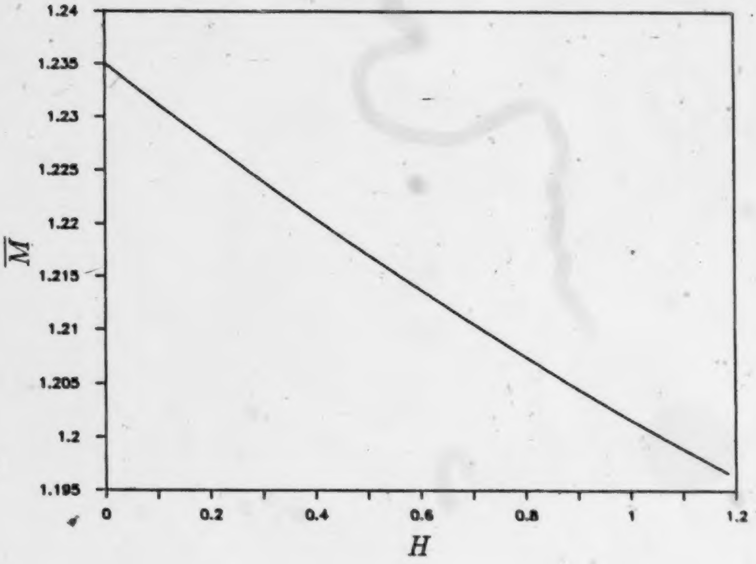

Figure 2.7: Mean magnetization of $dn(u,k)$ waves for $M_4 < M_3 < M_2 \leq M \leq M_1$.

a large amount of energy, which would indicate that these are unstable phases. We will again point out in the next section that this is not necessarily so.

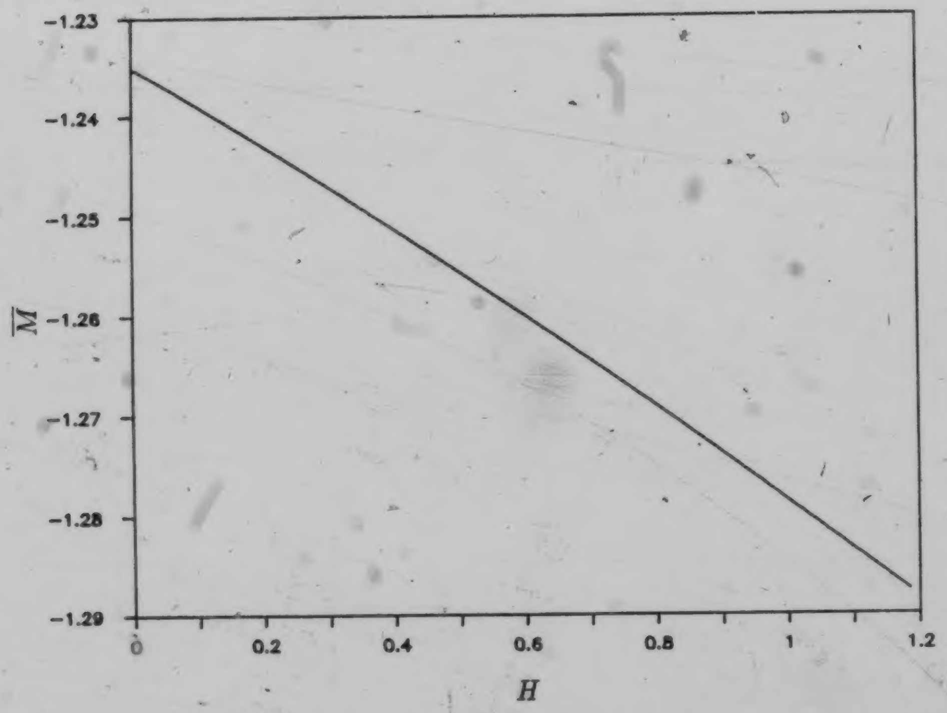

Figure 2.8: Mean magnetization of $dn(u,k)$ waves for $M_4 \leq M \leq M_3 < M_2 < M_1$.

2.4 Free Energy

For completeness, we include our numerical simulations of the free energy for the ferromagnetic and the antiferromagnetic spin waves in this section. The total free energy is obtained by integrating its density (2.1) over the entire volume of the sample:

$$F = \int \left\{ f_0 + \frac{A}{2}M^2 + \frac{B}{4}M^4 + D|\vec{\nabla}M|^2 - MH \right\} d^3r \tag{2.42}$$

For our translationally-invariant solutions, we substitute (2.3) and (2.4) into the above expression and rewrite it as

$$\frac{F}{S_\perp} = \int_0^l \left\{ f_0 + \frac{A}{2}M^2 + \frac{B}{4}M^4 + D\left(\frac{dM}{d\xi}\right)^2 - MH \right\} d\xi \tag{2.43}$$

where we have taken $S_\perp$ and l to be the cross-sectional area and the length of the sample, respectively. The gradient term in the above integrand can be replaced immediately by the expression (2.6). Then, the total free energy is obtained by direct numerical integration. Since the solutions are periodic, the length of the sample can be taken conveniently as the period of the solution. Our results are presented in Fig 2.9-2.15. In agreement with our intuition, Fig.2.9 and 2.15 show that the $sn(u,k)$ and the $dn(u,k)$ (for $M_4 \leq M \leq M_3 < M_2 < M_1$) elliptic solutions are indeed unstable. In both cases, an increasing amount of energy is required to turn the magnetization against the magnetic field. The rest of the figures however implies a very unusual behavior, namely, the free energy of the system is lowered by misalignment of magnetization with the field. If we examine the free energy expression (2.43) carefully, we find that this phenomenon can be understood as a result of a competition between the local inhomogeneous and the mean field properties of the solutions. For those solutions whose spatial periods are long, their gradients are small. Then, their free energies are dominated by their mean field property. Therefore, having the magnetization antiparallel to the field increases

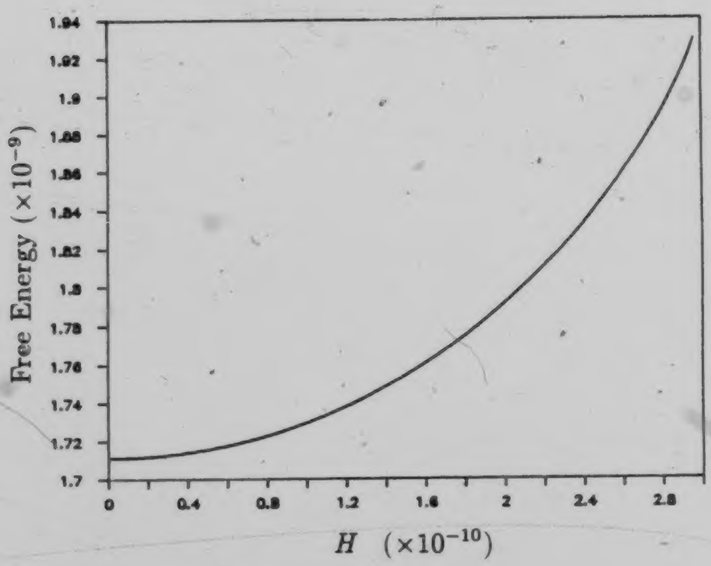

Figure 2.9: Field dependence of the free energy for the $sn(u,k)$ solutions.

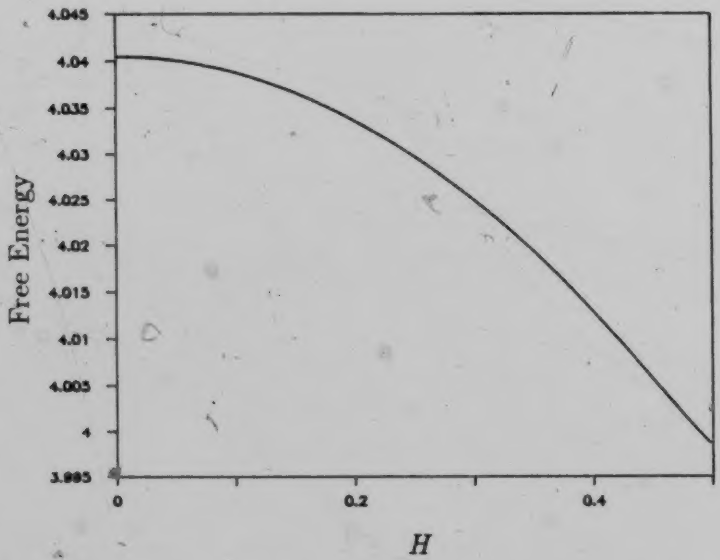

Figure 2.10: Free energy of the $cn(u,k)$ solutions at $\varepsilon = -0.6$.

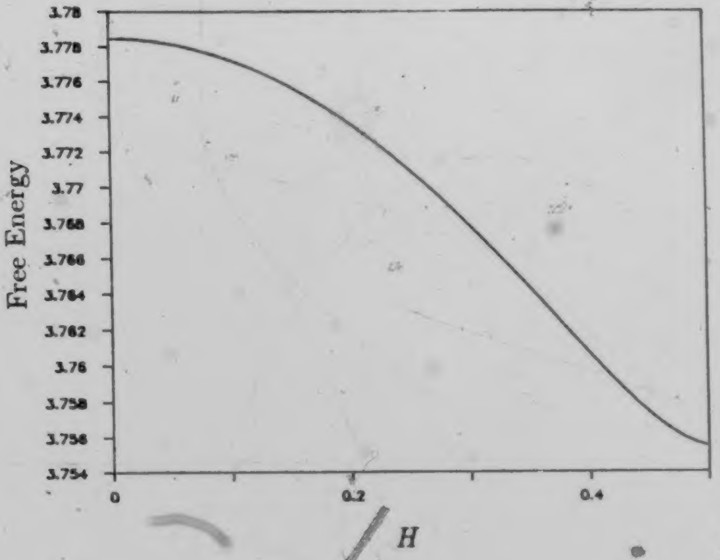

Figure 2.11: Free energy of the $cn(u,k)$ solutions at $\varepsilon = -0.55$.

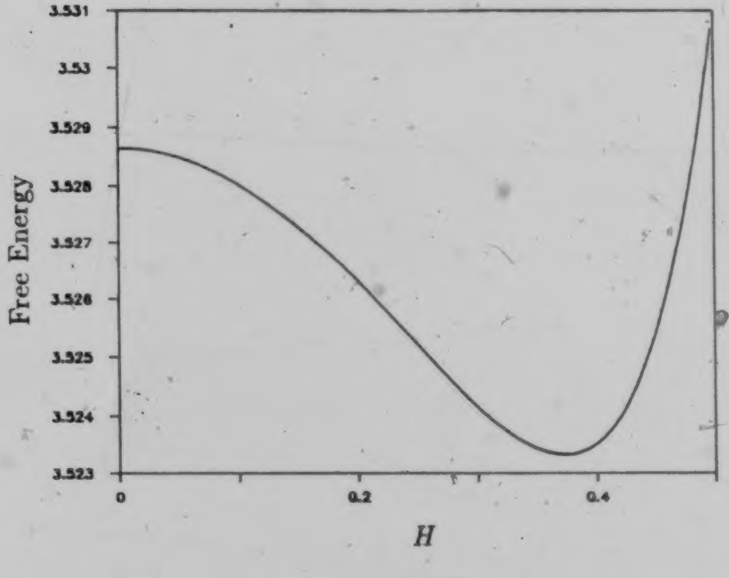

Figure 2.12: Free energy of the $cn(u,k)$ solutions at $\varepsilon = -0.5$.

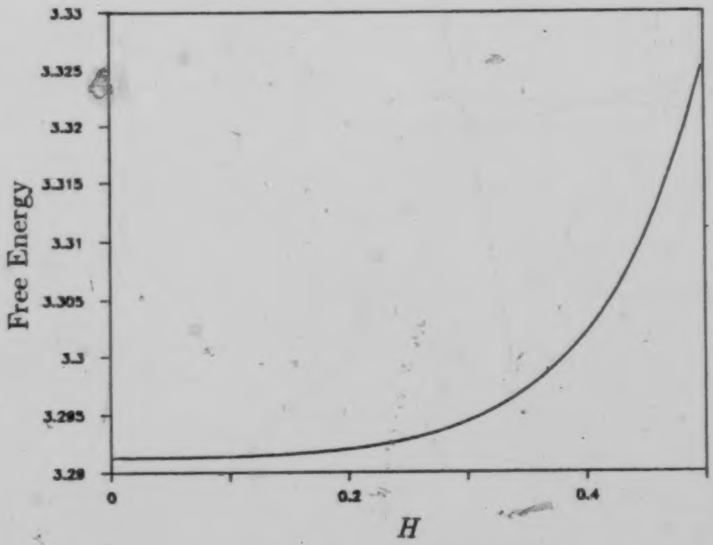

Figure 2.13: Free energy of the $cn(u, k)$ solutions st $\varepsilon = -0.45$.

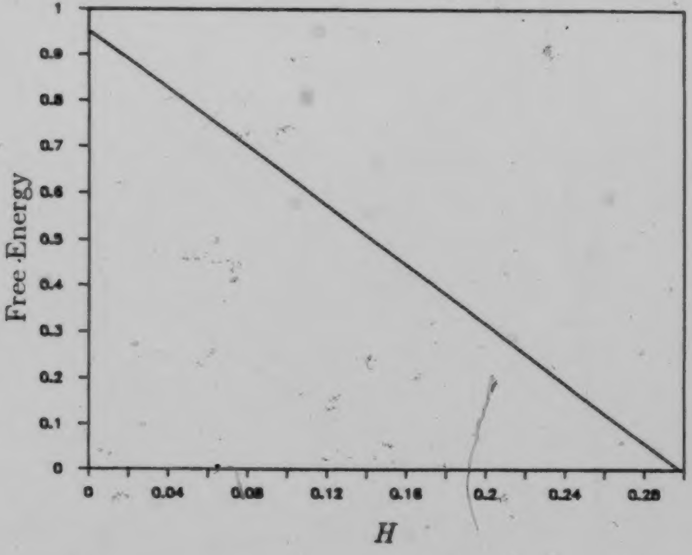

Figure 2.14: Free energy of the $dn(u, k)$ waves in region 1.

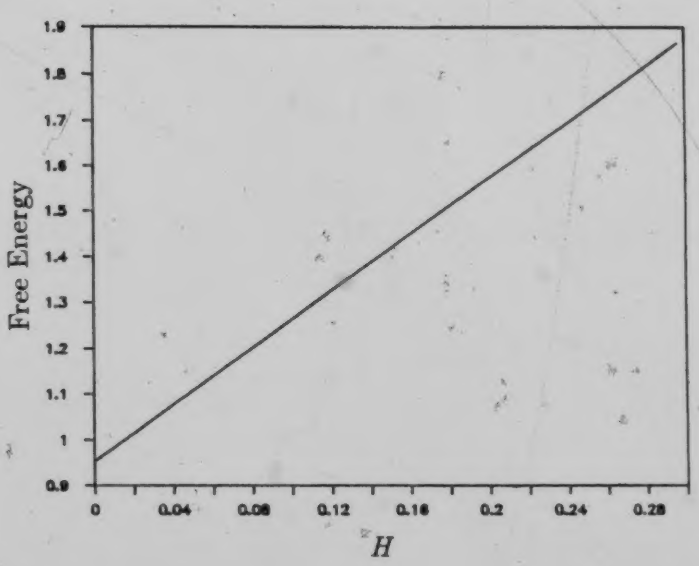

Figure 2.15: Free energy of the $dn(u,k)$ waves in region 2.

the total free energy. This could be the case for the above $sn(u,k)$ and $dn(u,k)$ elliptic waves. On the other hand, if the spatial period is short, then the gradient in (2.43) takes over and makes most of its contribution to the free energy. The mean field property in this case is irrelevant. The free energy can increase or decrease regardless of whether the magnetization is parallel or antiparallel to the field. This explains the unusual field dependence of the free energy for the $cn(u,k)$ and the $dn(u,k)$ (for $M_4 < M_3 < M_2 \le M \le M_1$) elliptic waves.

To summarize the results of this chapter, we have shown that the presence of a weak magnetic field breaks the symmetry of the polynomial that appears in the equation of motion. This symmetry breaking causes the elliptic wave solutions $sn(u,k)$ and $cn(u,k)$ to oscillate asymmetrically about the horizontal axis and the $dn(u,k)$ solutions about the saturation values $M = \pm 1$. We have further calculated the mean magnetizations for these waves and deduced that, through numerical analysis, not only are these magnetizations reluctant to align themselves with the field, but they tend to be antiparallel to the field as the field strength increases. These waves are interpreted as inhomogeneous phases. Furthermore, the $cn(u,k)$ solutions exhibit continuous phase transitions in which the magnetization reverses its direction to be parallel to the field as the field passes a certain threshold value. This could suggest that stable phases exist at a sufficiently high field. Our evidence is however inconclusive because our model assumes only a weak magnetic field so that the signs and values of the parameters A, B, D and γ are not affected by it. This process deserves further investigation. Finally, through our numerical simulations of the free energy, we have shown that stable solutions exist only in the case of the $cn(u,k)$ elliptic waves and that there are signs of competition between the local inhomogeneous and the mean field properties of the solutions. For those solutions whose spatial periods are long, their free energies are determined by their mean field property; whereas, for those whose spatial periods are short, their free energies are determined by their local property, specifically, their spatial variations. In the latter case, the mean magnetization becomes irrelevant in deciding the stability of the solutions.

CHAPTER THREE

BIFURCATIONS AND PERTURBATIVE ANALYSIS IN THE X^2Y^2 POTENTIAL PROBLEM

Ergodicity of the system given by the Hamiltonian

$$H = \frac{1}{2}(p_x^2 + p_y^2 + x^2y^2) \tag{3.1}$$

has been a controversy for a long time. This system has been suggested to be associated with a simplified model of the classical Yang-Mills field which is related to the vacuum fluctuations in quantum chromodynamics [14]. The system is also found to be applicable to the plasma confinement problem in which a particular magnetic-vector potential generates the unbounded x^2y^2- potential. Extensive studies on the dynamics of the system were carried out by many groups over the years [14]-[23], no evidence of stable motion had ever been reported. Following the detailed numerical investigation using the surfaces of section by Carnegie and Percival [19], many authors believed that the system was globally ergodic. Only recently, Dahlqvist and Russberg [9] have demonstrated the existence of a family of stable periodic orbits and a regular region in a Poincaré section. They have also pointed out that because the regular region occupies a very small fraction of the accessible phase space it is very difficult to detect. In view of the important nature of this system, in this chapter we will examine its dynamical behavior by applying perturbations to two unstable, analytic straight-line trajectories.

There is no natural limit on the spatial extent of the motion of a particle moving in this x^2y^2 potential. The potential's three-dimensional and contour plots are shown in Fig. 3.1 and Fig. 3.2. A particle can propagate along any of the axes to infinity. These motions correspond to the trival solutions to the problem and are

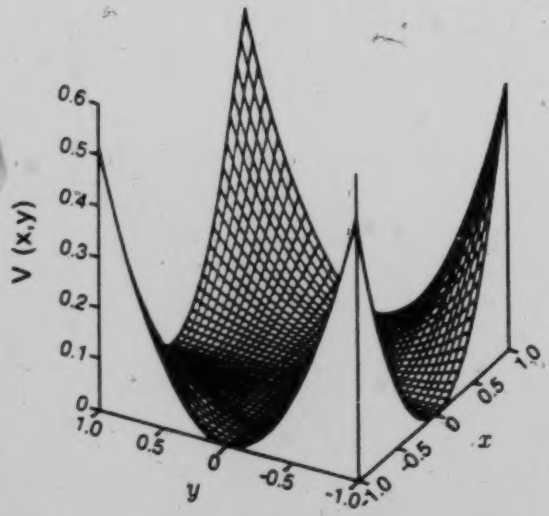

Figure 3.1: Three-dimensional plot of the x^2y^2-potential.

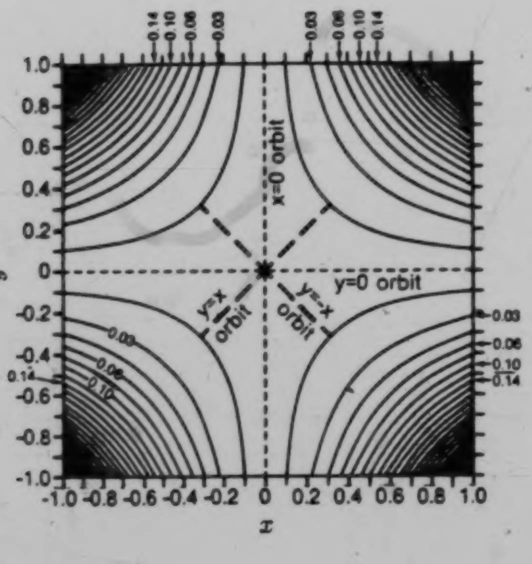

Figure 3.2: Contour plot of the potential.

represented by the trajectories

$$x = 0, \quad \frac{dy}{dt} = \pm\sqrt{2E} \tag{3.2}$$

and

$$y = 0, \quad \frac{dx}{dt} = \pm\sqrt{2E}. \tag{3.3}$$

These trajectories are made up of points placed at the positions of local potential minima. Hence, they are the most stable paths that the system is able to sustain. Particles travelling along these paths experience no net force at all; they simply move along at a constant velocity of magnitude $\sqrt{2E}$. Whether any physical conditions exist that determine if a particle's motion remains bounded is an important question, because, as mentioned above, it is closely related to the plasma confinement problem where charged particles are trapped by the very same potential that arises from the magnetic-vector potential. We shall illustrate this derivation in section 3.3. It is also our aim in this chapter to develop some analytic tools to shed light on this question.

3.1 Numerical Simulations

The equations of motion corresponding to the Hamiltonian (3.1) are

$$\frac{d^2x}{dt^2} = -xy^2 \tag{3.4}$$

and

$$\frac{d^2y}{dt^2} = -yx^2 \tag{3.5}$$

With the total energy of the system held fixed at 1/2 (for numerical convenience but without loss of generality) for all initial conditions, the equations are integrated using the fourth-order Runge-Kutta method with a step size 0.005. A member of the family of stable periodic orbits mentioned earlier is found and shown in Fig 3.3.

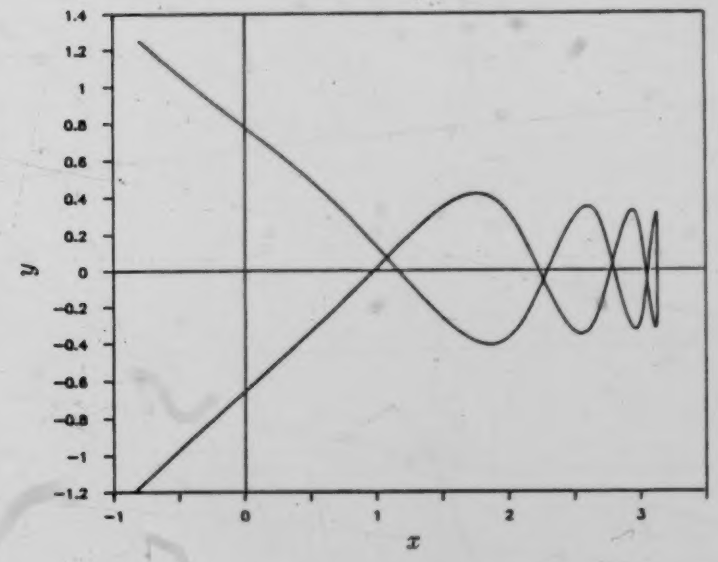

Figure 3.3: A stable periodic trajectory.

In addition, as shown in Fig. 3.4, we discover two straight-interval trajectories:

$$y = \pm x \tag{3.6}$$

which are unstable with respect to the initial condition. These are regular (non-chaotic) trajectories. Fig. 3.5 and Fig. 3.6 show that, for the $y = x$ interval, x and y are both periodic functions of time and that their periods are commensurate (the ratio of their periods is 1:1 indeed). As shown in Fig. 3.7 and Fig. 3.8, the velocities $\dot{x}$ and $\dot{y}$ are also found to have the same properties. Consequently, each of these trajectories appears as a single point in a Poincaré section such as, for example, $\dot{x}$ *vs* x ($y = 0$, $\dot{y} > 0$).

Analytical expressions for these two unstable trajectories are readily obtainable. If we assume equation (3.6) for the trajectory, then the equations of motion are reduced to

$$\frac{d^2x}{dt^2} = -x^3 \tag{3.7}$$

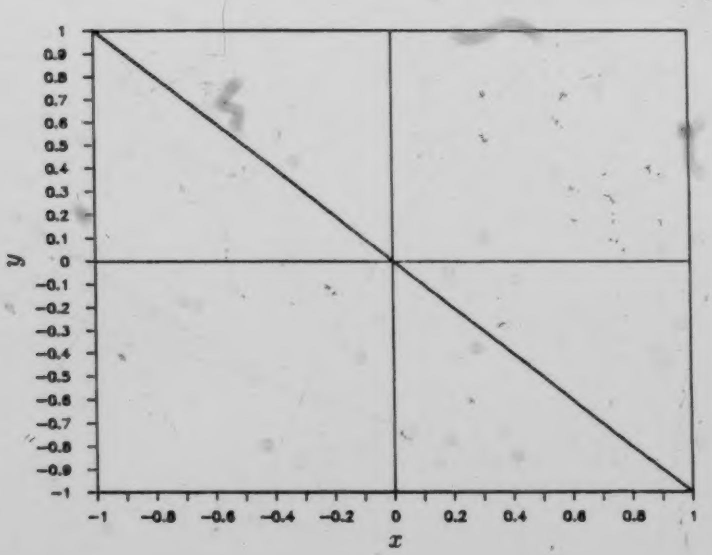

Figure 3.4: The straight-interval trajectory $y = -x$.

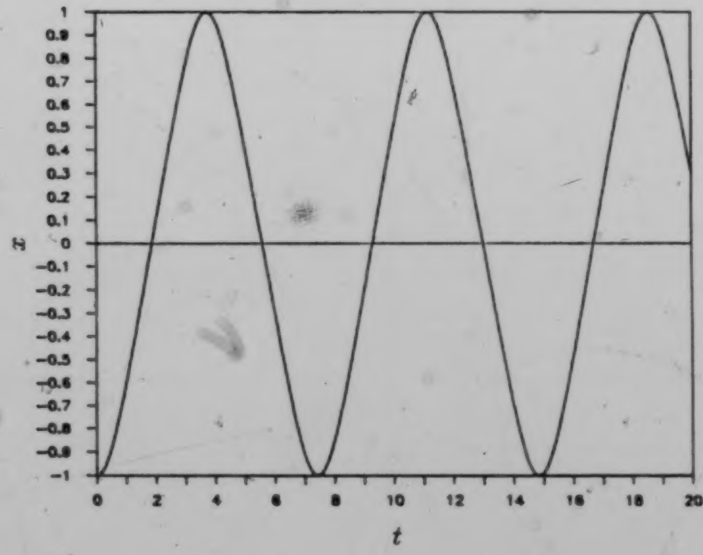

Figure 3.5: x as a periodic function of t for the straight-line path.

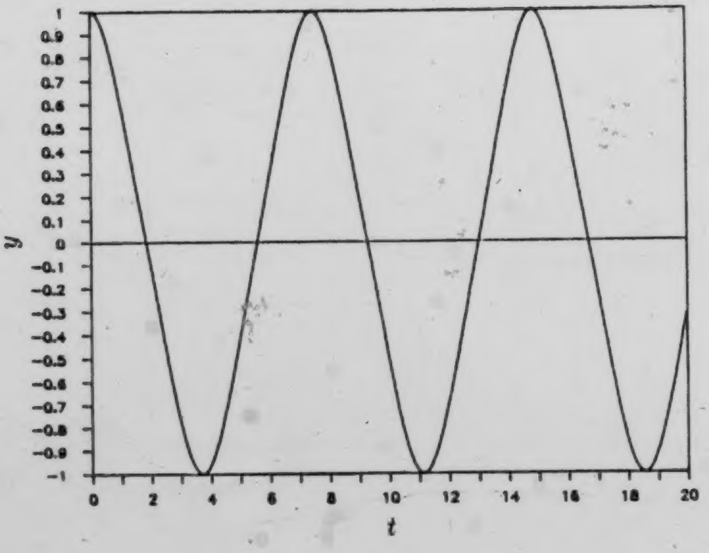

Figure 3.6: y as a periodic function of t for the straight-line path.

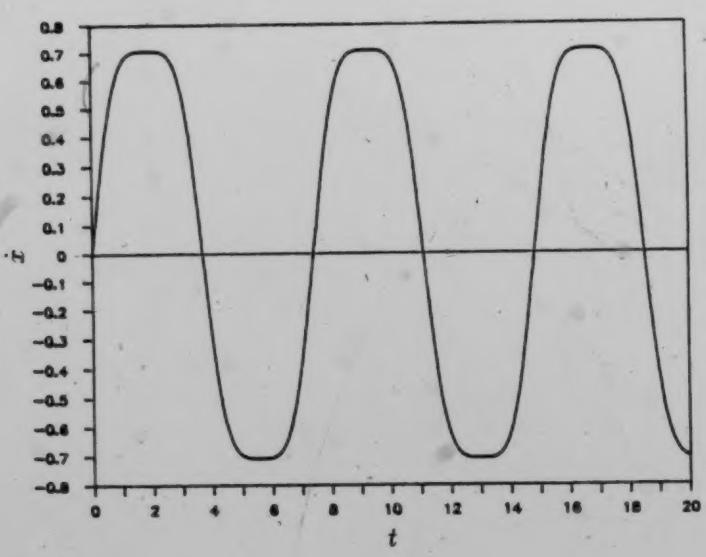

Figure 3.7: $\dot{x}$ as a periodic function of t for the straight-line path.

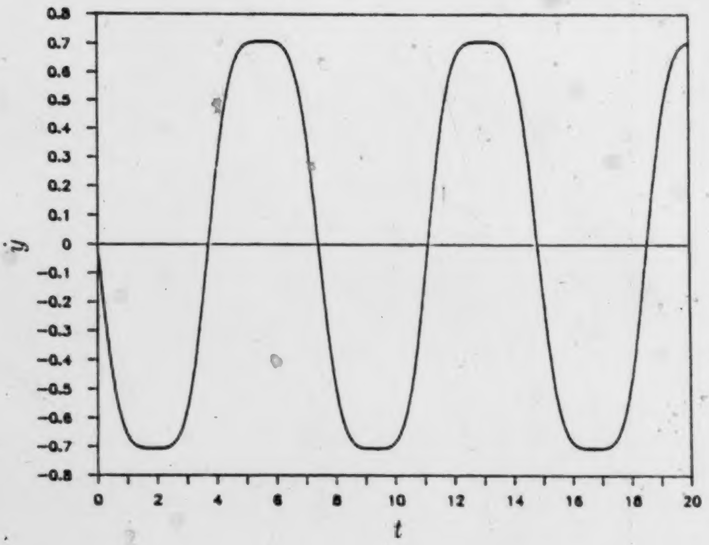

Figure 3.8: $\dot{y}$ as a periodic function of t for the straight-line path.

for both cases. Integrating this equation once, we obtain

$$\left(\frac{dx}{dt}\right)^2 = -\frac{x^4}{2} + c \tag{3.8}$$

where c is an integration constant. From the energy conservation $E = 1/2\,(\dot{x}^2 + \dot{y}^2 + x^2 y^2)$, for $y = \pm x$, $\dot{x} = E$ when $x = 0$. This implies $c = E$. Then, the corresponding solution to equation (3.8) is given by

$$x(t) = (2E)^{\frac{1}{4}} cn((2E)^{\frac{1}{4}} t, 1/\sqrt{2}) \tag{3.9}$$

where $cn(u, k)$ is the Jacobian elliptic cosine function and k is the modulus [13]. The function is doubly periodic. It has a real period as well as an imaginary one. In this case only the real period is relevant and is given by

$$T = \frac{4K(1/\sqrt{2})}{(2E)^{\frac{1}{4}}} \tag{3.10}$$

where $K(k)$ is the complete elliptic integral of the first kind [13]. The amplitude of the wave therefore increases, while its period decreases with energy. At energy 1/2,

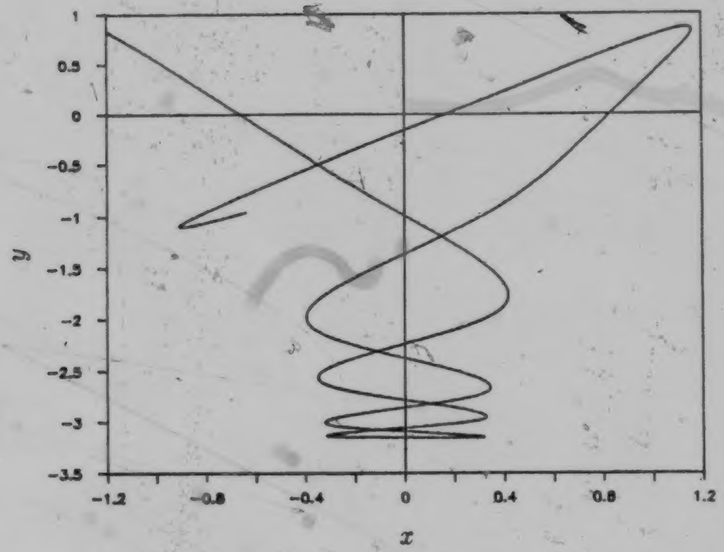

Figure 3.9: Trajectory for $x_0 = -1.2$.

$T = 7.4163$. This value seems to agree quite well with our numerical result (Fig. 3.5).

Changing the initial condition by a small amount leads the system into completely chaotic states. For convenience, we keep the initial kinetic energy always zero. When the initial x is increased by a small amount, instead of following the straight-line path $y = x$, the particle departs from it, oscillates around the y-axis and bounces between the lower potential walls. This motion is depicted in Fig. 3.9. It oscillates around the x-axis and bounces between the potential walls on the right as shown in Fig. 3.10, if the initial x is decreased instead. The unstable straight-line intervals can be thought of as consisting of points of unstable equilibrium where the local potential energy is at the saddle point. Infinitesimal deviations from these straight lines cause the particle to travel in the direction of the potential's steepest descent, in an attempt to achieve stable equilibrium. This explains the trajectories' sensitive dependence on initial conditions.

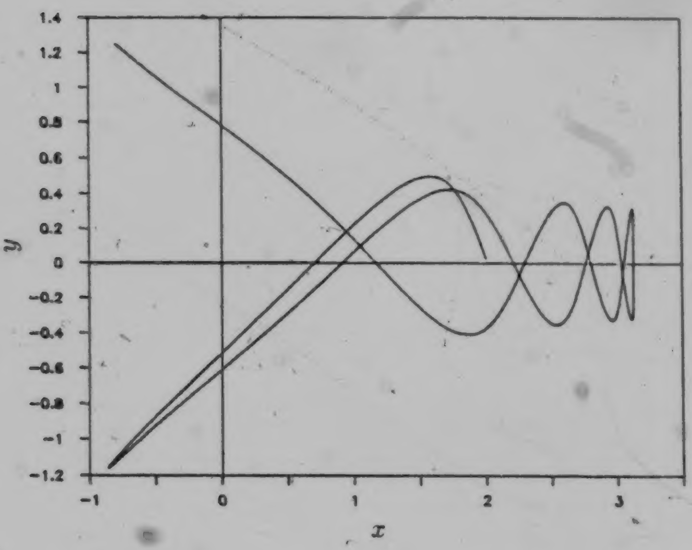

Figure 3.10: Trajectory for $x_0 = -0.8$.

Plotting the positions and the velocities of these two neighboring paths as functions of time as in Fig. 3.11-3.18 once again reveals that they are all periodic in time; however, their periods are incommensurate. In a Poincaré section, these trajectories appear as points scattered randomly throughout the entire accessible region and eventually become space-filling if the particle's motion remains bounded. Although these two chaotic trajectories extend in two different directions, there is a symmetry relation between them. From Fig. 3.11 to Fig. 3.18, their motions are related by a mirror reflection about the straight line $y = x$, or more explicitly through the transformation

$$x_2 = -y_1 \tag{3.11}$$

$$y_2 = -x_1 \tag{3.12}$$

These graphs further show that a secondary period emerges as the particle departs from the straight line path. Therefore, bifurcation is clearly evident. Although we have assumed zero initial kinetic energies in the above computations, we have

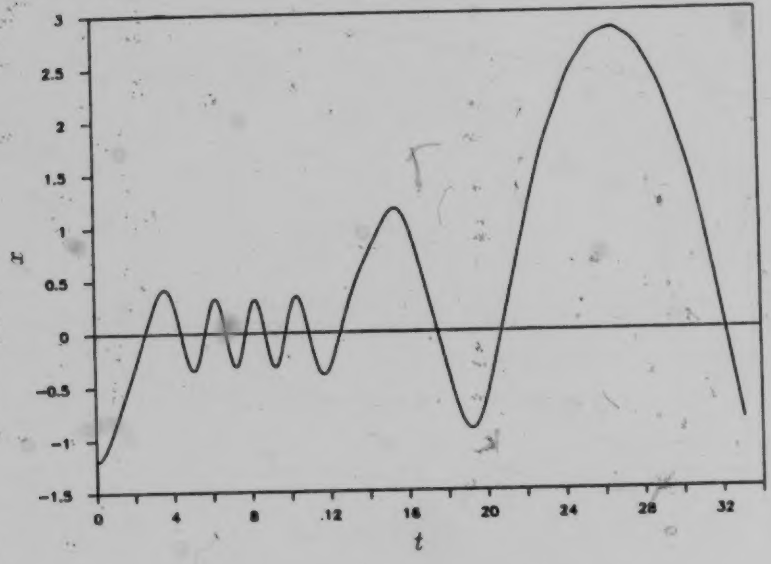

Figure 3.11: x *vs* t for $x_0 = -1.2$.

rechecked and confirmed that the system's behavior is not changed if non-zero values are used.

3.2 Perturbative Analysis I

The above observations lead us to speculate that an infinitesimal departure from the unstable straight-line paths (3.6) causes the system to follow one of several stable orbits. To test our theory, we look for solutions to the equations of motion of the form:

$$\begin{aligned} X(t) &= x(t) + u(t) \\ Y(t) &= y(t) + v(t) \end{aligned} \tag{3.13}$$

where $x(t)$ and $y(t)$ represent the straight-line paths, $u(t)$ and $v(t)$ the infinitesimal perturbations. Substituting (3.13) into the equations of motion (3.4) and (3.5), and

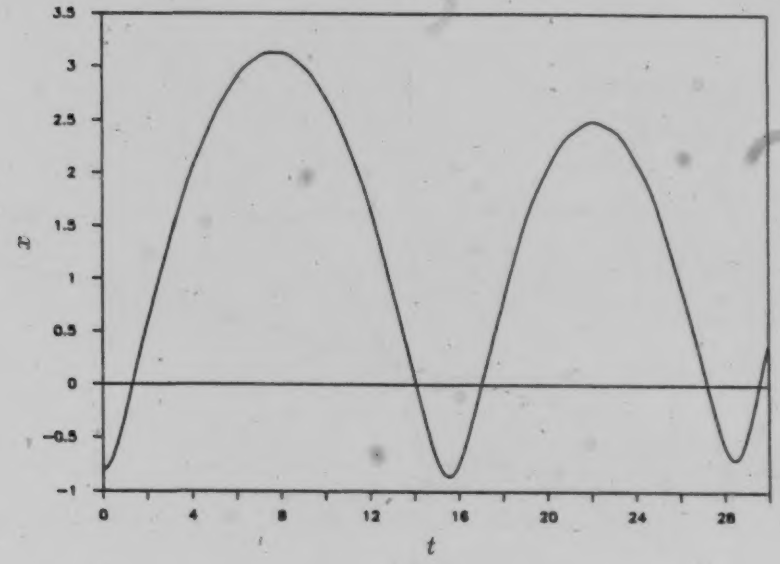

Figure 3.12: x *vs* t for $x_0 = -0.8$.

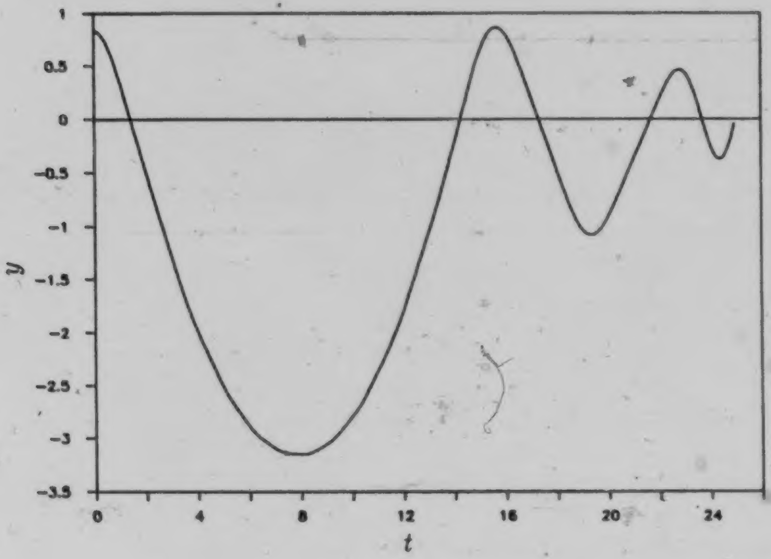

Figure 3.13: y *vs* t for $x_0 = -1.2$.

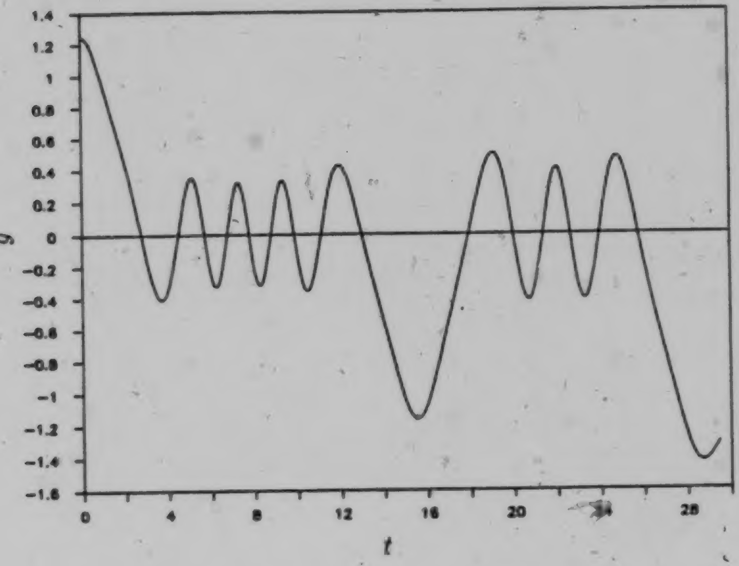

Figure 3.14: y *vs* t for $x_0 = -0.8$

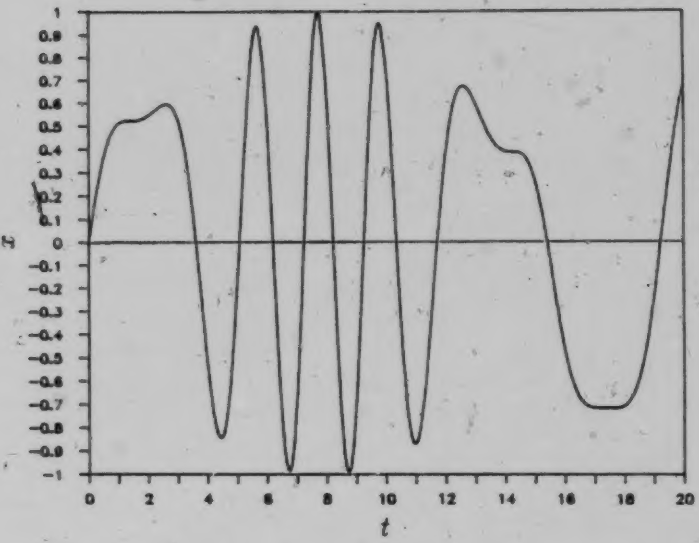

Figure 3.15: $\dot{x}$ *vs* t for $x_0 = -1.2$.

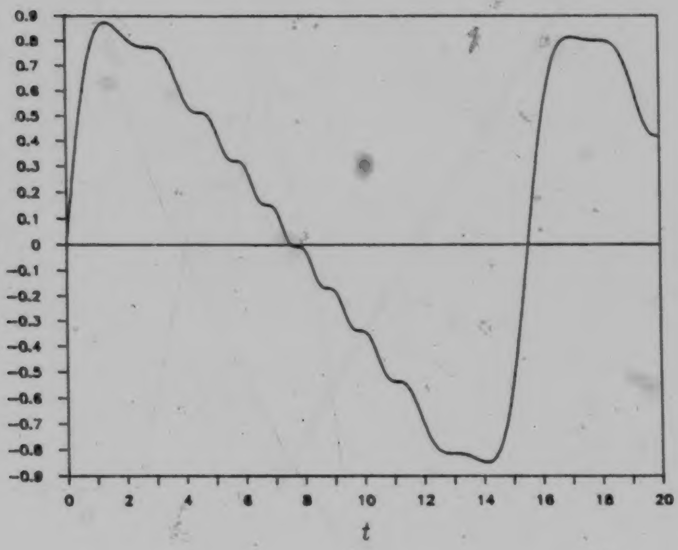

Figure 3.16: $\dot{x}$ *vs* t for $x_0 = -0.8$.

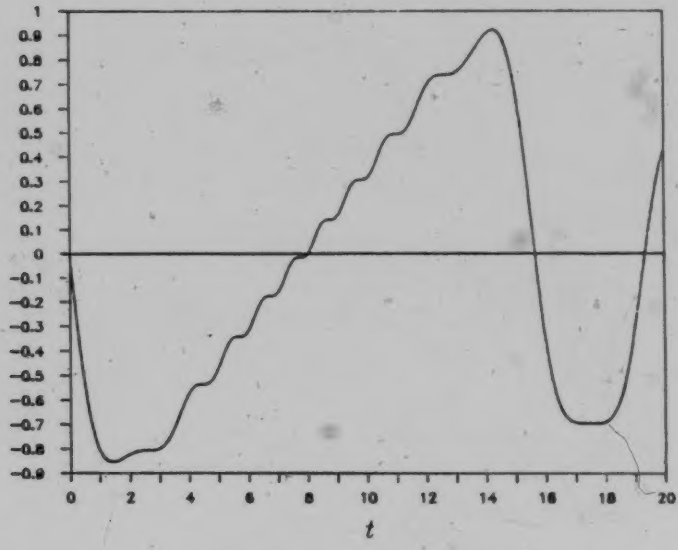

Figure 3.17: $\dot{y}$ *vs* t for $x_0 = -1.2$.

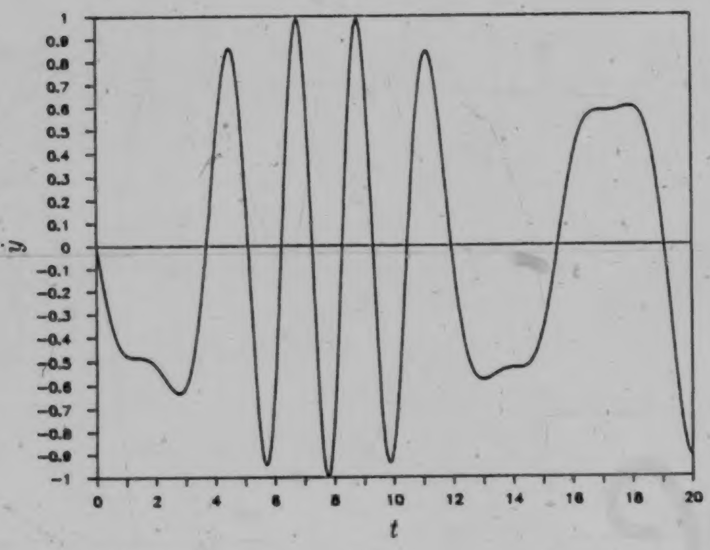

Figure 3.18: $\dot{y}$ *vs* t for $x_0 = -0.8$.

ignoring high order perturbations, we obtain the equations:

$$\begin{aligned} \frac{d^2u}{dt^2} &= -x^2(\pm 2v + u) \\ \frac{d^2v}{dt^2} &= -y^2(\pm 2u + v) \end{aligned} \tag{3.14}$$

where the "+" corresponds to the case $y = x$ and the "−" the case $y = -x$. In matrix notation, these equations are written as

$$\frac{d^2}{dt^2}\begin{bmatrix} u \\ v \end{bmatrix} = -x^2 \begin{bmatrix} 1 & \pm 2 \\ \pm 2 & 1 \end{bmatrix}\begin{bmatrix} u \\ v \end{bmatrix}. \tag{3.15}$$

Because a small change in the initial conditions eventually leads the system to a completely different trajectory, our perturbative approach is valid only for a very short initial time-interval while the particle's trajectory still remains in the proximity of the straight-line path. These matrix equations can be diagonalized by a similarity transformation. Note that, for the case $y = x$, the eigenvalues of the 2×2

matrix on the right are $\lambda_1 = 3$ and $\lambda_2 = -1$, and the corresponding normalized eigenvectors are

$$\begin{bmatrix} \frac{1}{\sqrt{2}} \\ \frac{1}{\sqrt{2}} \end{bmatrix} \text{ and } \begin{bmatrix} \frac{1}{\sqrt{2}} \\ \frac{-1}{\sqrt{2}} \end{bmatrix} \tag{3.16}$$

respectively. For the case $y = -x$, its eigenvalues are $\lambda_1 = 3$, $\lambda_2 = -1$ and the corresponding eigenvectors are

$$\begin{bmatrix} \frac{-1}{\sqrt{2}} \\ \frac{1}{\sqrt{2}} \end{bmatrix} \text{ and } \begin{bmatrix} \frac{1}{\sqrt{2}} \\ \frac{1}{\sqrt{2}} \end{bmatrix} \tag{3.17}$$

respectively. Then equation (3.15) can be diagonalized as follows

$$\frac{d^2}{dt^2}\left\{C^T\begin{pmatrix} u \\ v \end{pmatrix}\right\} = -x^2 C^T \begin{pmatrix} 1 & \pm 2 \\ \pm 2 & 1 \end{pmatrix} C C^T \begin{pmatrix} u \\ v \end{pmatrix} \tag{3.18}$$

where, for the case $y = x$,

$$C = \frac{1}{\sqrt{2}}\begin{bmatrix} 1 & 1 \\ 1 & -1 \end{bmatrix},$$

and, for the case $y = -x$,

$$C = \frac{1}{\sqrt{2}}\begin{bmatrix} -1 & 1 \\ 1 & 1 \end{bmatrix}.$$

The matrix C^T denotes the transpose of C. With a change of basis, equations for the case $y = x$ are diagonalized and decoupled as

$$\frac{d^2\phi_1}{dt^2} = -3x^2\phi_1 \tag{3.19}$$

$$\frac{d^2\phi_2}{dt^2} = x^2\phi_2. \tag{3.20}$$

We have introduced the transformed variables $\phi_1 = (u+v)/\sqrt{2}$ and $\phi_2 = (u-v)/\sqrt{2}$. The set of equations for the case $y = -x$ can be obtained simply by interchanging ϕ_1 and ϕ_2 in the above equations (3.19) and (3.20); the corresponding solutions can be obtained in the same way. Therefore, equations (3.19) and (3.20) have captured the dynamical symmetry of the perturbations. Substituting the Jacobian elliptic solution (3.9) into these equations, and using the identity $sn^2(u,k) + cn^2(u,k) = 1$, they become

$$\frac{d^2\phi_1}{d\tau^2} = 3\left[sn^2(\tau, \frac{1}{\sqrt{2}}) - 1\right]\phi_1, \tag{3.21}$$

and

$$\frac{d^2\phi_2}{d\tau^2} = -\left[sn^2(\tau, \frac{1}{\sqrt{2}}) - 1\right]\phi_2. \tag{3.22}$$

We have scaled the independent time variable as $\tau = (2E)^{\frac{1}{4}}t$. Equation (3.21) is a special case of the Jacobian form of the Lamé equation [24]

$$\frac{d^2\psi}{dz^2} = \left[n(n+1)k^2 sn^2(z,k) + A\right]\psi \tag{3.23}$$

where n is any positive integer and A is an arbitrary constant. Equation (3.21) then corresponds to the case $n = 2$ and $A = -3$. Its analytic solution [24] is given by

$$\phi_1(\tau) = \prod_{r=1}^{2} \frac{H(\tau + \tau_r)}{\Theta(\tau)} exp(-\tau Z(\tau_r)). \tag{3.24}$$

The parameters τ_1 and τ_2 must be chosen so that the following conditions are satisfied simultaneously:

$$\sum_{p=1}^{2}{}' \frac{sn(\tau_p)cn(\tau_p)dn(\tau_p) + sn(\tau_r)cn(\tau_r)dn(\tau_r)}{sn^2(\tau_p) - sn^2(\tau_r)} = 0 \tag{3.25}$$

and

$$\left\{\sum_{r=1}^{2} cn(\tau_r)ds(\tau_r)\right\}^2 - \sum_{r=1}^{2} ns^2(\tau_r) = A \tag{3.26}$$

where $r = 1, 2$ and the prime indicates that terms with $p = r$ are to be excluded from the sum. In addition, the sum of the left hand sides of conditions (3.25) must also vanish identically. Therefore, conditions (3.25) and (3.26) represent two altogether independent equations. In the expression (3.24), Jacobi's Zeta, Jacobi's Theta and first order Theta functions have been denoted by $Z(\nu)$, $\Theta(\nu)$ and $H(\nu)$, respectively. The solution is a product of two factors of periodic functions. It can therefore be doubly periodic. A periodic solution is indeed what we expected. Since the equation (3.21) can be looked upon as an equation of motion of a particle moving in a periodic attractive potential, its solutions naturally represent the periodic bound states. What is not obvious from the equation is the double periodicity of the solution. It implies oscillation within a periodic envelope. This indirectly gives a theoretical confirmation of the bifurcation effects observed earlier in our numerical simulations. Unfortunately, equation (3.22) does not correspond to any specific case of Lamé equation and cannot be solved straight-forwardly either. But, since the equation describes the motion of a particle moving in a periodic repulsive potential, its solutions must reflect the non-periodic scattering states. If we now transform back to our old basis, our original perturbations are given in terms of ϕ_1 and ϕ_2:

$$\begin{aligned} u(t) &= (\phi_1 + \phi_2)/\sqrt{2} \\ v(t) &= (\phi_1 - \phi_2)/\sqrt{2}. \end{aligned} \tag{3.27}$$

It becomes clear now that bifurcations come from only the periodic bound states of equation (3.21).

3.3 Perturbative Analysis II

A differential equation that describes the actual motion of the particle can be derived if we regard y as a function of x, i.e. $y = f(x(t))$. The first and the second derivatives of y with respect to time then yield

$$\frac{dy}{dt} = \frac{df}{dx}\frac{dx}{dt} \tag{3.28}$$

and

$$\frac{d^2y}{dt^2} = \frac{df}{dx}\frac{d^2x}{dt^2} + \left(\frac{dx}{dt}\right)^2 \frac{d^2f}{dx^2}. \tag{3.29}$$

Substituting the equations of motion (3.4) and (3.5) into (3.29), it becomes

$$-f(x)x^2 = -\frac{df}{dx}xf^2(x) + \left(\frac{dx}{dt}\right)^2 \frac{d^2f}{dx^2}. \tag{3.30}$$

If we now put equations (3.28) and (3.30) in the conservation of energy expression $E = 1/2(\dot{x}^2 + \dot{y}^2 + x^2y^2)$, we obtain a second order differential equation that governs the particle's trajectories:

$$\frac{d^2f}{dx^2}(2E - x^2f^2) = xf\left[1 + \left(\frac{df}{dx}\right)^2\right]\left[f\frac{df}{dx} - x\right]. \tag{3.31}$$

An analytical solution to this equation may not be easily obtainable for a general case. However, useful information regarding the dynamical behavior of the system can still be extracted by performing a similar perturbative analysis to (3.31).

Since the dynamics of the unstable straight-interval trajectories (3.6) has already been well understood and we have indeed written their solutions in analytic form, it seems logical that we perturb the trajectory once again with respect to this straight-line path. Therefore, for a very short initial time interval, we look for solutions to (3.31) of the form

$$y = f(x) = \pm x + \eta(x) \tag{3.32}$$

where x represents the unperturbed straight-line paths and η the infinitesimal perturbation. Substituting (3.32) into equation (3.31) and ignoring all high order perturbations leads to a special case of Pfaff's equation:

$$\frac{d^2\eta}{dx^2}(2E - x^4) - 2x^3\frac{d\eta}{dx} - 2x^2\eta = 0. \tag{3.33}$$

According to the table of equations of second order provided by Murphy [25], this equation is not integrable in finite terms. But if we scale the independent variable according to $x = (2E)^{\frac{1}{4}} z$ and take $\zeta = z^4$, equation (3.33) is transformed to Gauss's hypergeometric equation[25]

$$\zeta(1-\zeta)\frac{d^2\eta}{d\zeta^2} + \frac{d\eta}{d\zeta}\left\{\frac{3}{4} - (1+\frac{1}{4})\zeta\right\} - \frac{1}{8}\eta = 0 \tag{3.34}$$

which has two independent solutions

$$_2F_1\left(\frac{1 \mp i\sqrt{7}}{8}, \frac{1 \pm i\sqrt{7}}{8}, \frac{3}{4}; \zeta\right) \tag{3.35}$$

and

$$\zeta^{\frac{1}{4}}\,{}_2F_1\left(\frac{3 \mp i\sqrt{7}}{8}, \frac{3 \pm i\sqrt{7}}{8}, \frac{5}{4}; \zeta\right). \tag{3.36}$$

The hypergeometric function $_2F_1(a, b, c; \zeta)$ is defined conventionally as

$$_2F_1(a, b, c; \zeta) = 1 + \frac{ab}{c}\zeta + \frac{a(a+1)\,b(b+1)}{2!\,c(c+1)}\zeta^2 + \cdots. \tag{3.37}$$

The general solution to equation (3.34) is then a linear combination of (3.35) and (3.36), which allows $\eta(x)$ a wide range of dynamical behavior.

If oscillations take place around the x-axis with very small amplitudes and long periods, we can determine accurately where the trajectories cross the axis with the help of equation (3.31). If $f(x)$ and its gradient df/dx are both very small, equation (3.31) is reduced to

$$\frac{d^2 f}{dx^2} = \frac{-x^2}{2E} f. \tag{3.38}$$

If we take $f(x) = \sqrt{x}y(x)$ and $x = \sqrt{2}x^2/(4\sqrt{E})$, the equation is transformed to

$$z^2\frac{d^2y}{dz^2} + z\frac{dy}{dz} + (z^2 - \frac{1}{4^2})y = 0. \tag{3.39}$$

This is a differential equation for the Bessel functions of order 1/4 [25]. The general solution to this equation is a linear combination of two independent Bessel functions:

$$y(z) = C_1 J_{\frac{1}{4}}(z) + C_2 J_{-\frac{1}{4}}(z) \tag{3.40}$$

where C_1 and C_2 are arbitrary constants to be determined by the initial conditions. However, $J_{-\frac{1}{4}}(z)$ becomes divergent at the origin; hence, a physically meaningful solution to equation (3.38) consists of only the first term of (3.40)

$$f(x) = C_1\sqrt{x}J_{\frac{1}{4}}\left(\sqrt{\frac{2}{E}}\frac{x^2}{4}\right), \tag{3.41}$$

for $x \geq 0$. The solution exhibits damped oscillations around the x-axis. At very low energies, where the motion is restrictive and the amplitudes of oscillations are small, the above solution can be applied appropriately. Then, the intersections of the trajectories with the x-axis correspond directly to the zeros of the Bessel function in (3.41), and these zeros are the fixed points (common points) of all trajectories stretching along the x-axis.

We mentioned earlier that our system is closely related to the plasma confinement problem. The Hamiltonian for such a system is given by

$$H = \frac{1}{2m}\left\{p_x^2 + p_y^2 + \left(p_z - \frac{eA_z}{c}\right)^2\right\} \tag{3.42}$$

where $\vec{A} = A_z\vec{k}$ with $A_z = xy$ is the magnetic vector potential derived from the magnetic induction $\vec{B} = x\vec{i} - y\vec{j}$. The momenta p_i are the canonical momenta defined as

$$p_i = m\dot{x}_i + \frac{eA_i}{c}. \tag{3.43}$$

Since z is a cyclic coordinate, the z-component of the canonical momentum is a constant of motion. If we demand that p_z is to vanish identically, then the particle's velocity along the z-direction is given explicitly as

$$\dot{z} = \frac{-e}{mc}xy. \tag{3.44}$$

A x^2y^2-potential then appears in the above Hamiltonian. Although this Hamiltonian resembles the one given in (3.1), the particle in this case moves in a three-dimensional space. For this reason, its energy conservation is slightly modified.

Since H does not depend on time explicitly, it represents the total energy of the system. With a vanishing p_z, the total energy is written as

$$E = \frac{1}{2m}(p_x^2 + p_y^2 + \frac{e^2}{c^2}x^2y^2). \tag{3.45}$$

This energy expression neither corresponds to nor is reducible by the method of scaling to the energy conservation in the two-dimensional case. To such a system, it would be invaluable to determine what initial conditions give rise to bounded trajectories. These relations may not be easy to derive. But, for our two-dimensional model, armed with equation (3.31) and assuming bounded trajectories, we can at least model the particle's behavior near its farthermost points (turning points hereafter) of its trajectories. We do not know what determines the locations of these points, but we do know at these points the gradients (assuming trajectories along the x-direction) dy/dx approach an infinite value and the velocities $\dot{x}$ and $\dot{y}$ become infinitesimally small. Using these facts in equation (3.31), we get a second order differential equation that describes the particle's approximate behavior near its turning point (x_t, y_t):

$$\frac{d^2y}{dx^2} = \left(\frac{x_t y_t^2}{2E - x_t^2 y_t^2}\right)\left(\frac{dy}{dx}\right)^3 \tag{3.46}$$

This equation can be integrated at once to give

$$x = -(\frac{x_t y_t^2}{4E - 2x_t^2 y_t^2}y^2 + B_1 y + B_2) \tag{3.47}$$

where B_1 and B_2 are the integration constants. The constant B_1 is determined by the condition that the gradient becomes infinite at (x_t, y_t), and B_2 by $y(x_t) = y_t$.

Therefore, we have provided physical reasons for the unstable straight-interval trajectories in the x^2y^2-potential problem and shown that they are expressible in terms of Jacobian elliptic functions. Using perturbative methods on the equations of motion, we have proven that the solutions can be doubly periodic and thus provided theoretical basis for the observed bifurcations. Furthermore, applying perturbative techniques again on the equation that describes the particle's trajectories, we have obtained an approximate expression for the particle's trajectories at extremely low energies and for those in the neighborhood of the particle's farthermost points at any energy. The question whether a natural bound on the motion of the particle exists still remains. Nevertheless, we have shown, while exact methods are not feasible, perturbative techniques can be used to extract interesting information.

CHAPTER FOUR

CHAOS IN TWO-DIMENSIONAL LATTICES

Lattice dynamics has long been considered to be intimately related to the mechanisms of structural phase transitions. Numerous studies have been done on the dynamics of lattices with the inclusion of the first and the next nearest neighbor interactions [26]-[30]. These interactions often give rise to the nonlinear behavior of these systems. In some cases, the lattice is placed in a spatially periodic external substrate potential (the Frenkel- Kontorova model). Such a model is able to explain the dynamics of crystal growth [31]-[34] and of adsorbed atomic layers [35]-[39]. Nonlinear modes of behavior such as solitons are often found to play an important role in lattice dynamics. However, most studies are limited to short range interactions and to one dimension only. In addition, although the motion of solitons in a crystal lattice is related to the deterministic behavior of the system, the lattice may also be capable of exhibiting stochastic or chaotic behavior due to instability. Therefore, it will be interesting to identify what physical conditions determine whether the nonlinear lattice behaves chaotically.

To achieve these objectives, we consider a two-dimensional monatomic lattice with an approximation applied to the long-range interactions. The approximation is somewhat similar to the molecular field approach, where we consider each atom in a self-consistent field due to the atoms beyond its first nearest neighbors. These long range interactions will appear as anharmonic terms in the effective potential.

This anharmonic lattice offers a very good way of revealing the structural phase transition as well as the classical transition of order into chaos. Generally speaking, in this continuum approximation, chaotic behavior arises from a system of coupled nonlinear partial differential equations that describes the classical dynamical system [40]. Chaos, in this context, means that even though a solution to the equations exists, the state of the system in phase space is indeterministic, contrary to the old Newtonian physics in which, once the solution is found, the state of the system is known at all times. In this chapter, we shall demonstrate such chaotic behavior through a simplified two-dimensional lattice model. We will first derive the equations of motion for the system, and then obtain its effective Hamiltonian. The solution will be obtained by means of numerical analysis, and its dynamical behavior displayed through sequential Poincaré sections.

4.1 The Model

We consider a monatomic two-dimensional rectangular lattice in which the atoms are coupled to their nearest neighbors in the x- and the y-directions by springs of different elasticities so that anisotropy is built into the model. This atomic layer is depicted in Fig. 4.1. In addition, the spacings between the equilibrium positions of the atoms can be unequal in different directions. This rectangular symmetry is of great use in reducing the complexity of various analytic expressions to be derived later on. Also, to avoid any boundary effects, we also assume the lattice to be infinitely large.

The total potential energy of the system can be approximated by separating it into the sum of the mean field potential U^{MF} due to higher order coordination spheres and the potential due to the nearest-neighbor interactions U^{nn}:

$$U^{tot} = U^{MF} + U^{nn}. \tag{4.1}$$

The mean field potential comes from the mutual interactions among the atoms themselves but excludes the interactions between the first nearest-neighbors. Its purpose is two fold: i) it approximates the long-range interactions that exist within

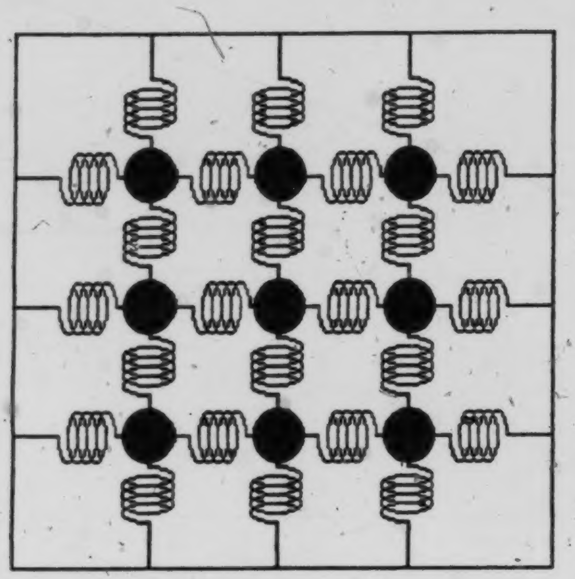

Figure 4.1: A two-dimensional crystal lattice.

the lattice and ii) if this potential is regarded as external, our system can be used to describe the dynamics of adsorbed layers in which, very much like the Frenkel-Kontorova model, our mean field potential can be looked upon as the potential due to the substrate. The potentials in (4.1) can be expanded in powers of the components of the atomic displacements. Once their analytic forms are found, the equations of motion are readily obtainable by differentiation.

4.2 The Mean Field Potential

In the mean field approach, we look at one atom at a time and calculate the interaction potential of the atom with the rest of the population (except the nearest neighbors) when they are at their equilibrium positions. Then, the sum of these interaction potentials over all lattice sites gives rise to the mean field potential U^{MF}.

If $\vec{s}$ is the lattice vector and $\vec{u}(\vec{s})$ the displacement of the atom at site $\vec{s}$, then the interaction potential is given by

$$U_{\vec{s}}(\vec{u}(\vec{s})) = {\sum_{\vec{m}}}' V(\vec{s}+\vec{u}(\vec{s})-\vec{m}) \tag{4.2}$$

where $V(\vec{r})$ represents the two-body restoring force potential and is a function of the separation only. The prime in the summation on the right indicates that terms involving the nearest neighbors are to be excluded. Denoting the cartesian components of $\vec{u}(\vec{s})$ by $u_\alpha(\vec{s}), \alpha = 1, 2, 3$, we expand the interaction potential $U_{\vec{s}}(\vec{u}(\vec{s}))$ in powers of the components of $\vec{u}(\vec{s})$

$$\begin{aligned} U_{\vec{s}}(\vec{u}(\vec{s})) &= {\sum_{\vec{m}}}' V(\vec{s}-\vec{m}) + {\sum_{\vec{m}}}' \frac{\partial}{\partial s_\alpha} V(\vec{s}-\vec{m}) u_\alpha(\vec{s}) \\ &\quad + \frac{1}{2!} {\sum_{\vec{m}}}' \frac{\partial^2}{\partial s_\alpha \partial s_\beta} V(\vec{s}-\vec{m}) u_\alpha(\vec{s}) u_\beta(\vec{s}) \\ &\quad + \frac{1}{3!} {\sum_{\vec{m}}}' \frac{\partial^3 V(\vec{s}-\vec{m})}{\partial s_\alpha \partial s_\beta \partial s_\gamma} u_\alpha(\vec{s}) u_\beta(\vec{s}) u_\gamma(\vec{s}) \\ &\quad + \frac{1}{4!} {\sum_{\vec{m}}}' \frac{\partial^4 V(\vec{s}-\vec{m})}{\partial s_\alpha \partial s_\beta \partial s_\gamma \partial s_\delta} u_\alpha(\vec{s}) u_\beta(\vec{s}) u_\gamma(\vec{s}) u_\delta(\vec{s}) + \cdots \end{aligned} \tag{4.3}$$

where the sum over the components of $\vec{u}(\vec{s})$ is automatically implied. The first order term on the right vanishes identically since all derivatives are evaluated at the equilibrium positions. The mean field potential is then

$$U^{MF} = \sum_{\vec{s}} U_{\vec{s}}(\vec{u}(\vec{s})), \tag{4.4}$$

and the force acting on the atom at site $\vec{l}$ in the negative ρ-direction can be easily shown to be

$$\frac{\partial U^{MF}}{\partial u_\rho(\vec{l})} = \frac{\partial U_{\vec{l}}(\vec{u}(\vec{l}))}{\partial u_\rho(\vec{l})}. \tag{4.5}$$

Using the Taylor expansion (4.3) in (4.5) and retaining terms up to the third order only, we obtain

$$\frac{\partial U^{MF}}{\partial u_\rho(\vec{l})} = S_{\rho\alpha} u_\alpha(\vec{l}) + K_{\rho\alpha\beta} u_\alpha(\vec{l}) u_\beta(\vec{l}) + L_{\rho\alpha\beta\gamma} u_\alpha(\vec{l}) u_\beta(\vec{l}) u_\gamma(\vec{l}). \tag{4.6}$$

We have introduced three symmetric tensors $S_{\rho\alpha}$, $K_{\rho\alpha\beta}$ and $L_{\rho\alpha\beta\gamma}$ to simplify the expression. They are written as

$$\begin{aligned} S_{\rho\alpha} &= \sum_{\vec{m}'}{}' \frac{\partial^2 V(\vec{m}')}{\partial m'_\rho \partial m'_\alpha}, \\ K_{\rho\alpha\beta} &= \frac{1}{2!}\sum_{\vec{m}'}{}' \frac{\partial^3 V(\vec{m}')}{\partial m'_\rho \partial m'_\alpha \partial m'_\beta} \end{aligned}$$

and

$$L_{\rho\alpha\beta\gamma} = \frac{1}{3!}\sum_{\vec{m}'}{}' \frac{\partial^4 V(\vec{m}')}{\partial m'_\rho \partial m'_\alpha \partial m'_\beta \partial m'_\gamma}, \tag{4.7}$$

where we have replaced the summation over $\vec{m}$ by $\vec{m}' = \vec{l} - \vec{m}$. Making use of the rectangular symmetry of the lattice, many of the tensor components vanish identically:

$$\begin{aligned} S_{ij} &= 0, && \text{if } i \neq j; \\ K_{lmn} &= 0, && \text{for all } l, m, n; \\ L_{lmnp} &= 0, && \text{if any three of the indices are identical.} \end{aligned}$$

Expression (4.6) is therefore reduced to

$$\frac{\partial U^{MF}}{\partial u_\rho(\vec{l})} = S_{\rho\rho} u_\rho(\vec{l}) + L_{\rho\rho\rho\rho} u_\rho^3(\vec{l}) + 3\lambda u_\rho(\vec{l}) u_\alpha^2(\vec{l}), \tag{4.8}$$

where $\lambda = L_{1122}$; ρ, $\alpha = 1, 2$ but $\alpha \neq \rho$. This is interpreted as the force due to the long-range order among atoms or due to the substrate in the adsorbed layer in the Frenkel-Kontorova model.

4.3 Nearest- Neighbor Interactions

Using the same approach and notation as before, the interaction potential of the atom at site $\vec{s}$ due to its nearest neighbors is given by

$$\sum_{i=1}^{4} V(\vec{a}_i + \vec{u}(\vec{s} + \vec{a}_i) - \vec{u}(\vec{s})) \tag{4.9}$$

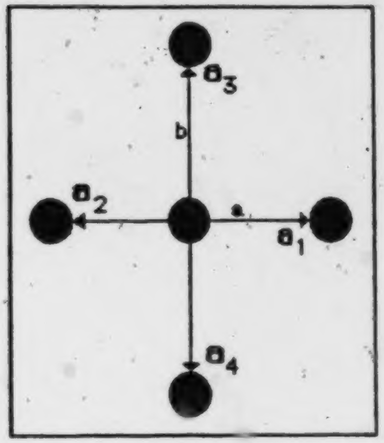

Figure 4.2: An atom with its four nearest-neighbors.

where $\vec{a}_i$ are the primitive lattice vectors. An atom and its four nearest-neighbors are shown in Fig. 4.2. The potential U^{nn} is then

$$U^{nn} = \frac{1}{2}\sum_{\vec{s}}\sum_{i=1}^{4} V(\vec{a}_i + \vec{u}(\vec{s}+\vec{a}_i) - \vec{u}(\vec{s})). \tag{4.10}$$

The factor of 1/2 on the right ensures that each interaction is counted only once. Again, we expand the potential in powers of the cartesian components of the atomic displacements

$$\begin{aligned} U^{nn} &= U^{nn}(0) + \sum_{\vec{m}} \frac{\partial U^{nn}}{\partial u_\alpha(\vec{m})} u_\alpha(\vec{m}) \\ &\quad + \frac{1}{2!}\sum_{\vec{m},\vec{m}'} \frac{\partial^2 U^{nn}}{\partial u_\alpha(\vec{m}')\partial u_\beta(\vec{m})} u_\alpha(\vec{m}') u_\beta(\vec{m}) + \cdots, \end{aligned} \tag{4.11}$$

where the derivatives are evaluated at the atomic equilibrium positions. We now use the harmonic approximation, that is we retain terms only up to second order. This means that any anharmonic terms that appear in the effective potential to be derived later on must come from the mean field approximation we developed in the last section. Since the expansion (4.11) is made around the equilibrium positions, the first order term on the right must vanish identically. Substituting (4.10) into (4.11), and introducing the tensor

$$\begin{aligned}\phi^i_{\alpha\beta} &= \frac{1}{2}\left(\frac{\partial^2 V(\vec{r})}{\partial x_\alpha \partial x_\beta}\right)_{\vec{r}=\vec{a}_i}\\ &= \frac{1}{2}\left\{\frac{x_\alpha x_\beta}{r^2}\left(\frac{\partial^2 V}{\partial r^2}-\frac{1}{r}\frac{\partial V}{\partial r}\right)+\frac{\delta_{\alpha\beta}}{r}\frac{\partial V}{\partial r}\right\}_{r=a_i} \qquad (4.12)\end{aligned}$$

where V($\vec{r}$) is taken to be central and x_i are the cartesian components of $\vec{r}$, we obtain

$$U^{nn} = U^{nn}(0) + \frac{1}{2}\sum_{\vec{s}}\sum_{i=1}^{4}\phi^i_{\alpha\beta}\left[u_\alpha(\vec{s}) - u_\alpha(\vec{s}+\vec{a}_i)\right]\left[u_\beta(\vec{s}) - u_\beta(\vec{s}+\vec{a}_i)\right]. \qquad (4.13)$$

However, the tensor $\phi^i_{\alpha\beta}$ can be simplified further by direct substitution of the primitive lattice vectors $\vec{a}_i$ and expressed in terms of the lattice constants a and b, respectively, as

$$\phi^i = \begin{bmatrix} V''(a) & 0 \\ 0 & \frac{V'(a)}{a} \end{bmatrix}, \text{ for } i = 1,\ 2, \qquad (4.14)$$

and

$$\phi^i = \begin{bmatrix} \frac{V'(b)}{b} & 0 \\ 0 & V''(b) \end{bmatrix}, \text{ for } i = 3,\ 4. \qquad (4.15)$$

These help to reduce the nearest-neighbor interaction potential to

$$\begin{aligned}U^{nn} &= U^{nn}(0) + \sum_{\vec{s}}\phi^1_{\alpha\alpha}\left[u_\alpha(\vec{s}) - u_\alpha(\vec{s}+\vec{a}_1)\right]^2\\ &\quad + \sum_{\vec{s}}\phi^3_{\alpha\alpha}\left[u_\alpha(\vec{s}) - u_\alpha(\vec{s}+\vec{a}_3)\right]^2. \qquad (4.16)\end{aligned}$$

Finally, the force acting on the atom at site $\vec{l}$ in the negative ρ-direction is given by

$$\begin{aligned}\frac{\partial U^{nn}}{\partial u_\rho(\vec{l})} &= 2\phi^1_{\rho\rho}\left[2u_\rho(\vec{l}) - u_\rho(\vec{l}-\vec{a}_1) - u_\rho(\vec{l}+\vec{a}_1)\right]\\ &\quad + 2\phi^3_{\rho\rho}\left[2u_\rho(\vec{l}) - u_\rho(\vec{l}-\vec{a}_3) - u_\rho(\vec{l}+\vec{a}_3)\right]. \qquad (4.17)\end{aligned}$$

4.4 The Equations of Motion and The Continuum Limit

Combining (4.8) and (4.17) gives the equations of motion for the atom at site $\vec{l}$

$$\begin{aligned} m\frac{\partial^2 u_\rho(\vec{l})}{\partial t^2} &= -2\phi^1_{\rho\rho}\left[2u_\rho(\vec{l}) - u_\rho(\vec{l}-\vec{a}_1) - u_\rho(\vec{l}+\vec{a}_1)\right] \\ &\quad -2\phi^3_{\rho\rho}\left[2u_\rho(\vec{l}) - u_\rho(\vec{l}-\vec{a}_3) - u_\rho(\vec{l}+\vec{a}_3)\right] \\ &\quad -S_{\rho\rho}u_\rho(\vec{l}) - L_{\rho\rho\rho\rho}u^3_\rho(\vec{l}) - 3\lambda u_\rho(\vec{l})u^2_\alpha(\vec{l}), \end{aligned} \tag{4.18}$$

where $\rho, \alpha = 1, 2$ and $\alpha \neq \rho$. Up to this point, we have been treating $\vec{l}$ as a discrete variable indexing different lattice sites. In addition, since we are assuming an infinitely large lattice, (4.18) represents a system of infinitely many coupled equations. In order to reduce the number of equations to a managable size, we need to go over to the continuum limit. In doing so, we regard $\vec{l}$ as a continuous variable and expand $u_\rho(\vec{l}\pm\vec{a}_1)$ and $u_\rho(\vec{l}\pm\vec{a}_3)$ in a Taylor series as

$$u_\rho(\vec{l}\pm\vec{a}_1) = u_\rho(\vec{l}) \pm \frac{\partial u_\rho(\vec{l})}{\partial l_1}a + \frac{1}{2!}\frac{\partial^2 u_\rho(\vec{l})}{\partial l_1^2}a^2 \pm \cdots$$

and

$$u_\rho(\vec{l}\pm\vec{a}_3) = u_\rho(\vec{l}) \pm \frac{\partial u_\rho(\vec{l})}{\partial l_2}b + \frac{1}{2!}\frac{\partial^2 u_\rho(\vec{l})}{\partial l_2^2}b^2 \pm \cdots. \tag{4.19}$$

Substituting (4.19) into (4.18), replacing $\vec{l}$ by $\vec{r} = (x\vec{i} + y\vec{j})$ and ignoring high order terms in the expansion, the equations of motion become

$$\begin{aligned} m\frac{\partial^2 u_\rho(\vec{r})}{\partial t^2} &= \sigma_{\rho\rho}\frac{\partial^2 u_\rho(\vec{r})}{\partial x^2} + \zeta_{\rho\rho}\frac{\partial^2 u_\rho(\vec{r})}{\partial y^2} \\ &\quad -S_{\rho\rho}u_\rho(\vec{r}) - L_{\rho\rho\rho\rho}u^3_\rho(\vec{r}) - 3\lambda u_\rho(\vec{r})u^2_\alpha(\vec{r}), \end{aligned} \tag{4.20}$$

where σ and ζ are defined as

$$\sigma = \begin{bmatrix} 2a^2V''(a) & 0 \\ 0 & 2aV'(a) \end{bmatrix}$$

and

$$\zeta = \begin{bmatrix} 2bV'(b) & 0 \\ 0 & 2b^2V''(b) \end{bmatrix}. \tag{4.21}$$

For a typical two-body potential such as the Lennard-Jones potential and at a typical equilibrium atomic spacing [41], σ_{11} and ζ_{22} are always positive whereas σ_{22} and ζ_{11} are of arbitrary signs. Next, we assume travelling wave-like solutions in the form:

$$u_1 = u_1(\vec{k}\cdot\vec{r} - \omega t) = u_1(z)$$

and

$$u_2 = u_2(\vec{k}\cdot\vec{r} - \omega t) = u_2(z), \tag{4.22}$$

where $\vec{k} = (k_x\vec{i} + k_y\vec{j})$ plays the role of the wave vector and ω the angular frequency. Upon substitution, the equations of motion take the following form:

$$\frac{d^2u_1}{dz^2} = \frac{1}{\Omega}(S_{11}u_1 + L_{1111}u_1^3 + 3\lambda u_1u_2^2)$$

and

$$\frac{d^2u_2}{dz^2} = \frac{1}{\Phi}(S_{22}u_2 + L_{2222}u_2^3 + 3\lambda u_2u_1^2) \tag{4.23}$$

where Ω is defined as

$$\Omega = \sigma_{11}k_x^2 + \zeta_{11}k_y^2 - m\omega^2$$

and Φ as

$$\Phi = \sigma_{22}k_x^2 + \zeta_{22}k_y^2 - m\omega^2. \tag{4.24}$$

These equations can be converted into a more convenient form by introducing the dimensionless variables X, Y, T:

$$\begin{aligned} z &= \tau T, \\ u_1 &= \mu X, \\ u_2 &= \nu Y. \end{aligned} \tag{4.25}$$

Such scaling is beneficial both for physical insight and for numerical convenience. Provided

$$\nu^2\Phi = \mu^2\Omega$$

and

$$\frac{\tau^2\mu^2 L_{1111}}{\Omega} = \frac{\tau^2\nu^2 L_{2222}}{\Phi} = -1, \tag{4.26}$$

(4.23) can be written as

$$\begin{aligned} \frac{d^2X}{dT^2} &= K_X X - X^3 + DXY^2 \\ \frac{d^2Y}{dT^2} &= K_Y Y - Y^3 + DYX^2 \end{aligned} \tag{4.27}$$

where

$$K_X = \frac{\tau^2 S_{11}}{\Omega}, K_Y = \frac{\tau^2 S_{22}}{\Phi} \tag{4.28}$$

and

$$D = \frac{3\tau^2\mu^2\lambda}{\Phi} = \frac{3\tau^2\nu^2\lambda}{\Omega}. \tag{4.29}$$

Therefore, we have reduced a system of infinitely many coupled equations (4.18) to two equations of motion for each of the displacement components X and Y. However, in adopting the continuum limit, we have assumed that the lattice constants are infinitesimally small. Hence, we have focused ourselves on only those solutions whose spatial extent is very large in comparison with the lattice constants a and b (i.e. we have adopted a long wave length limit).

Equations (4.27) describe a phonon-field in an infinitely large two-dimensional lattice. Their solutions give either the time evolution or the spatial variation of the field. Clearly, they can be looked upon as a system of two coupled anharmonic oscillators. As pointed out earlier in section 4.3, the anharmonicity of the system, the cubic and the coupling term in (4.27), must come from the mean field approximation. Unfortunately, demanding the conditions (4.26) to be satisfied, we have put our model in a much restrictive form. The dynamics corresponding to equations (4.27) represents only a subset of the solutions to the more general equations (4.23).

4.5 The Hamiltonian

We look for a Lagrangian density that generates the equations of motion (4.20). Such a density function could have the form

$$\begin{aligned}\mathcal{L} &= \sum_{i=1}^{2}\left\{\frac{m}{2}\left(\frac{\partial u_i}{\partial t}\right)^2 - \frac{\sigma_{ii}}{2}\left(\frac{\partial u_i}{\partial x}\right)^2 - \frac{\zeta_{ii}}{2}\left(\frac{\partial u_i}{\partial y}\right)^2 - \frac{S_{ii}}{2}u_i^2 - \frac{L_{iiii}}{4}u_i^4\right\} \\ &\quad -\frac{3}{2}\lambda u_1^2 u_2^2. \qquad (4.30)\end{aligned}$$

For a continuous system, the corresponding Euler-Lagrange equations for the field variable η_ρ are

$$\sum_{\nu=0}^{3}\frac{d}{dx_\nu}\left(\frac{\partial \mathcal{L}}{\partial \eta_{\rho,\nu}}\right) - \frac{\partial \mathcal{L}}{\partial \eta_\rho} = 0. \qquad (4.31)$$

It can be easily shown that, by direct substitution into (4.31), the Lagrangian density (4.30) does correspond to equations (4.20). Taking this Lagrangian density, the conjugate momentum densities are given by

$$p_1 = \frac{\partial \mathcal{L}}{\partial \dot{u}_1} = m\dot{u}_1$$

and

$$p_2 = \frac{\partial \mathcal{L}}{\partial \dot{u}_2} = m\dot{u}_2. \qquad (4.32)$$

These naturally lead to the Hamiltonian density

$$\begin{aligned}\mathcal{H}' &= p_1\dot{u}_1 + p_2\dot{u}_2 - \mathcal{L} \\ &= \sum_{i=1}^{2}\left\{\frac{m}{2}\left(\frac{\partial u_i}{\partial t}\right)^2 + \frac{\sigma_{ii}}{2}\left(\frac{\partial u_i}{\partial x}\right)^2 + \frac{\zeta_{ii}}{2}\left(\frac{\partial u_i}{\partial y}\right)^2 + \frac{S_{ii}}{2}u_i^2 + \frac{L_{iiii}}{4}u_i^4\right\} \\ &\quad +\frac{3}{2}\lambda u_1^2 u_2^2. \qquad (4.33)\end{aligned}$$

In order to obtain an effective Hamiltonian density that corresponds to the resultant equations of motion (4.27), we again assume the travelling wave solutions (4.22) and scale the variables according to (4.25). In addition, the Hamiltonian density is also scaled as

$$\mathcal{H}' = \varepsilon\mathcal{H}. \tag{4.34}$$

The purpose of scaling here is to avoid imposing extensive physical constraints on the system. Rather, the contraints are also shared by the scaling parameters τ, μ, ν and ε. Therefore, the final Hamiltonian density takes the most convenient form and, at the same time, the system remains applicable to a wide range of cases. Following these procedures, assuming (4.26) and

$$\frac{\Omega\mu^2}{\tau^2\varepsilon} = -1, \tag{4.35}$$

the effective Hamiltonian density can be written as

$$\mathcal{H} = \frac{P_X^2}{2M_X} + \frac{P_Y^2}{2M_Y} - \frac{1}{2}\left(K_X X^2 + K_Y Y^2\right) + \frac{1}{4}\left(X^4 + Y^4\right) - \frac{D}{2}\left(X^2Y^2\right), \tag{4.36}$$

where

$$\begin{aligned} P_X &= M_X \frac{dX}{dT}, \\ P_Y &= M_Y \frac{dY}{dT}, \\ M_X &= -\left(\frac{2m\omega^2}{\Omega} + 1\right) \end{aligned}$$

and

$$M_Y = -\left(\frac{2m\omega^2}{\Phi} + 1\right). \tag{4.37}$$

In the case of weak coupling, the two oscillators are essentially independent of each other and their individual energies are best represented by

$$E_i = \frac{P_i^2}{2M_i} - \frac{K_i}{2}Q_i^2 + \frac{1}{4}Q_i^4 \tag{4.38}$$

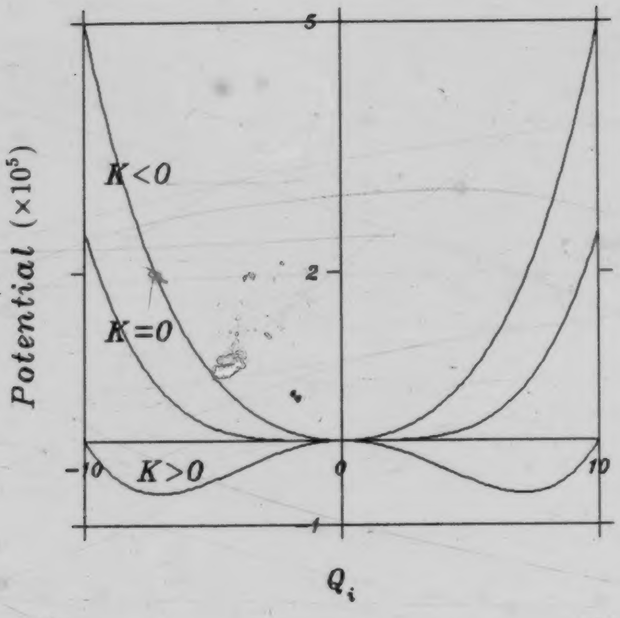

Figure 4.3: The potential energy of the decoupled oscillators for various values of the effective wave vector K.

where $i = X, Y$. A typical plot of the corresponding potential is depicted in figure 4.3. The figure shows the potential changes from a single-minimum to a double-minimum type as the effective wave-vector K_i changes from negative to positive. This feature resembles the Landau-type free energy expansion in which the energy profile is temperature dependent. Furthermore, the critical value $K_i = 0$ marks the onset of chaos. Since chaos usually appears in the neighborhood of a potential peak (separatrix), it seems reasonable to assume that chaos is present in our system only if $K_i > 0$.

4.6 Numerical Analysis

We now look at the special case where we put $K_X = K_Y = 1$, $D = -\frac{1}{2}$ and

$$M_X = M_Y = 1, \tag{4.39}$$

and examine the dynamical behavior of the system. The last condition (4.39) is the most restrictive condition in the present model. From (4.37) and (4.24), it simply means that the outcome of the model is relevant only if the following two conditions hold simultaneously:

$$\sigma_{11} k_x^2 + \zeta_{11} k_y^2 = 0 \tag{4.40}$$

and

$$\sigma_{22} k_x^2 + \zeta_{22} k_y^2 = 0 \tag{4.41}$$

Whether these conditions hold crucially depends on the two-body potential. They hold only if $V'(b)$ and $V''(a)$ are of opposite sign, and similarly for $V'(a)$ and $V''(b)$. In addition, non-trival solutions exist only if $\sigma_{11}/\zeta_{11} = \sigma_{22}/\zeta_{22}$. Even though the two-body potential is such that (4.40) and (4.41) can be satisfied simultaneously, the dynamics of the model represents only those phonon modes in a very narrow subset of $\vec{k}$ space determined by the very same conditions and, from the dispersion relation, it corresponds to those modes in a small subset of the available vibrational frequencies. To be more specific, these phonon modes lie on two straight line intervals in the accessible $\vec{k}$ space. The straight lines pass through the origin. Their slopes are of equal magnitude but of opposite signs. These are the limitations that one has to bear in mind when attempting to apply the model to any physical system.

Furthermore, from (4.24), conditions (4.40) and (4.41) imply $\Omega = \Phi = -m\omega^2$. From (4.28), setting $K_X = K_Y = 1$ means

$$S_{11} = S_{22} < 0. \tag{4.42}$$

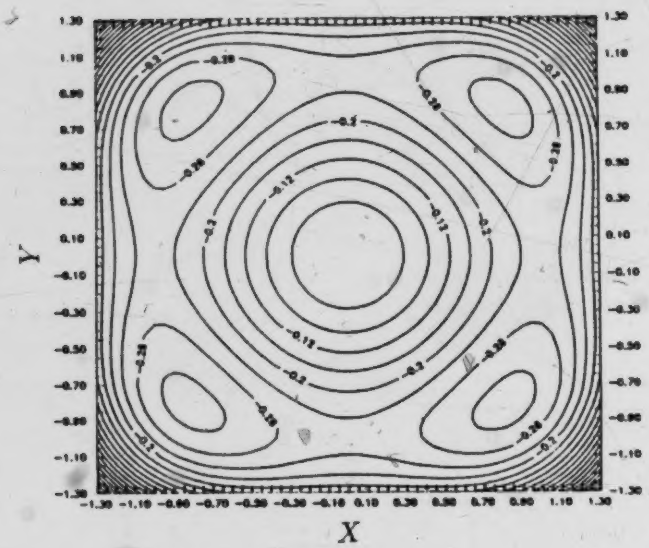

Figure 4.4: Contour plot of the potential in (4.43).

But, by definition(4.7), $S_{\rho\rho}$ are the second derivatives of the interaction potential $U_s(\vec{u}(\vec{s}))$ evaluated at the equilibrium positions in the mean field approximation. Condition (4.42) then implies the lattice points represent unstable equilibria. Hence, this particular choice of K_X, K_Y, M_X and M_Y leads us to a model which possesses intrinsic instability.

From the Hamiltonian density (4.36), the potential energy of the phonon field is given by

$$V(X,Y) = -\frac{1}{2}(X^2+Y^2) + \frac{1}{4}(X^4+Y^4) + \frac{1}{4}X^2Y^2 \tag{4.43}$$

and its contour plot is shown in Figure 4.4. The potential has a barrier at the origin and four minima, each at an energy approximately $-1/3$, located at $(\pm\sqrt{2/3}, \pm\sqrt{2/3})$. Intuitively, at low energies, the particle is trapped and lies very close to the bottom of the potential well. At these energy levels, coupling is weak and motion is very restrictive. The system should behave regularly. Chaos appears only when the energies are high enough so that the particle can escape from one well to another.

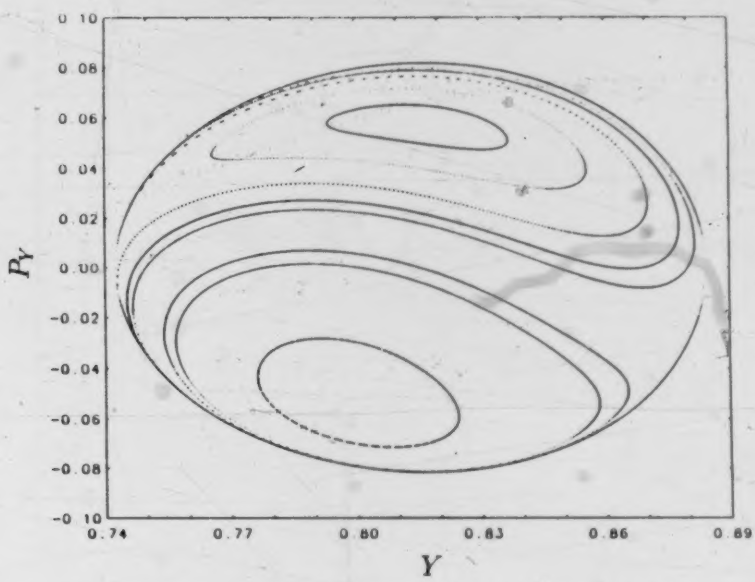

Figure 4.5: Poincaré section at $E = -0.33$.

This is expected to happen in the neighborhood of the potential peak ($E = 0$ in our case).

The equations of motion (4.27) were solved using the 4th order Runge- Kutta method for the energies −0.33, −0.31, −0.275, −0.2499, −0.24, −0.05, 1, 10 and 1000. To ensure accuracy, all calculations were carried out in double precision and the integration step was chosen to be 0.0005. The dynamical behavior of the system is represented by Poincaré sections P_Y *vs* Y as in Fig. 4.5-4.14, where we take the initial momenta to be positive, $X = \sqrt{2/3}$ and $P_X > 0$.

Expectedly, the system exhibits regular behavior at extremely low energies as shown in Fig. 4.5. The particle is trapped in one of the potential wells. All orbits generated are highly regular. Bifurcation takes place at slightly elevated energies. As indicated in Fig. 4.6, the single orbit marked "b" splits into two close loops, separated by the separatrix labeled "s". Evidently, this separatrix acts as a divider for infinitely many orbits within this finite region of phase space. This is indeed

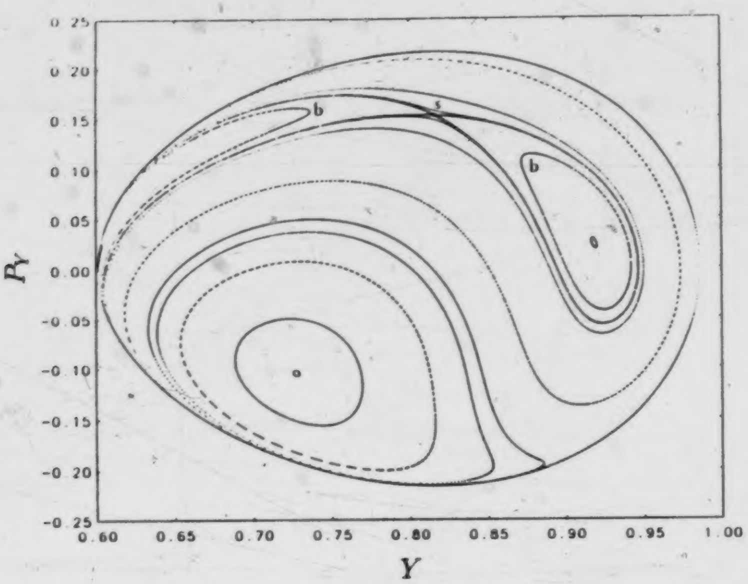

Figure 4.6: Poincaré section at $E = -0.31$.

a well-known property of a strange attractor. Furthermore, within the separatrix itself as shown in Fig. 4.7, chaos is clearly seen.

At energy -0.275, as shown in Fig. 4.8, many regular orbits break up into randomly scattered trajectories. Chaotic structure is beginning to dominate the picture. A chain of islands which completely encloses the regular region acts as a boundary separating the order from the chaos. The particle is no longer trapped at energy -0.2499. Figure 4.9 shows that it hops from one potential well to another. Its trajectories are spread all over the two enclosed regions. The system is becomming increasingly chaotic; regular structure is beginning to shrink. The contour of the Poincaré map is now extended to two symmetrical but well separated ovals. This extension manifests a possible phase transition.

At energy levels slightly below the potential peak, the system is completely chaotic as shown in Fig. 4.11. The two ovals have merged to give a much bigger contour, as the four symmetrical potential wells become accessible to the particle.

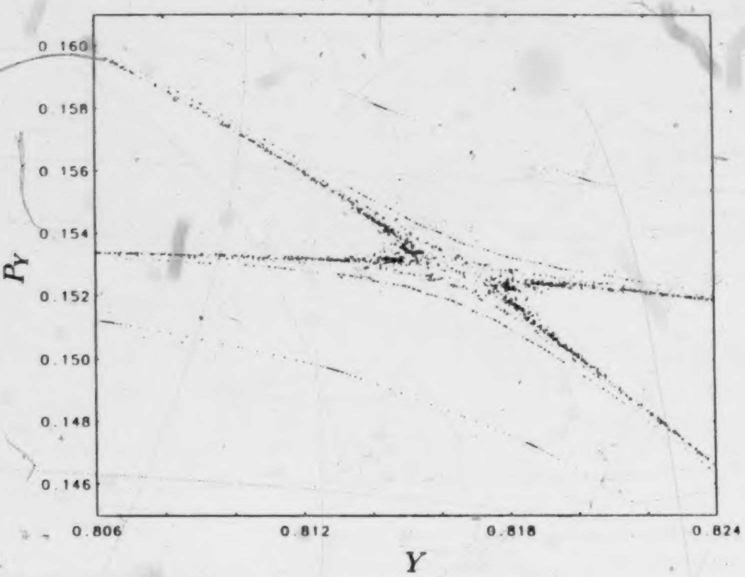

Figure 4.7: Separatrix of the previous figure.

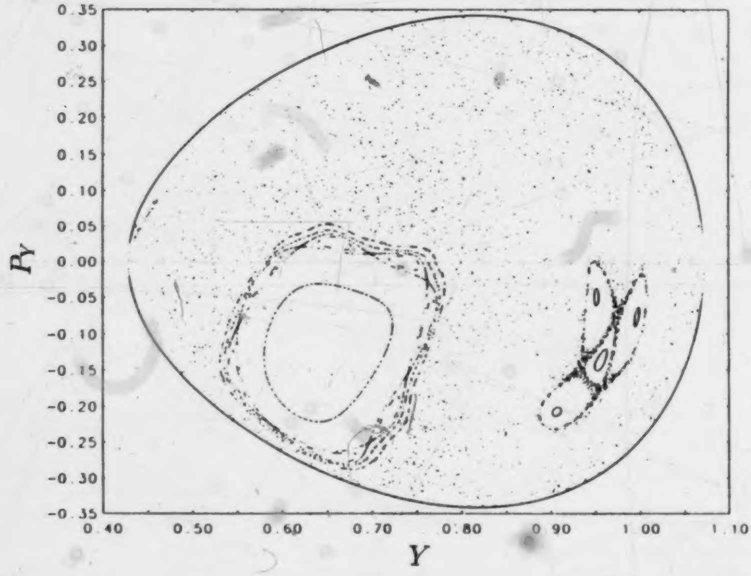

Figure 4.8: Coexistence of chaotic and regular structures at $E = -0.275$.

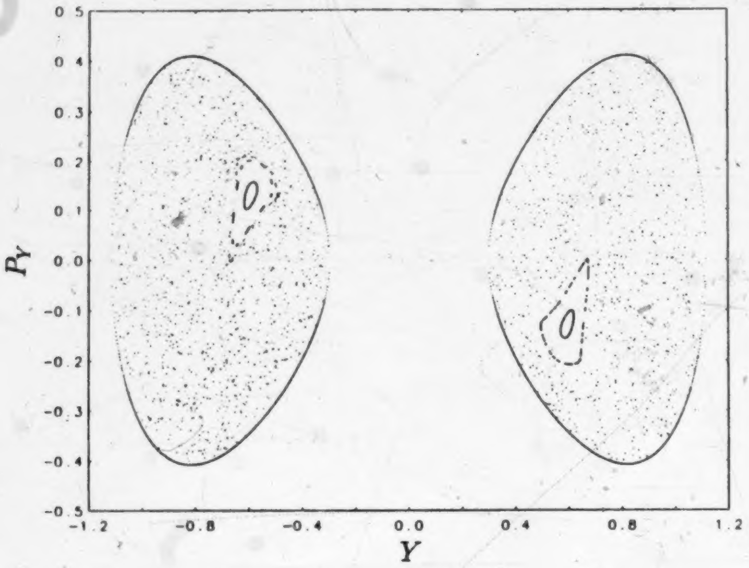

Figure 4.9: Diminishing regular region at $E = -0.2499$.

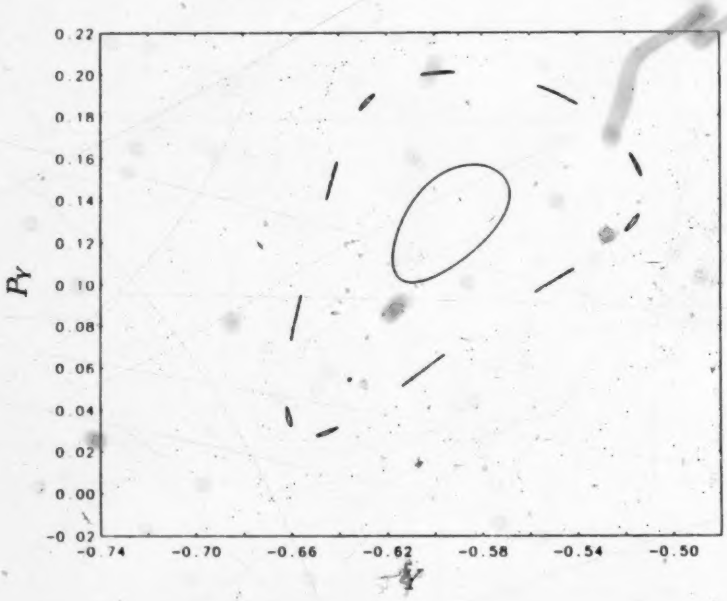

Figure 4.10: Islands of high-order resonance from the previous figure.

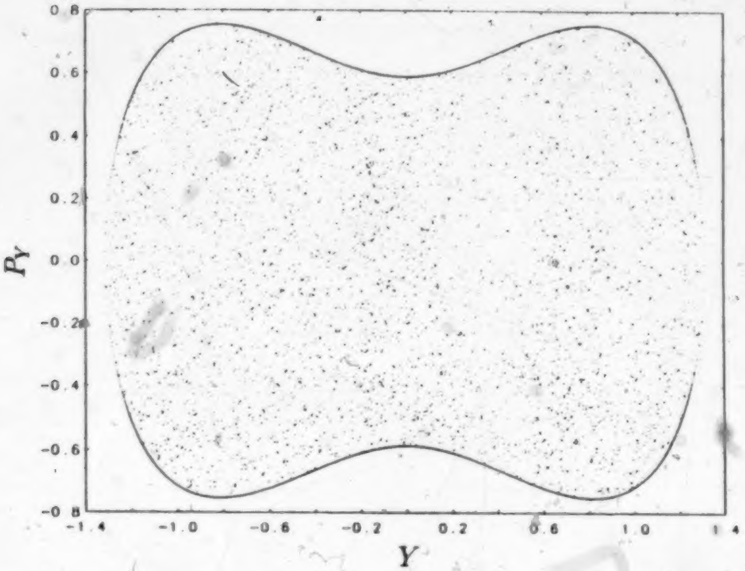

Figure 4.11: Complete chaos at $E = -0.05$.

This, once again, indicates another possible phase transition. Figure 4.12 shows that regular trajectories and chains of islands are starting to reappear as the energy level is raised beyond the peak. While the energy continues to climb upward, the regular region expands at the expense of the chaotic one. This is clearly demonstrated in Figures 4.13 and 4.14. The order-disorder transition seems to repeat itself but in the reverse direction. It is therefore possible that, at extremely high energies, the system's behavior could become completely regular again. In fact, this transitional cycle has been observed earlier by Ali and Somorjai [42].

Whether a system behaves chaotically or not depends largely on the shape of the potential. Our Poincaré sections suggest that complete or partial chaos exists only in the neighborhood of the irregularity in the potential which, in our case, is the region near the potential barrier. For a smooth and regular potential, chaos is therefore unlikely. In our model, the depth of the potential wells depends on the effective wave vector $\vec{K}$ which in turn depends on the long-range interaction

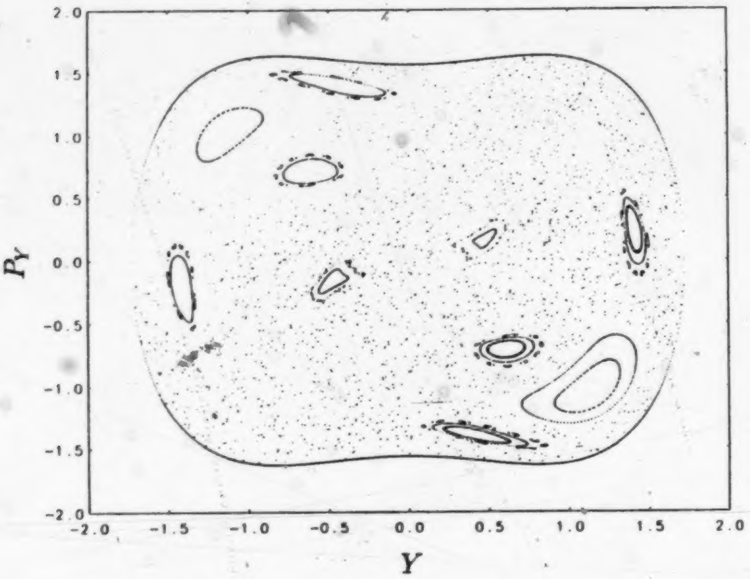

Figure 4.12: Emergence of regular structure at $E = 1$.

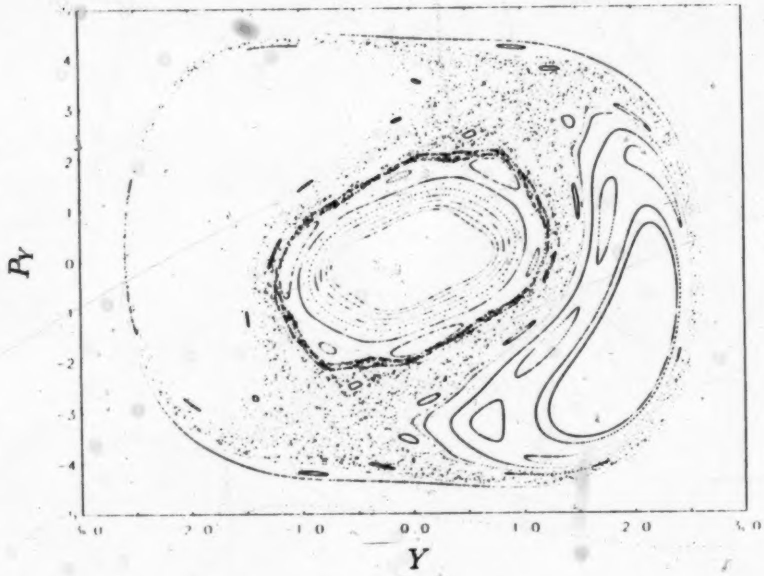

Figure 4.13: Expansion of regular region at $E = 10$.

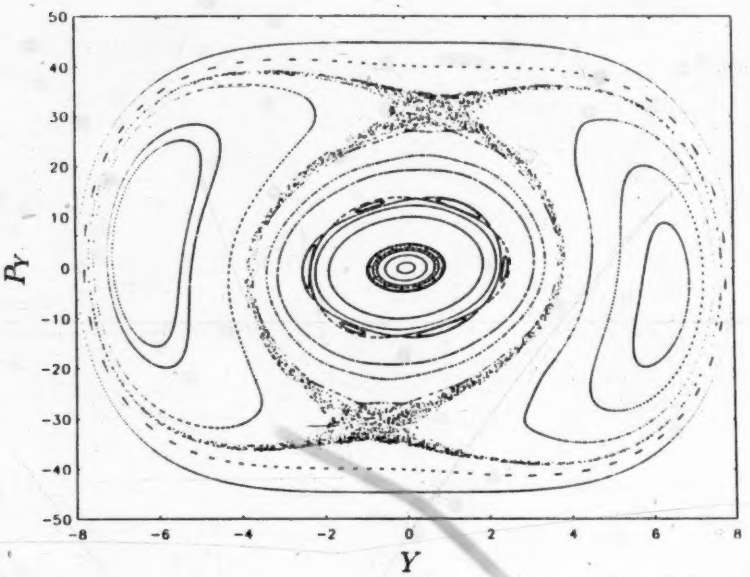

Figure 4.14: Dominance of regular structure at $E = 1000$.

potential and the dispersion of the medium. Therefore, it is the competition between the long-range order and the dispersion that determines if the system is capable of exhibiting chaotic behavior. Given such capability, chaos manifests itself only when the system is oscillating in the irregular region of the potential.

Finally, because of the choice of parameters, we are restricted only to a narrow range of the system's behavior. Our model is hence quite limited. A future direction to take will be to investigate the case where $K_X \neq K_Y$ and to determine how the system responds as K_X or K_Y changes sign. This choice of $\vec{K}$ certainly introduces an asymmetric potential, and the depths of the potential wells change quite independently as $\vec{K}$ varies. This model can then be applied to describe the dynamics of a stable-metastable phase transition, i.e. a first order one.

4.7 Conclusions

In summary, we have first shown that some important one-component (scalar) systems are deterministic and exactly solvable. Particularly, for the case of the three-dimensional Landau-Ginzburg model applied to a ferromagnet where the z-component of the magnetization is taken as the order parameter, the exact analytical solutions include solitary waves and correspond to physical realizations such as domain walls, nucleation processes and magnetic double layers. We have further shown that the presence of a weak magnetic field breaks the symmetry of the equation of motion and also that of the solutions. The mean values of the oscillatory solutions in this case shift as the magnitude of the field varies. There are also indications of competition between the local inhomogeneous and the mean field properties of the solutions. The result of the competition is such that in some cases it could be energetically more favourable to have the magnetization antiparallel to the field.

Secondly, we have demonstrated that systems that are described by two coupled spatial parameters are capable of exhibiting chaotic behavior. Although exact analytic methods for nonlinear coupled equations of motion are not available at this time, we have shown, through the x^2y^2 potential problem, that perturbative techniques can be used to model the approximate behavior of the system and to extract useful information. Finally, we have shown how anharmonic perturbation to a two-dimensional atomic lattice leads to a system with two coupled spatial parameters. We have examined very closely the chaotic transitional behavior of the system and found that whether chaos manifests itself depends on both the energy level of the system and the smoothness of its effective potential.

Therefore, in this thesis, we have provided exact, perturbative and numerical methods for quartic nonlinear Hamiltonian systems with one or two parameters.

The specific examples chosen in this thesis serve as prototypes, they can be easily generalized for solving problems within the same class. As is well known from the literature on phase transitions and critical phenomena, potential systems and phenomena which qualify for applications are extremely numerous and cover many different areas of physics.

BIBLIOGRAPHY

[1] L. D. Landau and E. M. Lifshitz, *Statistical Physics*(Pergamon, London, 1959).

[2] J. F. Currie, J. A. Krumhansl, A. R. Bishop and S. E. Trullinger, *Phys. Rev.*, **B22**(1980) 477.

[3] R. F. Dashen, B. Hasslacher and A. Neven, *Phys. Rev.*, **D10**(1974) 4130.

[4] T. Schreider and E. Stoll, *Phys. Rev.*, **B13**(1976) 1216.

[5] J. A. Krumhansl and J. R. Schrieffer, *Phys. Rev.*, **B11**(1975) 3535.

[6] D. J. Scalapino, M. Sears and R. A. Farrell, *Phys. Rev.*, **B6**(1972) 3409.

[7] A. R. Bishop and J. A. Krumhansl, *Phys. Rev.*, **B12**(1975) 2824.

[8] J. A. Tuszyński, *Phys. Lett.*, **110A**(1985) 148.

[9] P. Dahlqvist and G. Russberg, *Phys. Rev. Lett.*, **65**(1990) 2837.

[10] J. A. Tuszyński, M. Otwinowski, R. Paul and A. P. Smith, *Phys. Rev.*, **36B**(1987) 2190.

[11] P. Winternitz, A. M. Grundland and J. A. Tuszyński, *J. Phys. C: Solid State Physics*, **21**(1988) 4931.

[12] P. Winternitz, A. M. Grundland and J. A. Tuszyński, *To Be Published.*

[13] P. F. Byrd and M. D. Friedman, *Handbook of Elliptic Integrals for Engineers and Scientists* (Springer Verlag, Berlin, 1971).

[14] S. G. Matanyan, G. K. Savvidy and N. G. TerArutyunyan-Savvidy, *Sov. Phys. JETP,* **53**(1981) 421.

[15] B. V. Chirikov and D. L. Shepelyansky, *JETP Lett.*, **34**(1981) 163.

[16] E. S. Nikolaevskii and L. N. Shur, *JETP Lett.*, **36**(1982) 218.

[17] G. K. Savvidy, *Phys. Lett.*, **130B**(1983) 303.

[18] G. K. Savvidy, *Nucl. Phys.*, **B246**(1984) 302.

[19] A. Carnegie and I. C. Percival, *J. Phys.*, **A17**(1984) 801.

[20] S-J. Chang, *Phys. Rev.*, **D29**(1984) 259.

[21] W-H. Steeb, C. M. Villet and A. Kunick, *J. Phys.*, **A18**(1985) 3269.

[22] G. Sohos, T. Bountis and H. Polymilis, *Nuovo Cimento*, **B104**(1989) 339.

[23] C. C. Martens, R. L. Waterland and W. P. Reinhardt, *J. Chem. Phys.*, **90**(1989) 2328.

[24] E. T. Whittaker and G. N. Watson, *A Course of Modern Analysis*(Cambridge University Press, Cambridge, 1963)p.575.

[25] G. M. Murphy, *Ordinary Differential Equations and their Solutions*(Van Nostrand, Princeton, New Jersey, 1960)p.378.

[26] B. Dey and S. Parthesarathy, *Phy. Rev.* **B42**(1990) 6433.

[27] S. N. Pnevmatikos, *"Solitons in Nonlinear Atomic Chains,"* Singularities and Dynamical Systems(Elsevier Science Publishers B.V., North-Holland, 1985).

[28] E. W. Montroll, *The Journal of Chemical Physics*, **15**(1947) 575.

[29] O. M. Braun, *Surface Science*, **230**(1990) 262.

[30] O. M. Braun and Y. S. Kivshar, *Phy. Rev.* **B43**(1991) 1060.

[31] I. Markov and V. D. Karaivanov, *Thin Solid Films,* **65**(1980) 361.

[32] S. Stoyanov and H. Muller-Krumbhaar, *Surface Science,* **159**(1985) 49.

[33] I. Markov and A. Milchev, *Thin Solid Films,* **126**(1985) 83.

[34] A. Milchev, *Phys. Rev.* **B33**(1986)2062.

[35] G. Teodorou and T. M. Rice, *Phy. Rev.* **B18**(1978) 2840.

[36] V. L. Pokrovsky and A. L. Talapov, *Sov. Phys.-JETP,* **48**(1978) 579.

[37] A. G. Naumovets, *Sov. Sci. Rev.* **A5**(1984) 443.

[38] A. G. Naumovets and Yu. S. Vedula, *Surf. Sci. Rep.* **4**(1984) 365.

[39] I. F. Lyuksyutov, A. G. Naumovets and V. L. Pokrovsky, *Two-Dimensional Crystals*(Naukova Dumka, Kiev, 1988).

[40] M. V. Berry, *AIP Conference Proceedings,* **46**(1978) 16.

[41] C. Kittel, *Introduction to Solid State Physics*(John Wiley & Sons, New York, 1986)p.63.

[42] M. K. Ali and R. L. Somorjai, *Physica,* **1D**(1980) 383.